EXPERIMENTAL AND NUMERICAL INVESTIGATIONS OF TRIBOMECHANICAL BEHAVIOUR OF SiMoCr DUCTILE CAST IRON

NANAK RAM

DEPARTMENT OF MECHANICAL ENGINEERING

DELHI TECHNOLOGICAL UNIVERSITY DELHI

September 2023

EXPERIMENTAL AND NUMERICAL INVESTIGATIONS OF TRIBOMECHANICAL BEHAVIOUR OF SiMoCr DUCTILE CAST IRON

by

NANAK RAM

DEPARTMENT OF MECHANICAL ENGINEERING

Submitted

in fulfillment of the requirements of the degree of

Doctor of Philosophy

to the

DELHI TECHNOLOGICAL UNIVERSITY DELHI

September 2023

Dedicated

To

my beloved Parents

and

my wife Manju Rani,

my lovely children

Madhav *and* Divyansh Saini

for their unconditional love and support

CERTIFICATE

This is to certify that the thesis entitled " **Experimental And Numerical Investigations of Tribomechanical Behaviour of SiMoCr Ductile Cast Iron**" being submitted by **Mr. Nanak Ram** to **Delhi Technological University Delhi** for the award of the degree of **Doctor of Philosophy** in the Department of Mechanical Engineering is a bonafide research work carried out by him under my supervision and guidance. To the best of my knowledge the thesis has reached the requisite standard. The research reports and the results presented in this thesis have not been submitted in parts or in full to any other University or Institute for the award of any degree or diploma.

(**Dr. Vijay Gautam**)

Professor

Department of Mechanical Engineering

Delhi Technological University Delhi

New Delhi-110042

ACKNOWLEDGEMENTS

I would like to convey my deep sense of gratitude and sincere thanks to **Prof. Vijay Gautam**, for giving me an opportunity to pursue this research work under his guidance. I have learnt a lot from his remarkable acumen, enthusiasm, management, motivation and determination while carrying out this work without which timely completion of the thesis would have been nearly impossible. Words are really short to suffice his favour and cooperation. I am grateful to him in all respects.

I express my deep sense of gratitude to **Prof. S. K Rathore** (RTU Kota, Rajasthan), Prof. **Mohammad Suhaib** (JMIU, Delhi), Prof. Anil Kumar (DTU, Delhi) and **Prof. A. K Agarwal** (DTU, Delhi) for being part of my thesis committee. Their questions and valuable suggestions during my presentations and examinations have been very useful in providing direction to my research work. I am also grateful to **Prof. S. K. Garg**, Head of Department of Mechanical Engineering and other faculty members for their kind support in carrying out my research work.

My special thanks to my colleague and friend **Dr. Ajay Chhillar and Sh. Sanjeev Kumar** for their constant encouragement and unconditional support. Thanks to my fellow research scholars **Sh. Ravi Kumar, Sh. Subhajit, Sh. Bijender Kumar and Sh. Rakesh kumar** for their fruitful and productive association.

I would like to express my immense gratitude to **Dr. Sanjay Kumar**, DTU Delhi, for his valuable suggestion and help in carrying out the fatigue tests in IIT Delhi. I also would like to express my immense gratitude to **Dr. N. Yuvraj,** DTU Delhi, for his valuable support in the preparation of the said alloy in foundry shop DTU Delhi. I would like to thank **Sh. Tek Chand** and **Sh. Om Prakash** for their kind support in the experimental work carried out at DTU Delhi.

I express my unfailing gratitude towards Department of Training and Technical Education, Delhi for allowing me to conduct research work as a part-time scholar.

I take this opportunity to thank my all friends who helped me directly or indirectly during this research work.

Finally, I am highly indebted to my family members for their unconditional love, support, sacrifice and blessings.

Last but not the least, I humbly thank my **SATGURU JI** for being so kind to me and pray that everyone is bestowed with opportunities and capabilities to fulfil their dreams.

(**Nanak Ram**)

DTU Delhi

ABSTRACT

The versatility of ductile cast iron in the mechanical properties obtained through compositions and microstructure control in as-cast components offers reduced energy and material requirements by eliminating the cost of heat treatments. In the present study, three different melts Melt-1, Melt-2 and Melt-3 of SiMoCr ductile cast iron are prepared to study the effect of silicon, molybdenum and chromium on microstructure with reference to the variation in the matrix of ratio of pearlite and ferrite, nodularity, nodule size and nodule count and their resulting effects on tensile, hardness, wear and fracture properties of the material. For a given chemical composition and nodule size, an increase in the nodule count decreases the pearlite-ferrite ratio which further results in a reduction in tensile strength but an increase in percentage elongation. Elongated, sharp, wavy, or spiky edges of the nodules result in stress concentration and promote crack growth in the matrix. The spherical nodule plays a significant role in arresting the crack and reorients the crack path around the nodule. Nodule count also affects graphite shape, size and distribution. An increase in the nodule count decreases the nodule size in the matrix of ferrite and pearlite results in a finer grain structure which further increases the tensile strength.

The uniaxial tensile tests are conducted from the specimens taken out from the as-cast sample bars at different strain rates and temperatures to analyze the combined effect of the amount of deformation, strain rate and temperature on the plastic behaviour of the material under different working conditions both in experiments and simulations. The various parameters of the Johnson-Cook material model are determined by following the standard procedure. Microstructural examination depicts that the percentage of various alloying elements affects the variation in the matrix of the ratio of pearlite and ferrite,

nodularity, nodule size and nodule count and thereby affecting the tensile properties and *J-C* parameters of the material. A common three-point bend test is performed as per the standard test procedure to determine the fracture toughness of the developed materials. The value of static fracture toughness obtained from the experimental data for the fatigue pre-crack specimen prepared from the test bars of Melt-2 is higher than the rest of the samples prepared from the test bars of the other two melts which may be attributed to the homogeneous distribution of the nodules in the matrix of ferrite and pearlite. According to the results obtained from FE simulations with fatigue pre-crack, the results for fracture toughness are found to be in good agreement with the results obtained from experimental data. A series of pin-on-disc wear tests is conducted to study the dry sliding behaviour of Melt-3, by using the Taguchi L_{16} array for the optimum combination of load, sliding velocity and temperature, on a rotary tribometer setup, at controlled temperatures. The analysis of variance, first-order regression analysis and confirmation tests are done to validate the results obtained for the material's wear properties. Scanning electron microscope (SEM) and energy dispersive x-ray (EdX) analysis are also done for microstructural transformations. It is found that the sliding velocity has a higher influence on the specific wear rate. In contrast, the applied load is the key influencing parameter for a higher value of the coefficient of friction. In last, for testing the developed material in real-world situations, the wear and temperature response of brake discs made from Melt-3 of SiMoCr ductile cast iron against the brake pad under intermittent braking is also studied. A separate disc brake test rig setup is developed, for such intermittent baking tests, using a 15 hp induction motor, chain drive set for power transmission, brake shaft, brake caliper and SiMoCr brake disc.

From this study, it is observed that the developed material showed good tensile and hardness properties. The highest values of the ultimate tensile strength (606MPa) and

percentage elongation (13.98%) are observed in Melt-2. The average hardness value observed in the specimens of Melt-3 is the highest i.e., 298 ± 10.67 HV0.5 among the three melts. Melt-2 specimens showed the highest static fracture toughness as 54.49 MPa√m followed by fracture toughness observed in the samples of Melt-1 and Melt-3. The temperature evolved during intermittent braking at locking brake load is recorded experimentally as 198.7 °C, which agrees with the results obtained from numerical analysis and simulation. Overall, the material developed, SiMoCr DCI, in the present research will be a good contender for engineering applications where good tensile strength coupled with toughness, crack resistance and good wear properties are the key factors.

Keywords: *Ductile cast iron, nodularity, microstructure, Vickers microhardness, J-C parameters, single edge-notched beam, crack mouth opening displacement, fracture toughness, pin-on-disc, specific wear rate (k), Coefficient of friction (μ), Taguchi* L_{16} *array, FE simulations.*

TABLE OF CONTENTS

LIST OF TABLES

LIST OF FIGURES

ABBREVIATIONS

ADI	Austempered Ductile Iron
AISI	American Iron and Steel Institute
Al-Cu	Aluminum-Copper
ANOVA	Analysis of Variance
ASTM	American Society for Testing and Materials
CMOD	Crack Mouth Opening Displacement
COF	Coefficient of Friction
CGI	Compacted Graphite Iron
Cr-Mo	Chromium-Molybdenum
CPE8R	Eight Node biquadratic Plain Strain Quadrilateral, reduced Integration
C3D8T	Eight Node Thermally coupled brick Trilinear displacement and Temperature
DCI	Ductile Cast Iron
ERR	Energy Release Rate
FEA	Finite Element Analysis
Fe-Si-Mg	Fero Silicon Molybdenum
FEM	Finite Element Method
FG	Flakes Graphite
GCI	Grey Cast Iron
HV	Vickers Hardness
J-C	Johnson-Cook
LCF	Low Cycle Fatigue
LVDT	Linear Variable Differential Transformer
NCI	Nodular Graphite Iron
RE	Rare Earth
SENB	Single Edge-Notched Beam

SEM	Scanning Electron Microscope
SGI	Spheroidal Graphite Iron
SiCu	Silicon Copper
SIF	Stress Intensity Factor
SiMo	Silicon Molybdenum
SiMoCr	Silicon Molybdenum Chromium
SSFDI	Solution Strengthened Ferritic Ductile Iron
TG	Temper Graphite
UTM	Universal Testing Machine
UTS	Ultimate Tensile Strength
VHN	Vickers Hardness Number
WEDM	Wire-Cut Electrical Discharge Machining
EdX	Energy Dispersive X-Ray
YS	Yield Strength

NOMENCLATURE

a	initial crack length
A	Yield strength of the material under referenced conditions
A_R	Brake disc surface area
B	Strain hardening constant
C	Strain rate strengthening coefficient
C_R	Specific heat of the brake disc material
E	*Y*oung's modulus
d	Sliding distance
$\dot{\varepsilon}^*$	Dimensionless ratio of strain rate to the reference strain rate
ε_{eq}	Equivalent plastic strain
F	Deforming force in three point bend test
J	*J*-integral value obtained from the FE analysis
n	Strain hardening exponent
C_{eq}	Carbon equivalent
h_R	Heat transfer coefficient
K_{IC}	Plain strain fracture toughness
K_a	Thermal conductivity of air
k	Specific wear rate
m	Thermal softening co-efficient
q_0	Braking power absorbed by the disk brake
R_e	Reynolds number
S	Span length of three point bend test specimen
T^*	Homologous temperature
t_s	Braking time to stop
t_c	Approximate cooling cycle time
v	Poisson's ratio
ν	Sliding velocity
V	Wear volume
V_R	Brake disc volume

W	Height of three point bent test specimen
$W_{Fe\text{-}Si\text{-}Mg}$	Weight of Fe-Si-Mg (Kg)
W_{ladle}	Weight of melt in ladle (Kg)
Mg_f	%wt. in melt after treatment
$\%Mg_{Fe\text{-}Si\text{-}Mg}$	% wt. of Mg in Fe-Si-Mg alloy
S_i	% wt. of initial sulphur content in melt
S_f	% wt. of final sulphur content in melt after magnesium treatment
t	Time taken in magnesium treatment(minutes)
T	Temperature of melt (°C)
R	Yield of mg during magnesium treatment
σ_{eq}	Equivalent flow stress
σ	Standard deviation of responses
μ	Coefficient of friction
ρ, ρ_R	Density of the material
μ_a	Kinematic viscosity of air

CHAPTER 1

INTRODUCTION

1.1 Cast iron

Day by day incessant trends and escalating functional obligations of useful products and structural motifs enforcing the developers to develop more effective and efficient materials. Low-cost lightweight designs coupled with sustainable energy and environmental contemplation are the major need for improving efficiency and optimizing the utilization of energy resources. To meet such demands continuous research is going on for enhancing the properties and developing the new materials. The essential parts of enhancement and development of such engineering materials are the lower cost and shorter lead time without disturbing the mechanical properties and structural integrity.

As a manufacturing process, casting has more potential in this area with the development of new grades of cast iron to tackle the surge. Nodular graphite cast iron / Spheroidal graphite cast iron (SGI), among the available cast iron grades, provides an attractive combination of mechanical properties and castability at a lower cost, considered as a replacement for steels in numerous applications, especially the first and second generation of ductile cast irons (DCI) viz. ferritic-pearlitic and high silicon-based solution strengthened ferritic ductile cast irons (SSFDI) as specified in EN1563:2018 standards. These two grades of DCI are considered as the most important among the available types of cast iron due to their excellent mechanical properties and good castability in complex sections with relatively lower cost.

Some challenges like limited elongation and difficulty in machining due to variation in hardness owing to ferritic-pearlitic matrix thus restricted the use of these DCI grades to

specific applications only. On the other hand, SSFDI has made some improvements and overcome such challenges to an extent. However, this momentum of improvements in DCI grades must be continued by understanding and researching to enhance the mechanical properties for the fulfillment of the market demand. This means that continuously pushing the limits on the current properties of DCIs is necessary for the development of these grades with higher strength and elongation without adverse effects on the environment, economy, or any production disadvantage. The current available DCI grades are becoming the base for further investigating the possibilities for improved strength as well as elongation of the material.

It is noteworthy to mention that the matrix of the castings responsible for mechanical properties is influenced by the alloying elements, casting methods, solidification process and heat treatment. To achieve desired properties, the solidification process of casting is an economical way of acquiring the requisite microstructure using apt control of alloying elements in contrast with the costly post-solidification heat treatment. More focused research on the solidification method by controlling the composition of alloyant for achieving the as-cast high strength, higher elongation and better wear properties will become the base for this study. The present research is focused on the development of a SiMoCr DCI, by varying the main alloyant percentage for achieving higher tensile strength as well as elongation alongwith good wear properties.

1.2 Purpose

Most of the available grades of DCIs either have higher strength at the cost of reduced elongation or higher elongation with lesser strength. The SSFD iron shows superior mechanical properties as compared to the other available DCIs, but this superiority drastically deteriorates when the percentage of silicon increases beyond the limits

discussed by Alhussein et al., (2014). The purpose of this thesis is to develop a DCI by varying the percentage of alloyant in iron. A set of three heats are prepared in an induction furnace with the selected combinations of alloying elements and the developed material is distinguished from the other available DCI materials by labeling it as SiMoCr ductile cast iron (SiMoCr DCI). Microstructure analysis of SiMoCr DCI is done for analyzing the alloying element's effect on the microstructure of the developed material. Mechanical testing of SiMoCr DCI is done for observing the effects of alloying elements on the tensile strength, elongation and hardness of the developed material.

The three-point bend test will be done for finding the effects of alloying elements on the fracture toughness of SiMoCr DCI. The experimental results of fracture toughness will be verified with the finite element analysis.

The pin-on-disc wear test on the wear disc against pin made from brake pad material will be carried out for finding the sliding wear parameters of the developed material using Taguchi L_{16}. The specific wear rate and coefficient of friction data obtained from the test will be optimized using statistical analysis.

The brake disc made from developed material will be tested against a brake pad in real world situations using a brake test rig setup. The surface wear and temperature evolved during intermittent braking will be compared with the finite element analysis.

The major objectives of this research are listed in para 3.7 of Chapter 3.

In short, the target of this research is to develop a feasible alloy of DCI having higher tensile strength coupled with higher elongation, toughness alongwith good wear properties.

1.3 Approach

A systematic approach for addressing the problem statement of this thesis includes exhaustive research and literature assessment consisting of available studies on the various DCI grades. The systematic approach starts with a detailed study of the available literature to familiarize with the concepts of developing the standard grade DCIs. The historical background of the available DCI grades is detailed down in the literature review chapter in a thematic way to examine the research conducted for the present DCI grades and the factors responsible for the requisite mechanical properties. Further emphasis would be given on the challenges of the available DCI grades, the opinion of the researchers on such challenges, role of alloying elements in affecting the microstructure of the melt. The results of this study should be summarized to propose alternate effective composition of the melt which would be developed experimentally and characterized using standard tests. The step-by-step solution approach of the thesis is summarized in the following order.

1. Exuberant review of the presently available literature of standardized grades of DCI. Detailed assessment of the challenges and effect of alloying elements on the microstructure and properties of such grades.
2. By considering the extract of the vigorous review in previous step, interpretations of the material parameters supportive for high tensile strength, elongation as well as good wear properties, alloying elements would be selected to produce the SiMoCr DCI possessing high tensile strength, elongation and good wear properties.
3. Three proposed compositions of SiMoCr DCI is be selected based on the outcomes of previous step to achieve the desired properties. Control over the alloying elements percentage in composition is an essential activity of this step.

4. Development of the SiMoCr DCI by melting in an induction furnace and characterization of the material properties through study of microstructure and mechanical testing.

1.4 Structure of thesis

The structure of this thesis is comprising of several chapters described below:

Chapter 1: Introduction

Chapter 2: Theoretical background

Chapter 3: Literature review

Chapter 4: Development of SiMoCr DCI

Chapter 5: Evaluation of Johnson-Cook material model parameters

Chapter 6: Evaluation of Fracture toughness

Chapter 7: Evaluation of wear parameters

Chapter 8: Experimental and numerical investigations of a brake disc

Chapter 9: Conclusions and future scope

CHAPTER 2

THEORETICAL BACKGROUND

2.1 Cast iron

Cast iron is considered as the first man-made composite of iron and alloying elements, produced around the world for more than 2000 years, and has a share of more than 70% of world tonnage of casting material (Stefanescu, 2005). The competitive cost, mechanical and physical properties are the main rationales for the domination of cast iron among other cast materials. The cast iron properties are determined by tensile testing and microstructural examinations. The microstructures of cast iron are formed and mostly reliant on the material's structure for enhancing the mechanical properties and overall characteristics of the iron. The cast iron solidification liable to the composition as well as the cooling rate may follow either a thermodynamically metastable eutectic path for the formation of the iron-iron carbide phase system or the stable eutectic path for the formation of the iron-graphite phase system. The graphitization potential (nucleation potential of the liquid melt, its composition) of iron and the cooling rate of the liquid melt are the factors responsible for the formation of stable or metastable eutectics. Higher graphitization potential of iron results in iron with a rich carbon phase (graphite) while the lower graphitization results in iron with iron carbides. In general Cast iron consists of above 2.14% carbon content while in practice it contains 3.0-4.5 %wt. carbon as shown in Fig. 2.1 as commercial cast iron and contains other alloying elements specifically silicon depending on the applications. During melting, the carbon concentration in the melt reduces the iron's melting temperature to the eutectic point 1150℃ – 1300℃, substantially lesser in comparison to steel and improves the castability rather easy with this fluidity.

Adding the other alloying elements viz. silicon in cast iron productions may further affect the carbon solubility in the austenitic matrix and result in a eutectic matrix with a carbon percentage lower than 2 %wt. The desired properties of cast iron are achieved by manipulating the contents, quantity and eutectic morphology.

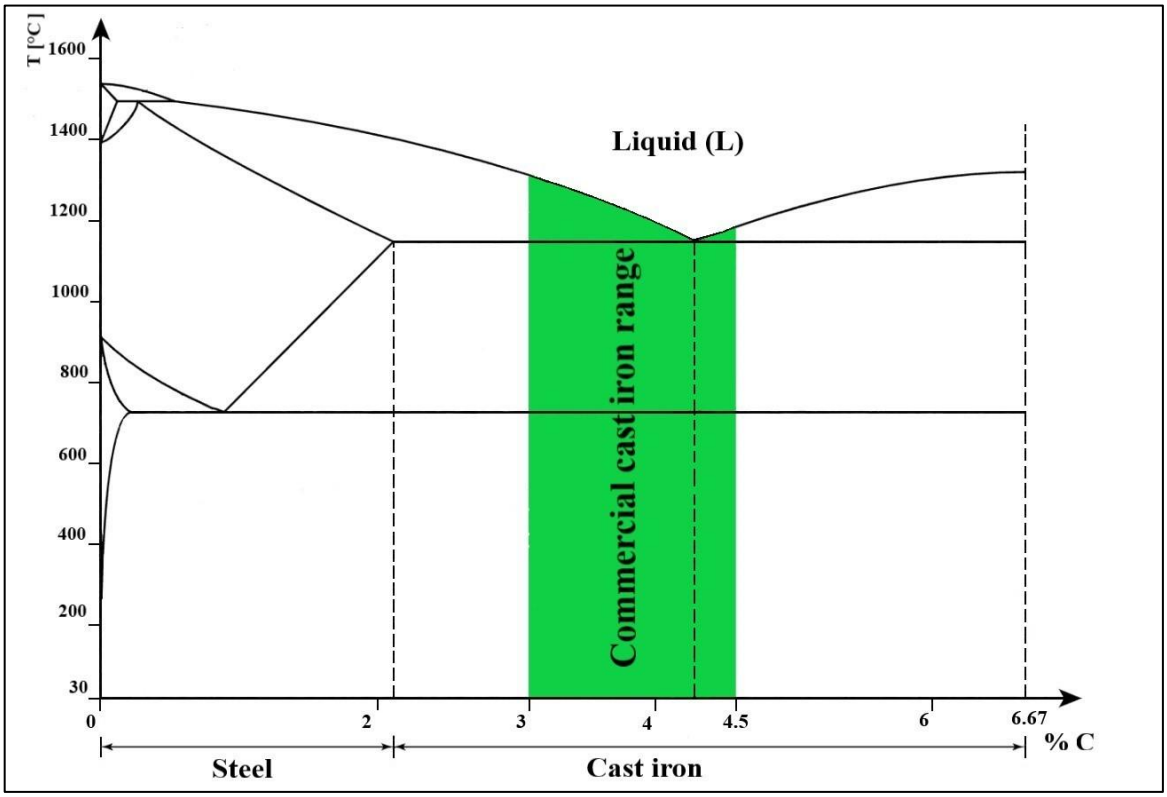

Fig. 2.1 Iron-iron carbide diagram (Okunnu, 2015)

2.2 Cast iron- classification

The general classification of cast iron based on metallurgical characteristics is given in Fig. 2.2. However, cast iron can be classified based on (i) fracture, (ii) graphite shape, and (iii) phase matrix. Based on fracture, cast iron is grouped as white cast iron and grey cast iron, while based on graphite shape, it is classified as lamellar (flakes) graphite (FG), compacted (vermicular) graphite (CG), spheroidal or nodular graphite (SG/NG) and temper graphite (TG). Austenitic, ferritic, pearlitic, martensitic and bainitic cast iron are the classifications based on phase matrix. In addition to these, cast iron is also classified

as low alloy and high alloy cast iron for general applications and specific applications respectively.

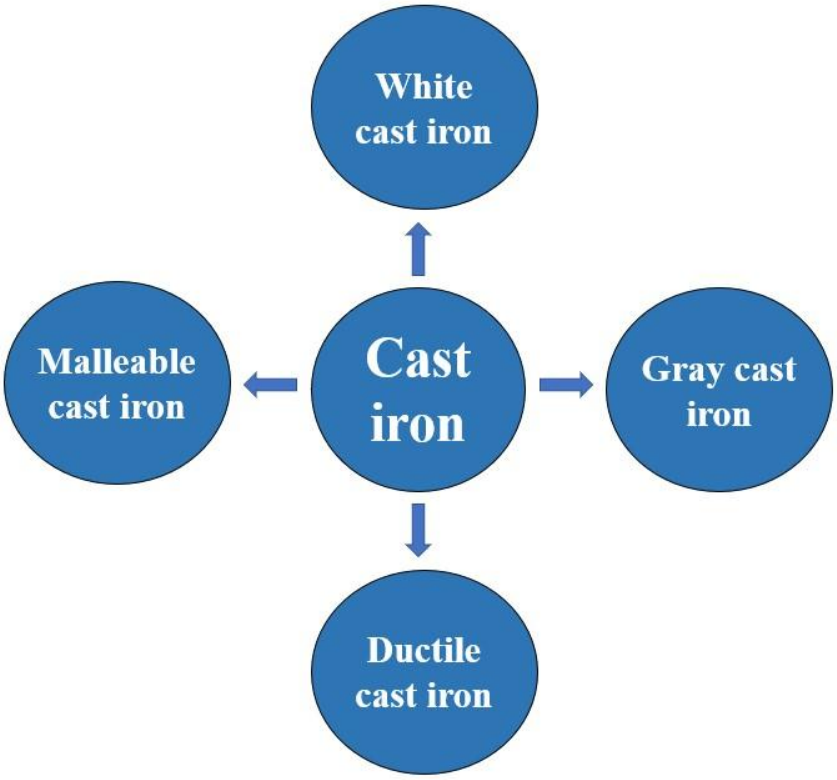

Fig. 2.2 Classification of cast iron

The classification given in Fig.2.2 categorizes the cast irons in terms of the solidification process and microstructure obtained. Flaky graphite, either in a pearlitic or ferritic matrix, distinguishes grey cast iron and makes it more brittle due to stress raisers at the flakes' notches. In the case of ductile or nodular cast iron, the treatment of liquid melt using magnesium/cerium/yttrium converts the flaky shape of graphite into a spheroidal or nodular shape with either pearlitic or ferritic matrix during the process known as "nodularization". The spheroidal shape of graphite nodules eradicates the stress notches making it ductile when compared to the other form of cast iron. Due to the presence of carbon, primarily in the form of cementite, the other variety of cast iron, known as white cast iron, is even more brittle. The final variety of cast iron, known as vermicular or compacted-graphite iron, shows the combined microstructural characteristics of both grey

and ductile irons. Ductile cast iron is the most commonly used form of cast iron worldwide due to its edge over the other types of cast iron by having some good mechanical properties as that of steels. For example, Ductile cast iron has achieved its highest tensile strength as high as 900 MPa (EN-GJS-900-2), or the elongation could reach upto 18% (EN-GJS-400-18), and good impact properties, including good impact properties under low-temperature conditions. Furthermore, it might have its physical characteristics greatly improved with the right heat treatment. As this study is restricted to the study of ductile cast iron only, the other types of cast irons are not elaborated here.

2.3 Ductile cast iron

Cast iron that is produced by adding rare earth materials or magnesium to the molten melt to convert the graphite flakes into spheroidal or nodular form is known as ductile cast iron (DCI), also known as nodular cast iron (NCI), or spheroidal graphite iron (SGI). The DCI's microstructure is controlled by the sequence of solidification and the content of the alloying elements in the melt, leading to a wide range of ductile iron grades that are accessible for various uses. As inferred by the name, DCI has a considerably higher tensile elongation and sufficient strength than grey irons because of the form of graphite nodules in the matrix. As compared to flaky graphite notches in grey iron, which operate as stress concentrators, the spheroidal shape of graphite acts as a dislocation inhibitor due to the ratio of surface area to volume. Nodule count, matrix structure, and "nodularity" are the micro constituents of ductile cast iron, and they each have a considerable impact on the iron's qualities either alone or in a blend. The nodularity index of the DCI serves as the foundation for mechanical qualities, including elongation and toughness. Increased nodule counts, a result of successful ductile cast iron inoculation, are crucial for meeting particular mechanical property criteria. Effective inoculation limits the production of

brittle white iron structures below the metastable eutectic temperature during solidification, supplying sufficient nucleation spots for the dispersed carbon to form the graphite matrix instead of the cementite matrix. Depending upon the form of cast iron produced or the behaviour of the alloys in the melt, the inoculants addition may be done either in the treatment ladle or in the mould. The percentage proportion of ferrite and pearlite in the material's structure regulates the strength of the material. The pearlitic matrix that alternates layers of ferrite and cementite makes up the majority of as-cast ductile cast iron. Through heat treatment or the right alloying composition, the ferritic matrix, which represents the pure phase of iron, is produced. While pearlite has great strength and hardness but low ductility, the ferritic matrix has lesser strength and hardness, however comparatively higher values of toughness and ductility. Through carefully managed heat treatment, composition control, or solidification order, both types of structures can be created in ductile cast iron totally or in a shared ratio. The three possible ductile cast iron microstructures, as shown in Fig. 1.3, (Okunnu, 2015), have a common feature as nodular graphite.

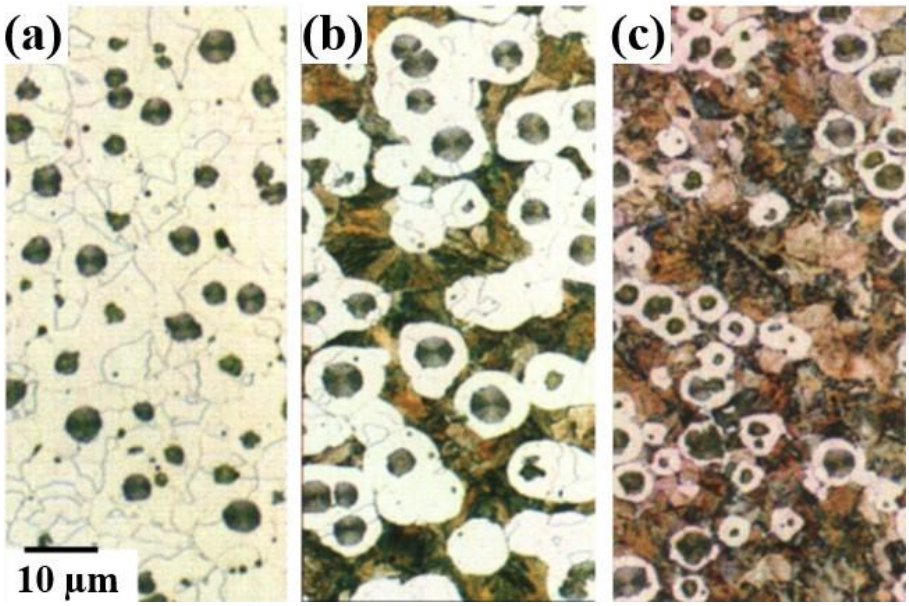

(a) Fully ferritic, (b) ferritic-pearlitic, (c) fully pearlitic matrix

Fig. 2.3 Typical microstructure of nodular cast irons (Okunnu, 2015)

2.4 Composition of ductile cast iron

DCI is a good contender for various applications where conjoined properties of strength and ductility are required. For instance, approximate double strength and higher elongation are observed in ductile cast iron in contrast to grey iron. According to the foundryman experience and according to the purity level of scrap metal used as charge material in castings, such qualities of ductile cast iron are related to the different chemical compositions. Generally speaking, ductile cast iron is composed of the following as main constituents: carbon (C), silicon (Si), manganese (Mn), sulphur (S), and phosphorus (P). Other alloying elements may be added to the mix, although this is entirely dependent on the applications, preferred microstructure, and probably unique foundry procedures. These alloying elements have advantages on their own and in combination with other elements in the charge when they are included in the base composition.

As a result, the final composition of the ductile cast iron depends upon the alloying elements. The solidification of the iron can be thus hypoeutectic DCI, hypereutectic DCI, or eutectic DCI. For differentiating among such types of ductile cast iron, the term carbon equivalence (C_{eq}) (Davis et al., 1996) is used to define the alloying element contribution in the form of carbon and the common C_{eq} equation used generally is given in Eq. 2.1 with only considering the effect of silicon. Although the most common formula with a greater number of alloying elements given in Eq.2.2(Stefanescu, 2018)

$$C_{eq} = \%C + \frac{\%\,Si}{3} \qquad \text{Eq. (2.1)}$$

$$C_{eq} = \%C + 0.28\%\,Si - 0.007\%Mn + 0.303\%P + 0.033\%Cr + 0.092\%\,Cu + 0.011\%Mo + 0.054\%Ni \qquad \text{Eq. (2.2)}$$

Due to its powerful support of the ferritic matrix and ability to increase hardness, tensile strength, and ultimate strength, silicon is a crucial alloying element. By promoting

graphite precipitation and raising the ductile-brittle transition temperature, it lowers the chilling tendency in cast iron and the solubility of carbon in the austenitic phase. A higher proportion of silicon in the composition increases ferrite strength while decreasing the alloy's resistance to impact. The cast also has high thermal oxidation resistance. Manganese levels below 0.2 %wt. should be preferred in as-cast alloys because they reduce the possibility of segregation at grain boundaries and encourage the formation of carbide and mild pearlite in the matrix. When choosing iron scrap for the melt, the presence of manganese, as well as silicon in the composition, is frequently a concern. Phosphorus content exceeding 0.05 weight percent in the melt increases the danger of segregation, encourages the formation of carbides or phosphide complexes, and elevates the temperature at which the iron transforms from ductile to brittle. A key requirement for nodularization is the inclusion of sulphur in ductile cast iron up to 0.015%wt., but the amount should be carefully controlled because either an excessive or inadequate percentage would impact the alloy's characteristics by promoting the creation of subpar and quasi-flaky graphite. The creation of ductile cast iron requires the careful addition of nodularizing materials such as magnesium (Mg)/ RE metals, which induce the graphite's notchy flakes to precipitate as spheroids. Ferro silicon magnesium (Fe-Si-Mg) is widely utilized today in the manufacturing of ductile iron castings with various section thicknesses and C_{eq} values due to its reduced cost and application to a wide range of castings. Therefore, it is essential to understand how to employ these alloying elements because their inappropriate inclusion could result in castings with undesirable qualities.

2.5 Ductile cast iron-family

Instead of being produced as a single material, ductile cast iron is instead produced as a set of adaptable materials with a varied selection of properties that are achieved with strict

microstructural control. The characteristic shared by all varieties of ductile cast iron is the spheroidal form of the graphite nodules. The DCI with such spheroids in the matrix is more ductile and tougher than the rest of the cast iron types and at par with the few types of cast and forged steel. The consistency and quality of ductile cast iron rely on this property. The DCI's mechanical properties are greatly enhanced with the presence of a higher percentage of graphite spheroids in the matrix. The designations given to the following varieties emphasize the importance of the matrix in determining the DCI's mechanical qualities.

- Ferritic ductile cast iron – The graphite nodules of spherical shapes are homogeneously packed in the ferritic matrix as shown in Fig. 2.3(a). The primary characteristics are high ductility, impact resistance, and yield and tensile strengths comparable to those of low-carbon steel. For many engineering applications, ferritic ductile cast iron is often manufactured as-cast, although the ductility and low-temperature toughness can be increased by annealing.
- Pearlitic ductile cast iron – Fig. 2.3(c) shows the graphite nodules in the pearlitic matrix which results in good strength, reasonable ductility, wear and impact resistance. In comparison to steels with similar physical qualities, machinability is also superior.
- Ferritic pearlitic ductile cast iron – The most popular type of DCI is ferritic pearlitic, and it is often formed in ‘as-cast’ state. Fig. 2.3(b) shows the nodules of graphite in ferrite -pearlite matrix as shown. With improved machinability and lesser production costs, the properties vary amid different ferritic and pearlitic grades.

The types of DCI mentioned above are commonly utilized in 'as-cast' conditions, however the DCI can be categorized as a few more grades for the fulfillment of a wide range of additional specific applications.

- Martensitic ductile cast iron – is manufactured by quenching and tempering the cast iron after adding enough alloy to prevent the production of pearlite. The tempered martensite matrix that forms, as a result, has lower levels of toughness and ductility but very high levels of strength and wear resistance.
- Bainitic ductile cast iron –is produced by heat treating the ductile cast iron at a specific temperature range to promote the formation of bainitic microstructures. This heat treatment process helps to improve the mechanical properties of the material, particularly its strength and toughness while maintaining its ductility.
- Austenitic ductile cast iron –austenitic matrix is formed. It has strong magnetic characteristics, good strength, and is dimensionally stable at high temperatures. It shows good resistance to corrosion and oxidation as well.
- Austempered ductile cast iron (ADI) – is a type of cast iron that has been heat treated to produce a unique combination of high strength, ductility, and toughness. The process involves austenitizing the cast iron at a high temperature, followed by quenching it in a bath of molten salt and then holding it at a lower temperature in a furnace to allow the transformation of the austenite into a bainitic structure. The resulting material has a microstructure of bainitic, ferrite and stabilized austenite, which gives it the desirable mechanical properties.

2.6 Grades of Ductile Cast Iron

Ductile cast iron is used worldwide in various engineering applications with different compositions of additives in nodular cast iron. Depending upon the composition of the

material various grades of DCI are available in the market. A brief detail of various grades of DCI is given in Table 2.1.

Table 2.1 Equivalent Grades of DCI

ISO ISO 1083	USA ASTM A536	India IS 1865	European EN 1563
400-15	60-40-18	SG370/17	EN-GJS-400-15
400-18			EN-GJS-400-18
450-10	60-42-10 65-45-12	SG400/12	EN-GJS-450-10
500-7	70-50-05	SG500/7	EN-GJS-500-7
600-3	80-55-06 80-60-03	SG600/3	EN-GJS-600-3
700-2	100-70-03	SG700/2	EN-GJS-700-2
800-2	120-90-02	SG800/2	EN-GJS-800-2
900-2	-	-	EN-GJS-900-2

Source: https://www.iron-foundry.com/china-ductile-iron-castings.html

In engineering applications strength and ductility both are required. The desired composition of these grades varies in accordance with the ASTM Standards D1976, E351, E1999, E1184 and D5381. It is seen clearly from Table 2.1 given above that the tensile strength of SG Iron increases only on the sacrifice of percentage elongation. But in some applications, it is desired to have both tensile strength and elongation even at high

temperatures. For that, it is desired to develop a material having both strength and elongation even at higher temperatures. Delprete and Sesana (2014) studied the behaviour of SiMoCr ductile cast iron at different temperatures and found that the alloy shows good monotonic properties at low temperatures but is seen to be fragile during fatigue tests due to high Silicon content in the alloy. The mechanical properties are found still be good at 500℃ with an average 40% decrease as compared to the low-temperature strength with increased ductility. At higher temperatures (800℃) the alloy becomes soft with a noticeable decrease in strength.

2.7 Properties of Ductile Cast Iron

The mechanical behaviour of DCI has historically been predicted most often using the yield and tensile strengths as well as the elongation of the material. The majority of the global specifications for DCI define the qualities of the various classes primarily in terms of their corresponding yield, tensile, and elongation strengths. Most specifications are completed by hardness values, which are typically provided as supplementary data, and impact properties, which are only given for specific ferritic grades. Additional crucial design parameters include the ductile cast iron's proportional limit and elastic modulus. It is important to note that the properties of ductile cast iron may vary depending on the manufacturing process, heat treatment, and other factors. The actual properties of a specific grade of DCI should be obtained from the manufacturer's data sheet or technical specifications.

- Modulus of elasticity – also known as Young's modulus, is a measure of a material's stiffness or ability to resist deformation under stress. It is defined as the ratio of the stress applied to the material to the resulting strain in the direction of the applied stress. It is important to note that the modulus of elasticity of ductile

cast iron may vary depending on the manufacturing process, heat treatment, and other factors. Generally, the modulus of elasticity of DCI ranges from 62 to 170 GPa (Satyendra, 2014).

- Poisson’s ratio – is a measure of the ratio of the lateral strain to the axial strain when a material is subjected to tensile or compressive stress. In other words, it describes the tendency of a material to contract in the direction perpendicular to the applied force. A low Poisson's ratio indicates that the material has a limited tendency to contract laterally when subjected to axial stress and is therefore considered to be relatively stiff in the transverse direction. Generally, the Poisson's ratio of DCI is relatively low, typically 0.275 (Satyendra, 2014).
- Proportional limit – depends on the grade of the material and its microstructure. The proportional limit is the maximum stress that a material can withstand without exhibiting permanent deformation and is typically determined using a tensile test. Beyond the proportional limit, the material will begin to deform plastically, which means that it will exhibit permanent changes in shape or size. Generally, the proportional limit of DCI ranges from 200 to 400 MPa.
- Yield strength – The yield strength of ductile cast iron (DCI) depends on the grade of the material and its microstructure. The yield strength is the stress at which a material begins to exhibit plastic deformation or permanent strain and is typically determined using a tensile test. Beyond the yield strength, the material will continue to deform plastically, which means that it will exhibit permanent changes in shape or size. Generally, the yield strength of DCI ranges from 275 MPa for ferritic grades to over 620 MPa for martensitic grades (Satyendra, 2014).
- Tensile strength – depends on the grade of the material and its microstructure. It is the maximum stress that a material can endure just before the fracture or breaks

during a tensile test. It shows the maximum resistance of the material under the application of load to pull it apart or stretch. It is important to note that the tensile strength of ductile cast iron may vary depending on the manufacturing process, heat treatment, and other factors. Generally, the tensile strength of DCI ranges from 400 to 800 MPa.

- Elongation – depends on the grade of the material and its microstructure. Elongation means the plastic deformation a material undergoes during a tensile test. It is expressed as the percentage increase in the length of the sample after it has been stretched to its breaking point. A higher elongation indicates that the material is more ductile and can deform more before breaking. Generally, the elongation of DCI is around 2-18%.
- Hardness – depends on the grade of the material and its microstructure. It is the measure of a material's resistance to deformation, particularly to scratching, indentation, or abrasion. It is often measured using the Brinell hardness test, which includes the surface indenting of the material with a steel ball and measuring the diameter of the resulting indentation. DCI typically has a hardness of around 130-360 Brinell hardness.
- Impact resistance – varies with the grade of the material and its microstructure, as well as other factors such as the geometry and size of the component. It is the ability of the material to absorb energy and resist breakage under high strain rates, such as those that occur during impact or shock loading. It is often measured using a Charpy or Izod impact test, which includes the striking of a notched sample with a force pendulum and records the energy absorbed by the sample before it fractures. Generally, DCI has good impact resistance due to its high toughness and ductility.

- Density – depends on the grade of the material and its microstructure. Mass per unit volume is generally considered as the density of the material. It is a valuable property for engineering applications because it can affect the weight, strength, and performance of a component. Generally, the density of DCI is around 6.9 g/cm3(Satyendra, 2014).
- Thermal expansion – varies with the material's grade and its microstructure, as well as other factors such as the temperature range and heating/cooling rates. Material's tendency to expand or contract with temperature changes is considered as thermal expansion. It is an important property for engineering applications because it can affect the dimensional stability and performance of a component. Generally, the coefficient of thermal expansion of DCI is around 10-12 × 10-6/°C.
- Heat resistance – depends on the grade of the material, its microstructure, and the specific application conditions. Heat resistance is termed as the material's ability to resist degradation or deformation when exposed to high temperatures. It is an important property for engineering applications that involve high-temperature environments, such as furnace components or exhaust manifolds. The heat resistance of DCI can be improved using heat-resistant alloys, surface treatments, or other materials modifications. Generally, DCI has good heat resistance up to temperatures of around 600-700°C, but its properties can degrade rapidly at higher temperatures.
- Thermal conductivity – depends on the grade of the material and its microstructure, as well as other factors such as the temperature range and heating/cooling rates. A material's ability to conduct heat is termed as thermal conductivity. It is a valuable property for engineering applications because it can

affect the heat transfer and performance of a component. Generally, the thermal conductivity of DCI is around 40-50 W/m-K.

- Electrical resistivity – depends on the grade of the material and its microstructure, as well as other factors, for instance, the temperature and the occurrence of impurities. Electrical resistivity is considered as the material's ability to resist the electrical current flow through it. It is an important property for engineering applications that involve electrical components or circuits. Generally, the electrical resistivity of DCI is around 80-90 Ω-m at room temperature.
- Magnetic properties – DCI exhibits magnetic properties due to the presence of iron in its composition. The magnetic properties of DCI depend on the grade of the material, its microstructure, and other factors such as the presence of other alloyant elements. DCI can be categorized as either ferritic or austenitic based on its microstructure, and this can affect its magnetic properties. Ferritic DCI is typically magnetic, while austenitic DCI can be either non-magnetic or weakly magnetic depending on the specific alloying elements present and their concentrations. The magnetic properties of DCI can be measured using techniques such as magnetic susceptibility or magnetic induction.
- Specific heat – depends on the grade of the material, its microstructure and the specific temperature range of interest. The material's ability to absorb or release heat as its temperature changes is termed as specific heat. It is an important property for engineering applications that involve heat transfer or thermal cycling. Generally, the specific heat of DCI is around 0.46-0.50 J/g-K at room temperature.
- Wear resistance – DCI exhibits good wear resistance due to its microstructure and composition. DCI has a combination of high hardness and toughness, making it suitable for applications where wear and impact resistance are important. The

wear resistance of DCI depends on several considerations, for instance the grade of the material, the specific application and operating conditions, and the kind and severity of the wear mechanism. It can be further improved through heat treatment, surface coatings, or other treatments. Several methods can be used to measure the wear resistance of DCI, such as pin-on-disk tests or abrasive wear tests. Overall, DCI is a commonly used material in applications where wear resistance is critical, such as in automotive components, machinery parts, and mining equipment.

- Corrosion resistance – DCI exhibits good resistance to corrosion in many environments due to its composition and microstructure. The graphite nodules in DCI act out as a barrier to inhibit the penetration of corrosive agents, while the matrix provides a protective layer against corrosion. It depends on several aspects such as the grade of the material, the specific application and operating conditions, and the type and severity of the corrosive environment. In some aggressive environments, such as acidic or alkaline solutions, the corrosion resistance of DCI may be limited. The corrosion resistance of DCI can be further enhanced through the use of protective coatings, inhibitors, or other treatments. For example, epoxy coatings can provide a barrier against corrosive agents, while cathodic protection can be used to prevent corrosion by controlling the electrochemical reactions. Several methods can be used to measure the corrosion resistance of DCI, such as salt spray tests or immersion tests. The actual corrosion resistance of a specific grade of DCI should be obtained from the manufacturer's data sheet or technical specifications. Overall, DCI is a commonly used material in applications where corrosion resistance is important, such as in marine components, pipes, and valves.

2.8 Effect of Inoculation

Inoculation is a process of adding up small volumes of certain elements to the molten metal to promote the formation of graphite nodules during solidification during the preparation of DCI. The addition of these elements, such as magnesium or Rare Earth (RE) metals (cerium/yttrium, etc.), increases the number of nucleation sites for graphite, resulting in a more uniform and fine-grained microstructure.

Inoculation has several effects on the properties of DCI, including:

1. Improved mechanical properties: Inoculation can enhance the DCI's strength, ductility and toughness by promoting the formation of a more uniform and fine-grained microstructure.
2. Reduced shrinkage defects: Inoculation can reduce the risk of shrinkage defects, such as porosity or shrinkage cavities, by promoting the formation of graphite nodules.
3. Enhanced wear resistance: Inoculation can improve the wear resistance of DCI by promoting the growth of a more uniform and fine-grained microstructure, which reduces the risk of surface cracks and other wear mechanisms.
4. Improved machinability: Inoculated DCI is easier to machine than un-inoculated DCI due to its more uniform and fine-grained microstructure.

The effect of inoculation on DCI properties varies with numerous factors, such as the structure and quantity of inoculant used, the base material composition, and the specific application of the material. Improper inoculation or fading of inoculation leads to insufficient nuclei for dendritic structure formation resulting in poor spheroids, lesser nodule counts, development of carbide chills, etc.

2.8.1 Effect of Shape of Graphite

The shape of graphite nodules in DCI significantly influences the properties of the material. DCI can have several different types of graphite shapes, including spheroidal, compacted, and vermicular, depending on the constituents and development of the material.

The nodule's shape alters the mechanical properties of DCI in the following ways:

1. Strength: DCI with spheroidal graphite nodules has higher strength than DCI with vermicular or compacted graphite nodules.
2. Ductility: DCI with vermicular or compacted graphite nodules has higher ductility than DCI with spheroidal graphite nodules.
3. Toughness: DCI with vermicular or compacted graphite nodules has higher toughness than DCI with spheroidal graphite nodules.
4. Fatigue resistance: DCI with spheroidal graphite nodules has higher fatigue resistance than DCI with vermicular or compacted graphite spheroids.

The graphite nodules shape also affects the machinability of DCI. DCI with spheroidal graphite nodules is easier to machine than DCI with vermicular or compacted graphite nodules due to its smoother surface and a lower tendency to form surface cracks.

The type of graphite shape in DCI is influenced by numerous factors, including the constituents of the alloy, the alloy's cooling rate throughout the solidification process, and the inoculation process. The choice of graphite shape varies with the specific application of the DCI and the requisite mechanical properties. Overall, the shape of graphite nodules plays an important role when designing and producing DCI for different applications.

2.8.2 Effect of Nodularity

The nodule count or nodularity of DCI referred as the amount of graphite nodules present in the microstructure of the material. The nodularity of DCI can have a substantial influence on its mechanical properties.

Increasing the nodule count in DCI generally results in the following effects:

1. Strength: DCI with a higher nodule count has higher strength due to the increased number of graphite nodules acting as crack-stoppers in the material.
2. Ductility: DCI with a higher nodule count has higher ductility attributable to the reduced size and volume fraction of graphite nodules in the microstructure.
3. Toughness: DCI with a lower nodule count has lower toughness due to the reduced number of crack-stoppers in the material.
4. Machinability: DCI with a higher nodule count is more difficult to machine due to the increased hardness and abrasiveness of the graphite nodules.

The nodule count of DCI can be influenced by various aspects, including the constituents of the alloy, the cooling rate during solidification, and the inoculation process. The choice of nodule count varies with the specific application of the DCI alongwith the desired mechanical properties. Overall, the nodule count is an important factor to consider when designing and producing DCI for different applications.

2.9 Wear Resistance

DCI is known for its excellent wear resistance properties owing to the existence of graphite nodules and a hard matrix. The wear resistance of DCI can be influenced by numerous factors in addition to the constituents of the alloy, the microstructure, and the type of wear. DCI exhibits excellent wear resistance in applications where it is subjected to sliding or abrasive wear. The graphite nodules in DCI act as solid lubricants, reducing friction and wear. The matrix material of DCI is typically a combination of ferrite and pearlite, which provides good wear resistance owing to its hardness.

The wear resistance of DCI can be further enriched by adding up the various alloying elements such as chromium, molybdenum, nickel and copper. These elements can

increase the hardness and corrosion resistance of the material, resulting in improved wear resistance. The microstructure of DCI can also have an impact on wear resistance. A fine and uniform microstructure with a high nodularity typically improves the wear resistance by virtue of the increased number of graphite nodules acting as crack-stoppers in the matrix. Overall, DCI is a preferred choice for the components like gears, bearings, etc, where wear resistance is critical.

2.10 Specific Wear Rate of DCI

The specific wear rate (k), typically expressed in terms of volume or weight loss, is a measure of the amount of surface material removed from a surface per unit of sliding distance. There are numerous factors that affect the specific wear rate of ductile cast iron including the coefficient of friction, the sliding velocity, the applied load, and the properties of the rubbing material. The specific wear rate of ductile cast iron can vary with changes in several factors, including the microstructure, surface finish, load, speed, and lubrication. In general, DCI has a low specific wear rate owing to the presence of graphite nodules, which play the role of solid lubricants and reduce friction and wear. The microstructure of DCI, particularly the size and allocation of the graphite nodules, can have a meaningful impact on the specific wear rate.

Studies have shown that increasing the nodularity of DCI can result in a lower specific wear rate owing to the increased number of graphite nodules and improved distribution of the nodules. Other factors, such as the use of proper lubrication and surface finish, can also reduce the specific wear rate. The specific wear rate of DCI also varies with the type of wear mechanism. For example, DCI exhibits excellent wear resistance in applications where it is subjected to sliding or abrasive wear. However, it may exhibit a higher specific wear rate in applications where it is subjected to impact or fretting wear.

In general, a higher specific wear rate indicates greater material loss and reduced durability of the ductile cast iron component. A higher coefficient of friction between two surfaces in contact can lead to increased wear and a higher specific wear rate. Similarly, higher sliding velocities and applied loads can increase the specific wear rate by generating greater frictional forces and stresses on the ductile cast iron surface. The specific wear rate is also be affected by the microstructure and other properties of the ductile cast iron, such as its hardness, strength, and ductility. Higher levels of these properties can improve the wear resistance of the ductile cast iron and may help in the reduction of the specific wear rate.

To improve the wear resistance of ductile cast iron components, various surface treatments can be used, such as coating, plating, or surface hardening techniques. These treatments can alter the surface properties of the ductile cast iron and reduce the specific wear rate under certain operating conditions. Overall, the specific wear rate of DCI is influenced by several factors and can alter broadly depending on the specific application and operating conditions.

2.11 Coefficient of friction of DCI

The coefficient of friction (COF) of ductile cast iron (DCI) can vary depending on numerous factors such as the surface finish, the kind of lubrication used, and the sliding conditions. One of the primary effects of the coefficient of friction on ductile cast iron is its wear resistance. A higher coefficient of friction between two surfaces in contact can lead to greater abrasion or erosion of the ductile cast iron surface, which can ultimately reduce its useful life. This is particularly relevant in applications where ductile cast iron is used as a wear-resistant material, such as in the production of engine components or mining equipment. On the other hand, a lower coefficient of friction between two

surfaces in contact can lead to increased adhesion or galling, which can also lead to premature wear or failure of ductile cast iron components. This is particularly relevant in applications where ductile cast iron is used in high-pressure or high-temperature environments, such as in piping or valve systems. In general, the coefficient of friction can be controlled through the use of lubricants or coatings, which can reduce frictional forces and enhance the wear resistance and durability of ductile cast iron components. The specific lubricant or coating used will differ with the specific application and the situations involved. Generally, the COF of DCI ranges from 0.1 to 0.5, depending on the testing conditions.

2.12 Benefits of Ductile Cast Iron

Ductile Cast Iron has several benefits that make it a trendy option for various applications.

Here are some of the key benefits of DCI:

1. High strength and durability: DCI has excellent strength and durability, making it suitable for use in demanding applications such as automotive and industrial machinery components.
2. Good machinability: DCI is easy to machine and can be shaped into complex geometries, making it a versatile material for various applications.
3. Excellent wear resistance: With higher wear resistance, DCI is suitable for use in applications where abrasive wear exists, such as gears, bearings, and brake components.
4. Good ductility and toughness: DCI has good ductility and toughness, which means it can withstand bending and impact without breaking, making it suitable for use in heavy-duty applications.

5. Good vibration damping: With good vibration damping properties, DCI is being suitable for use in areas where noise and vibration reduction are important, such as in engine blocks and brake components.
6. Good thermal conductivity: With good thermal conductivity, DCI disperse heat effectively, being suitable for use for components where higher temperature occurs, such as engine blocks and brake components.
7. Good corrosion resistance: DCI has good corrosion resistance, making it suitable for use in tough environments, such as marine and offshore components.

Overall, the blend of high strength, good machinability, excellent wear properties, good vibration dampening and thermal conductivity makes ductile cast iron a popular choice for various applications in the automotive, industrial, and marine industries.

2.13 Application of Ductile Cast Iron

Being a versatile material, DCI finds numerous applications in a wide range of industries. Some common applications of DCI include:

1. Automotive industry: DCI is used extensively in automotive parts such as engine blocks, cylinder heads, crankshafts, camshafts, brake discs, brake drums, suspension components, and steering knuckles.
2. Industrial machinery: DCI is used in the production of industrial machinery components such as gears, pulleys, rollers, and bearings owing to its exceptional strength and wear properties.
3. Oil and gas industry: DCI is used for valve bodies, pump components, and drilling equipment in the oil and gas industry due to its excellent corrosion resistance.

4. Water and sewage treatment: DCI is used in water and sewage treatment applications for pump housings, impellers, and valves due to its excellent corrosion resistance and low cost.
5. Marine industry: DCI is used in the marine industry for propellers, rudder components, and other marine hardware due to its excellent corrosion resistance.
6. Construction industry: DCI is used in the construction industry for drainage components such as manhole covers, grates, and frames due to its durability and corrosion resistance.
7. Railroad industry: DCI is used in the railroad industry for components such as brake shoes, couplings, and rail fasteners.

Overall, the unique combination of strength, ductility, wear resistance, corrosion resistance, and cost-effectiveness make DCI a popular choice for various applications in different industries.

2.14 Challenges of Ductile Cast Iron

Despite its many benefits, Ductile Cast Iron (DCI) also has some challenges, including:

1. Machinability: DCI can be difficult to machine owing to its high strength and abrasiveness, which may result in tool wear and high cutting forces. This can lead to longer machining times, increased tooling costs, and reduced productivity.
2. Brittle fracture: Although DCI is more ductile than grey cast iron, it can still exhibit brittle behavior under certain conditions, such as low temperatures or high-stress concentrations. This can lead to a catastrophic failure without warning.
3. Casting defects: DCI can be susceptible to casting flaws such as porosity, shrinkage, and insertions, which can compromise its mechanical properties and lead to premature failure.

4. Environmental concerns: The production of DCI involves the use of significant amounts of energy and resources, as well as the generation of waste products such as sand, dust, and emissions. This can have negative environmental impacts and raise concerns about sustainability.
5. Cost: While DCI can be a cost-effective material compared to alternatives such as steel or aluminium, its production costs can be influenced by factors such as raw material prices, energy costs, and labour costs.

The presently available grades of SG iron in the market either have good tensile strength or good ductility. The major challenge to the application of SG Iron is that it should possess both good tensile strength and ductility alongwith good wear resistance. The strength of SG iron at higher temperatures (800℃) also decreases which makes it unsuitable for high-temperature applications. Therefore, it is required to develop a DCI (SiMoCr ductile cast iron) which retains its properties even at higher temperatures.

CHAPTER 3

LITERATURE REVIEW

3.1 Ductile cast iron

A systematic attempt for accomplishing the thesis objectives is as much explorative as novel so that it discovers the potential of achieving the desired properties of SiMoCr DCI. But for doing so, it is necessary to understand the challenges experienced with the available grades of DCI and limitations of present methods for attaining such desired properties. The thematic approach of reviewing the existing views of the researchers for making the strategic solution is followed to get the essentials required to understand the inherent potentials and challenges of the DCI. This strategy also enhances the possibilities of improvement in DCI casting methods. Limited research has been done on SiMoCr DCI and found it inexpensive amongst the engineering materials. Such a situation is predictable to and precipitously changing, judging by interest and better understanding of the prospects of the SiMoCr DCI. Vigorous analysis of the effect of different alloyant on DCI structure and properties is studied and main findings are written in subsequent sections.

Çelik et al., (2011) has ran the engines with methonol at higher compression ratios at different load and speeds to meet the tough standards for environmental friendliness and fuel efficiency. These engines were generally smaller and ran at high temperatures and increased compression ratios. Papis et al., (2014) observed that the SiMo alloyed ductile iron used in turbo charged engine components did not effectively sustain the high temperature developed. In a study, Delprete and Sesana (2014) observed that the engine component like exhaust manifold has experienced the high temperature thermo-

mechanical stresses. The elasto-plastic behaviour of the developed alloy was found to be dependent on the temperature. During its study of SiMo iron with aluminium as an ingredient, Ibrahim et al., (2016) observed the carbide precipitation on grain boundaries within the pearlitic colonies due to presence of Al. An improved ultimate and yield strength with lower elongation and impact strength was observed. During the analysis of ferritic SiMo DCI, Hervas et al., (2015) found that upto 500℃, the mechanical properties were unaffected while at higher temperatures the nodule debonding affected the mechanical properties significantly. The compound of Mo and Mg segregation were observed at the grain boundaries during the crystallization study of SiMo DCI (Stawarz, 2017). Zeytin et al., (2009) found that the materials for engine components are exposed to heavy thermal and thermo-mechanical loadings and therefore the materials should possess high strength, fatigue, and scaling resistance at elevated temperatures. Chaengkham and Srichandr, (2011) observed that the cast iron containing high silicon (Si) and high molybdenum (Mo) meets the requirements and maintains dimensional stability during very high fatigue cycles at wide range of temperatures. A higher amount of Si promotes the ferritic structure by raising the austenitic transformation temperature. The SiMo DCI should have lower carbon content to promote fluidity and prevent defects like cold shuts and shrinkage. Lower toughness and ductility due to the presence of carbides and pearlite in the microstructure may be improved by heat treatment. González-Martínez et al., (2018) observed that the addition of antimony in the alloy reduces the formation of chunky graphite even though the alloy has higher Si content. Higher hardness, ultimate tensile strength, yield strength alongwith a sharp decrease in alloys elongation were also observed with higher Si content (Glavas et al., 2016; González-Martínez, et al., 2018). Nili Ahmadabadi et al., (2003) studied the temperature effect on ductile cast iron's hot formability using two different inoculant materials and found the reduction in

microporosity as well as shown the possibilities of making precision castings with minor graphite deformation. The ferrosilicon-based inoculants effectively minimize the chill formation and neutralize the subversive trace elements in the iron. Intercellular pearlite colonies, shrinkage porosity defects and carbide formation were also observed (Skaland, 2001). Heavy section castings with larger chunky graphite volume were observed with in-mould inoculation than the thinner sections. In-mould inoculation is also responsible for higher nodule counts (Ferrer et al., 2008). Thin-walled casting with eutectic and hypereutectic castings are observed with similar nodule counts in comparison to thick-walled castings (Pedersen & Tiedje, 2008). Nilsson and Vokál (2009) corelated the variation in ductility to casting defects and microstructure of the cast iron. During the life cycle assessment study of thin wall ductile cast iron for automotive application, Jhaveri et al., (2018) observed significant improvements. Weiß et al., (2018) conducted experimental studies on the effect of silicon content on the mechanical properties of DCI. It was concluded that a silicon content beyond 4.3% reduces the strength and ductility of DCI. Keough and Hayrynen, (2000) reviewed various applications where DCI effectively addressed the issues of weight, strength, noise cost, stiffness and recyclability. For improving the ductility of the material used in automobile suspension parts, Aranzabal et al., (2003) developed the ductile iron having mixed proeutectic ferrite and ausferrite structure, which shows good mechanical properties including ductility as well. During the camshaft fracture analysis, Bayrakceken et al., (2006) has concluded that casting defect played a significant role in failure of camshaft instead of the camshaft made from nodular cast iron. During the study of machining behaviour of pearlitic-ferritic nodular cast iron with cubic boron nitride tools, Grzesik et al., (2012) found significant improvement in surface finish. The automotive industry has expressed its confidence in DCI through extensive use in the components undergoing fatigue. A mixed proeutectoid ferrite and

ausferrite structure possessed properties between ferritic and pearlitic grades with high machinability and low production cost although the properties vary with heat treatments. Delprete and Sesana (2014) characterized the mechanical properties of a SiMoCr DCI containing a high amount of Cr and investigated to establish the alloy for high-temperature applications in automotive components. Borsato et al., (2019) investigated that increase of Si content promotes the formation of graphite in degenerated chunky shape alongwith an increase in tensile and yield strengths with reduced percentage elongation. Ferro et al., (2021) observed that increasing the solidification time renders the coarser microstructure with higher chances of porosity defects.

The casting sand plays a crucial role in the casting procedure to cast products. Green sand is commonly and widely used in casting foundries. Srinivasarao & Kumar (2017) studied the effect of fly ash and molasses addition to the green sand. It was found that the compression strength and permeability of the green sand improved as compared to the green sand without these additives.

3.2 Johnson Cook material model parameters

SiMoCr ductile cast iron is a strong candidate material for automotive, defence and aeronautical applications due to its high tensile strength, fracture toughness and good wear-resistant properties. To realize the various applications of this material, its mechanical behaviour should be thoroughly studied. Material properties are severely affected under various test conditions like large plastic deformation, high strain rates and changes in working temperatures. Also, the prediction of material behaviour at different strain rates and temperatures is essential from the design point of view for various automotive components. A lot of numerical techniques have been developed which become efficient and effective tools for studying material behaviour. The study of the

dynamic behaviour of materials under consideration using numeric techniques are mainly dependent on the selection of the correct material model for a particular material. Johnson & Cook (1983) has presented a constitutive model for materials, subjected to the high strains, strain rate and high temperature, to simulate the behaviour of the material in computations. The aim of accurate prediction of material behaviour remains the same for specific materials by developing a justified flow stress model at various strain rates and temperature. Shrot & Bäker (2012) used the Levenberg-Marquardt search algorithm for the inverse identification of *J-C* material parameters while developing a finite element model for machining processes.Gambirasio & Rizzi (2014, 2016) suggested various procedures for calibration of *J-C* model parameters under high strain rate for elastoplastic materials and a new *J-C* strength model was developed, i.e. split *J-C*, for the prediction of flow stress in three real materials, which improved capability of prediction of material behaviour as compared to the basic *J-C* material model. Banerjee et al., (2015) reached a justified agreement of simulation and experimental results during the behavioural study of armour steel subjected to large strains and strain rates at elevated temperature. Brauer et al., (2017) quantified the complex microstructure of grey cast iron to identify the prominent constituent responsible for the strain rate sensitivity by defining the structure property relationship. During the study on 10%Cr steel at elevated temperature and different strain rates, He et al., (2018) proposed a new modified Johnson-Cook model to consider the hardening mechanism and flow softening parameters in addition to the coupled effect of stress, strain and temperature. Interaction among the parameters responsible for strain hardening of the material was observed and the modified *J-C* model has an edge over the original *J-C* model in prediction of deformational behaviour of the material in hot conditions. For metal forming applications of AISI 1045 Medium carbon steel, Murugesan & Jung (2019) estimated the *J-C* parameters and found that the *J-C*

material model with five parameters explains the combined coupled effect of high strains, high strain rates and temperature. Khare et al., (2021) calculated the *J-C* parameters experimentally from tensile tests at varying strain rates and temperatures. Finite element simulations using such *J-C* material parameters on armour steel specimens with different notch radii under tensile loading were found to be in good agreement with the experimental results.

3.3 Fracture toughness

The mechanical components are assumed to possess several micro cracks or voids within its body, which will remain within the component without any crack growth during normal operation under the action of safe load and the mechanical property of the material is known as fracture toughness. The term fracture toughness became popularized after the pioneering work done by Griffith (1921) hundred years ago, by proposing the concept of material resistance to fracture using energy release rate in assessing the structural integrity of brittle materials. Rice (1968) proposed a new path independent integral 'J-Integral' for approximation of solution analysis of strain concentration by notches and cracks in elastic and elasto-plastic materials. Ast et al., (2019) considered the fracture toughness as coarse graining properties that provides the enough energy dissipation required for crack advancing through the sample. Vaško (2019) compared the fracture toughness of SiMo and SiCu nodular cast iron (NCI) and observed that the SiCu NCI has higher fatigue strength due to the presence of copper. Berdin et al., (2001) investigated the damage mechanism of ductile cast iron by performing tensile and tearing tests on the specimens taken from two different compositions of ductile cast iron and observed that the fracture toughness of the materials depends upon the crack process zone ahead of crack tip. Kujawski (2001) proposed a crack growth modeling for long and

short crack growth based on the fatigue crack driving force alongwith the load ratios. Dinda & Kujawski (2004) summarized the evaluation of fatigue crack growth parameter to predict the crack growth rate for various load ratios. Shirani et al., (2010) predicted the fatigue life of components with structural defects made from SGI using the Gumbel distribution. Also, in the study of fatigue life distribution and size effect in the wind turbine components made from DCI, Shirani & Härkegård (2011) predicted the fatigue strength of components with different dimensions using experimental and statistical analysis. The critical or safe load for structural materials was predicted using the fatigue crack growth mechanism for assessing the effect of load ratios. Ferro et al., (2012) determined experimentally the high cycle fatigue properties of EN-GJS-400 DCI with chunky graphite at constant axial load and room temperature. There was no influence of chunky graphite on the fatigue strength of DCI. The microstructural constituents greatly influenced the crack initiation and propagation but had negligible effect on the cyclic hardening of the nodular cast iron (NCI) (Čanžar et al., 2012) . Szmytka et al., (2020) proposed a method for low cycle fatigue (LCF) lifetime characterization of nodular cast iron. It improved the LCF lifetime results obtained from conventional methods. Matteis et al., (2014) concluded that the strain rate greatly influenced the fatigue strength of the SiMo DCI at high temperatures. Lekakh et al., (2021) proposed a modified mechanically constraint test for thermo-cyclic fatigue strength of SiMo ductile iron. The SiMo ductile iron's resistance to crack formation during thermal cycling is significantly affected by oxidation and decarburization. Benedetti et al., (2019) investigated the influence of alloying element's composition and cooling rate on the graphite morphology, mechanical properties of ferritic DCI and suggested the use of J-Integral instead of conventional critical stress intensity factor tests to quantify the facture toughness. Iacoviello et al., (2019) investigated the behavior of graphite elements during the crack propagation by

analyzing the fatigue crack profiles of the different DCIs and observed that the graphite nodules actually act as crack arrestor instead of a normal rigid nodule embedded in the matrix of the material. Agnihotri (2020) emphasized on the variation in property of material during crack propagation across the crack front in layered structures under dynamic loading conditions. Callister Jr & Rethwisch (2020) investigated that before the 2nd World War, to avoid crack propagation, the then design engineers used to adopt a higher factor of safety while designing the machine components. Toughness is a generalized term used as the energy absorbed by the material before fracture and is calculated as the area covered by the stress-strain curve upto rupture point. K_{IC}, G_{IC}, J_{IC} and CMOD (Crack mouth opening displacement) are the common four types of fracture toughness measures given in available literature. Salehnejad et al., (2019) analyzed the cracking failure of exhaust manifold of engines runs at high temperature by comparing the two given materials for exhaust manifold and found that instead of yield strength, fracture toughness is the criteria for evaluating the material strength of a cracked component. As far as the fracture toughness of available grades of ductile cast iron (DCI) is concern, till now a lot of work has been done to find out the fracture toughness of different available DCIs and accordingly it is used extensively in the different engineering applications. Pusch et al., (2016) obtained the highest static fracture toughness for nodular cast iron having large size graphite nodules in ferritic matrix. Cleavage fracture was seen with higher Si content with high loading rates at low temperatures. Hosdez et al., (2020) compared the fatigue crack growth in Compacted Graphite cast Iron (CGI) and Spheroidal Graphite Iron (SGI) and found that the role of fracture toughness becomes more important when the component surface has minor cracks or voids in the material itself. This type of cracks also influences crack propagation. The curved crack front is noticed in the spheroidal graphite iron which helps in reducing the crack growth rate and

the material has higher fracture toughness as compared to compacted and flakes graphite iron. For modelling the failure behavior and low cycle fatigue resistance of ductile cast iron, Collini & Pirondi (2019) used the microstructure-based reference volume element approach and confirmed the results both numerically and experimentally. The ductile iron was tested at mesoscale and found that nodule count, stress concentration and local triaxiality are the three major factors that affect considerably the behaviour of ductile cast iron. In this study, fracture toughness (K_{IC}) of a newly developed material, named as SiMoCr DCI, was obtained. The composition of SiMoCr iron is intentionally taken different from the composition of available grades of DCIs. Aranzabal et al., (2003) designed a new cast iron consisting of a mixed matrix of proeutectoid ferrite and ausferrite microstructure with high tensile and yield strengths, hardness and ductility similar to pearlitic and ferritic grades of DCI. The material was developed and tested for suspension parts subjected to dynamic loads. Delprete & Sesana (2014) characterized the mechanical properties of a SiMoCr DCI containing a high amount of chromium and investigated the high cycle and low cycle fatigue properties at high temperatures to establish the alloy for high-temperature applications in automotive components. Tokunaga et al., (2019) investigated the effect of Ni content on the microstructure of ferritic DCI and observed that the higher nickel content results in a microstructure with fine acicular ferrite. Borsato et al., (2016) experimentally studied the effect of in-mould composition of inoculants on microstructure and fatigue behaviour of ductile iron using metallographic techniques.

3.4 Sliding Wear

Ductile cast iron has emerged as a potential candidate material for the application in components for automotive, earth movers, special purpose machinery and defence

equipments (Shafiee et al., 2009). This material offers high tensile strength, toughness, thermal stability, high hardness, high wear resistance and good heat dissipation properties to meet the requirement of engineers and researchers for various applications at low production cost (Aal et al., 2006). The application of DCI for manufacturing gears, crankshafts, brake discs, etc., where enhanced wear resistance at different temperatures is needed, has drawn the special attention of the engineers (Abedi et al., 2010). With similar surface roughness values, significant difference was observed in the surface hardness and wear performance of the cast iron (quenched and tempered DCI, ADI and white cast iron) (Henrique et al., 2011). The study of wear behaviour of a DCI is a complex phenomenon due to several variables, including constituents of material, surface properties of the component, temperature range, sliding method: translatory or rotary, sliding velocity: high or low, sliding-type: dry or wet and sliding pressure. Surfaces of the cast components include a variety of defects and distortions, which results in a considerable influence on the material's wear properties. The rise in temperature due to rubbing of the contacting surfaces during sliding also contributes to a higher specific wear rate which may lead to thermal softening and possible melting of the surface layer of the material (Basurto-Hurtado et al., 2016).

Stachowiak & Batchelor, (2013) stated that the behaviour of contacting surfaces during sliding contact is quite different from that of static contact due to the lesser number of contact surface areas in sliding contact compared to static contact. In dry sliding, a few of the surface particles of the contact surfaces may jump out from their lattice structure, under the combined effect of pressure, sliding velocity and temperature, and move along the motion between contact surfaces termed as wear particles. In its study of dry sliding frictional and wear behaviour of two different materials in two different conditions, Bougoffa et al., (2021) concluded that the response of surface wear varies with the type of

wear test, material nature and the conditions in which the wear test was performed. Ramya Sree et al., (2021) observed that the surface treatment with nitride inclusions improves the wear behaviour of the material during dry sliding wear tests. Similar observations were also made by Mamatha Gandhi et al., (2021) during the examination of dry sliding behaviour of AISI 304 stainless steel. Khan & Chhibber, (2020)observed the progressive wear with the change in the pin face profile during dry and wet sliding wear analysis of super duplex stainless steel. Agunsoye et al., (2013) investigated the effect of Si addition to grey cast iron. The wear properties of GCI are studied by varying the sliding speed, load and time. ANOVA and linear regression analysis were used for examining the effect on wear behaviour of GCI. Rooprai et al., (2022) investigated the wear behaviour of AISI alloy steel by performing the pin-on-disc tests and optimized the wear parameters viz. sliding speed, sliding distance and applied load using grey relational analysis and ANOVA techniques based on Taguchi's framework. The results confirmed that being the key parameters sliding speed and the sliding distance significantly affects the specific wear rate and coefficient of friction. Salguero et al., (2018) studied the tribological interferences in the dry machining of Al-Cu alloys using pin-on-disc and proved that the abrasive wear is followed by adhesion. The frictional interaction appeared to be controlled by mechanical interlocking between such wear lumps on opposite surfaces. Cu rich debris were observed over the disc surface during pin-on-disc tests in the Cu enriched interfacial medium of tempered martensitic low alloyed steel pin with annealed tool steel disc (Rodrigues et al., 2016). Less stable higher coefficient of friction values was observed. Lyu (2019) studied the abrasive wear behaviour of compacted graphite cast iron having 0.1% tin (CGI-Sn) using pin-on-disc tests. It was found that tin improves the abrasive wear behaviour of CGI significantly. Mardaras et al., (2020) created an innovative technique to deposit layers of chromium carbide, ledeburite and

pearlite on as-cast specimens of DCI to improve the wear resistance and hardness of the surface layer. Shafiee et al., (2009) studied the microstructural effects on the wear behaviour of DCI and compared the wear properties of Cr-Mo steel with DCI. Cardoso et al., (2014) compared the austempered DCI and white cast iron in terms of abrasive wear resistance and found that the wear resistance of austempered DCI was better as compared to white cast iron due to the presence of martensite in the matrix. Zou et al., (2015) studied the effect of chromium addition to nodular cast iron. It was concluded that chromium addition to nodular cast iron increases the bainite structure in the matrix. Rebasa et al., (2002) carried out an experimental study of the effect of varying nodule count in DCI on abrasive wear and rolling contact fatigue wear. The increase in nodule count resulted in a higher abrasive wear rate. Many researchers have applied statistical techniques to quantify the effects of various parameters influencing sliding wear. Prasad (2006, 2011) studied the cast iron sliding wear response at different wear-affecting parameters like load applied, sliding speed and the surrounding environments to understand the material's wear mechanism. It was noticed that the temperature increases with the increase in speed and load while the frictional coefficient decreases, the wear loss increases significantly. Jozić et al., (2015) applied the Taguchi's design of experiment and grey relational analysis for the optimization of multiple objectives process parameters at the same time. During the optimization of wear performance using response surface methodology, Peng Chang et al., (2015) discovered that the talc being an intermediate material minimizes the surface wear rate. Gupta et al., (2016) optimized the tool wear using response surface methodology and particle swarm optimization. Sahin & Durak (2007) developed a numerical model to study the wear resistance of DCI and observed that sliding distance was the key factor responsible for abrasive wear using the design of experiments and ANOVA techniques.

3.5 Brake disc

With reference to safety, performance and operational life, disc brakes are the crucial part of any automotive unit. The heat evolved during braking, due to frictional rubbing of brake pad over disc surface to control the disc speed, should be addressed properly for long operational life of the brake disc-pad.(Vdovin & Gigan, 2020). Different types of brake disc made from a variety of materials are extensively used in braking applications. Ductile cast iron (DCI), being lighter in weight, good wear resistance and good heat dissipation rate, is a prominent material for brake disc applications ranging from railways brake discs to two wheelers. With the development of new alloys, composites, reinforcements and carbon fiber, the selection of materials for brake discs becomes a very competitive field. During single stop braking event analysis for thermal and structural changes in ventilated disc brake assembly, Belhocine et al., (2016) has studied the effects of various parameters responsible for braking. Polajnar et al., (2017) considered the functionally graded ductile cast iron as the potential candidate material for the brake pads to be used in automotives owing to its good wear properties and consistent coefficient of friction values. As the present study is focused on the development of SiMoCr DCI, the literature review is restricted to only the brake disc surface wear and temperature evolution during intermittent braking application. Li et al., (2020) reviewed the recent scenario of the automotive disc brake and future aspects. The current focus includes thermal conductivity, thermal fatigue resistance, wear rate and the noise intensity during braking.

3.6 Research Gaps and Motivation

On observing the grades of the ductile cast iron given in Table 2.1, it is concluded that the tensile strength and percentage elongation are two properties on the basis of which different grades of DCI are designated. Tensile strength of the grade increases on the cost of elongation or vice versa. There are numerous applications where both tensile strength and elongation are the prerequisite of the material to be chosen such as engine blocks, cylinder head, crankshaft, camshafts, brake discs, exhaust manifold, nuclear cask etc. After extensive literature survey it is found that:

1. The researchers have done a lot of work in the development and characterization of SiMo ductile cast iron which has either higher tensile strength or ductility. But there are hardly any ductile cast materials found till date which serves both the objectives i.e., high yield and tensile strength alongwith good ductility.
2. It is also observed that the presently available ductile cast irons have shown good mechanical properties at room temperature and upto 500℃. Beyond this temperature the behaviour of ductile cast iron changes drastically. In actual working conditions, a lot of components are there which have undergone the high temperature working conditions. For efficient working, these components should possess both good strength and ductility at high temperatures too.
3. During its operational life, a component is subjected to wear due to the rubbing action of relative components and due to which the component may wear out or fail to perform the desired operation. It is desired that the material of components should possess good wear properties, strength and crack arresting properties for avoiding the failure due to fracture propagated from micro cracks on the surface or within the components.

Therefore, it is required to develop a material (SiMoCr ductile cast iron) which should retain its tensile strength with good elongation, fracture toughness and wear resistance

properties even at elevated temperature. Presently very few literatures are available related to SiMoCr ductile cast iron.

3.7 Research Objectives

1. To develop a SiMoCr ductile cast iron for high temperature and wear applications by optimizing the percentage composition of the alloying elements in a designed number of heats using induction furnace.
2. Characterization of microstructure of the SiMoCr ductile cast iron.
3. Characterization of tensile, hardness and wear properties of the SiMoCr DCI.
4. Characterization of fracture toughness of the SiMoCr DCI.
5. Experimental and numerical investigations of an actual component (brake disc) of SiMoCr DCI.

CHAPTER 4

DEVELOPMENT OF SiMoCr DCI

4.1 Introduction

Ductile cast iron is currently used worldwide owing to its cost effectiveness, strength, ductility as compared to the other types of cast irons. The development of SiMoCr DCI includes the selection of alloying elements, calculation of charge material, preparation of patterns and green sand moulds, induction furnace augmentation, melting of charge, magnesium treatment and inoculation and casting. Spectrographic analysis of the developed materials reveals the percentage of alloying elements in the melts. The tensile and hardness test of the developed materials are done to reveal the strength and surface hardness of the materials.

4.2 Selection of alloying elements

Selection of alloying elements, for developing a new DCI, is a very typical work as it requires a thorough knowledge of the available grades of DCI and alloying elements. The knowledge of merits and limitations of available DCI grades is the prerequisite. In addition, the effects of alloying elements on material properties are thoroughly studied and summarized here after.

4.2.1 Carbon (C)

The solidification temperature of iron is reduced to about 1147 °C at 4.3% C, metastable compound (carbide), (1153 °C at 4.2% C, stable compound(graphite)), with the increase of carbon content in iron. Carbon becomes an interstitial impurity in iron and forms the

stable or metastable eutectic solid solution (Callister Jr & Rethwisch, 2020). The fluidity of the iron melt is due to the presence of carbon content, resulting in improved castability. The amount and size of graphite nodules are greatly affected by the carbon content, collectively with inoculation and solidification rate of the melt. Higher nodule count neutralizes the formation of carbides and increases the ferrite formation, and also reduces the hardness and brittleness. The formation of graphite by precipitation of carbon is done during solidification process. The solidification shrinkage of iron compensated by the expansion of precipitated graphite due to its lower density.

4.2.2 Silicon (Si)

Silicon is an important alloying element as it promotes graphite formation and stabilizes ferrite. Enhanced silicon content increases the ferritic area fraction by lowering the primary carbide and pearlitic content of the matrix. For a fully ferritic cast iron, increased silicon content contributes to improved strength by solution hardening of the ferrite. A side effect is, however, reduced ductility. Additions up to 4.0wt% have shown a great increase in the thermal fatigue resistance whereas elevated amounts (>5%) have shown negative effects such as increased brittleness. Silicon is an oxide former and contributes to increased oxidation resistance by the formation of a thin and compact silicon oxide film at the oxide/metal interface. It acts as an inoculant in the production of ductile cast iron.

4.2.3 Molybdenum (Mo)

Molybdenum stabilizes pearlite and is commonly added to cast iron to improve the mechanical properties, such as tensile strength and creep resistance, at high temperatures. However, the amount of molybdenum must be controlled since it has a tendency to form stable carbides in the intercellular regions, which can cause embrittlement. Molybdenum

alongwith nickel in controlled proportion in any material results in higher tensile strength, hardness and toughness.

4.2.4 Magnesium (Mg)

Magnesium as spheroidizing agent is performed an extremely essential activity in ductile cast iron production as it is responsible for precipitation of the graphite as spheroids. Magnesium content (0.03 to 0.06%) is adequate for the formation of sufficient nodules in the melt. Ferrosilicon magnesium (Fe-Si-Mg) is widely used in castings nowadays because of its low cost and applicability to various castings with different sections and C_{eq} values.

4.2.5 Chromium (Cr)

Chromium improves the high-temperature oxidation resistance by the formation of a protective oxide on the alloy surface. It is also a strong carbide former and stabilizer of pearlite. Small amounts of chromium improve tensile strength and hardness, but when excessively added, negative effects, such as increased brittleness may arise.

4.2.6 Copper (Cu)

Copper, being pearlite promoter, has been used since long back in production of cast iron. Copper increases tensile strength and hardness by promoting pearlite formation. Copper has a graphitizing effect and suppresses carbide formation. It has been found that addition of copper to SG iron upto 0.6%, over which only small amount of Ferrite could be obtained with low cooling rates (Sertucha et al., 2010)

After rigorous study, Carbon, Silicon, Molybdenum, Chromium and Copper are selected as alloying elements for the present study.

4.3 Casting pre-requisite

Casting pre-requisite includes the pattern making of the specimens to be produced and mould preparation.

4.3.1 Making of patterns

The patterns are made from wood material. The requisite shape of patterns viz. round, rectangular, circular disc and the brake disc patterns are made as shown in Fig. 4.1. The size of patterns is kept a little bigger than the casting product to accommodate the standard draft allowances, shrinkage allowances, machining allowances, deformation or camber allowances, shake or rapping allowances etc.

4.3.2 Mould preparation

The standard procedure of preparing moulds is followed using cope-drag type mould boxes in preparation of moulds. Gating, runner and risers are made as shown in Fig. 4.1. The prepared moulds are left on shop floor for Seven days so that the mould cavity got dried on its own.

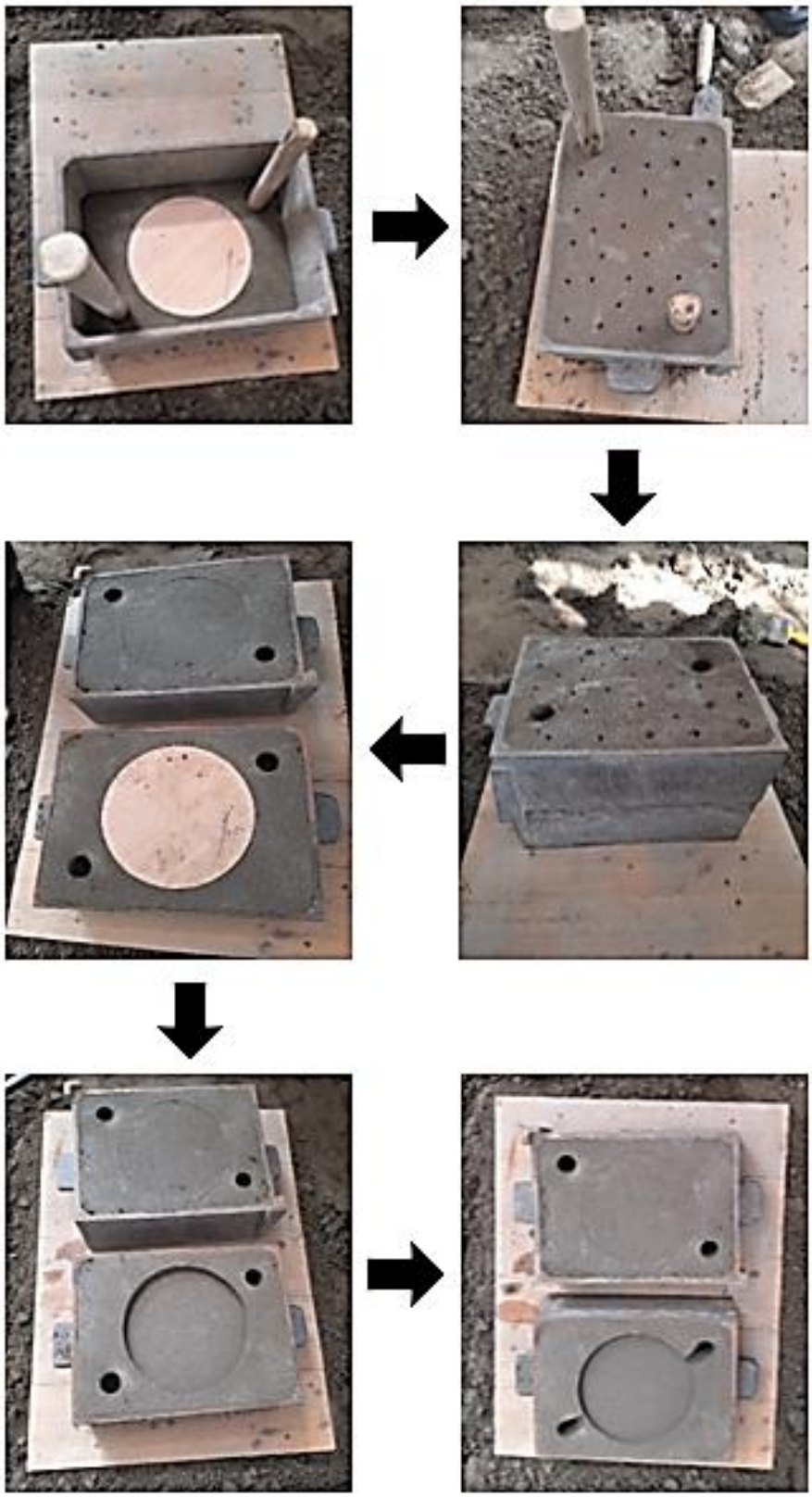

.

Fig. 4.1 Process flow chart of mould preparation for test samples

4.3.3 Charge material

The proposed composition of the alloy is given in Table 4.1. A minimum of three heats of material is to be produced using an induction furnace. Hence, the details of the various ingredients to be used in preparing the melt is given onward.

Table 4.1 Desired composition of SiMoCr DCI

Melt	Alloying elements(%wt.)						
	C	Si	Mo	Cr	Cu	Mg	Fe
Melt-1	3.1	3.0	0.8	0.3	0.3	0.06	rest
Melt-2	3.3	3.4	0.9	0.4	0.4	0.07	rest
Melt-3	3.5	3.8	1	0.5	0.5	0.08	rest

4.3.3.1 PIG Iron

It is an intermediate product of iron produced by the smelting of iron ore and cast in the form of pig moulds. It is brittle in nature and commonly used in making cast iron, wrought iron and steel. Its melting temperature ranges between 1150- 1200°C. It comprises of 1.8-4 % wt. carbon and 1-3% wt. silicon. Pig iron is a consistent charge material for ferrous casting production.

4.3.3.2 Ferrosilicon (Fe-Si)

Ferrosilicon is a mixture of iron and silicon with silicon ranging from15% to 90% wt. It melts at about 1200- 1250℃. It also contains about 1% to 2% wt. of calcium and aluminium. It is used as an inoculant of iron to accelerate graphitization. It is a base material for prealloys like magnesium ferrosilicon used as nodulizer in the production of DCI. The chemical composition of the Fe-Si selected for this study has 70% wt. silicon content.

4.3.3.3 Ferromolybdenum (Fe-Mo)

Ferromolybdenum is a ferro alloy containing 60-75% wt. molybdenum. It acts as a hardening agent and is found in alloys that are heat treatable. It increases the resistance to corrosion, improves weldability, wear resistance and strength. The melting point ranges from 1665-1715°C. The Fe-Mo selected in this study contains 60% wt. molybdenum.

Ferrochromium is available in two grades namely high carbon ferrochrome and low carbon ferrochrome. High carbon ferro chrome contains Cr 68%, C 8%, Si 3%, Cu 0.5% while low carbon ferro chrome contains Cr 65%, C up to 1%, Si 1%. The melting point of low carbon Fe-Cr, selected for present study, is about 1545°C and contains 65% wt. chromium.

4.3.3.4 Copper

Copper is a soft, malleable and ductile metal with very high thermal and electrical conductivity. Its melting point is about 1085℃. The pure copper bars used in this study contain 100% copper content.

4.3.3.5 Ferrosilicon-magnesium (Fe-Si-Mg)

Fe-Si-Mg being a main alloy of magnesium with silicon and iron, converts the graphite flakes into nodules. The melting point of Fe-Si-Mg is approximately 1250℃.

4.3.4 Charge material-calculations

The holding capacity of induction furnace used for this study is only 10 kg charge material. Therefore, the charge material is calculated accordingly for the three melts separately. The requisite composition of the three melts is given in Table 4.1. The chemical composition of charge material to be melted in induction furnace is tabulated in Table 4.2.

Table 4.2 Chemical composition of charge material

Charge material	Element (%wt.)									
	C	Si	Mn	P	S	Ni	Cu	Mo	Cr	Fe
Pig iron	4.23	2.31	0.24	0.11	0.02	0.02	-	-	-	Rest
Fe-Si	0.05	70	-	0.02	0.03	-	-	-	-	Rest
Fe-Mo	0.2	0.11	-	0.05	0.01	-	0.05	60	-	Rest
Fe-Cr	1.12	0.16	-	0.03	0	-	0.06	-	65	Rest

The calculation of charge material for Melt-1 casting is given below. Similar calculation was done for Melt-2 and Melt-3 and tabulated in Table 4.3.

Melt-1

1. Charge quantity of pig iron- 10 kg

Pig iron contains 4.23% carbon, 2.31% silicon and 0.24% manganese.

Therefore, 10 kg pig iron contains

C = $\frac{4.23\times10}{100}$ = 0.423 Kg

Si = $\frac{2.31\times10}{100}$ = 0.231 Kg

Mn = $\frac{0.24\times10}{100}$ = 0.024 Kg

Desired quantity of Si = $\left(\frac{3.0}{100}\times10\right) + 10\%\ foundary\ losses$

= 0.33 Kg

Fe-Si contains 70 % Si,

2. Charge Quantity of Fe-Si

= Si obtained from Fe-Si- Si obtained from pig iron

= $\frac{100\times0.33}{70} - 0.231 =$ 0.24 kg

Desired quantity of Mo

= $\left(\frac{0.8}{100}\times10\right) + 10\%\ foundary\ losses$

= 0.088Kg ~ 0.09 Kg

Fe-Mo contains 60 % Mo,

3. Charge quantity of Fe-Mo = $\frac{100\times0.09}{60}$ = 0.15 kg

Desired quantity of Cr

$$= \left(\frac{0.3}{100} \times 10\right) + 10\%\ foundary\ losses$$

= 0.033 Kg ~ 0.035 Kg

Fe- Cr contains 65% Cr,

4. Charge quantity of Fe-Cr = $\frac{100\times0.035}{65}$ = 0.054 kg

Desired quantity of Cu

$$= \left(\frac{0.3}{100} \times 10\right) + 60\%\ foundary\ losses$$

= 0.053 Kg ~ 0.055 Kg

Cu bars are 100% pure,

5. Charge quantity of Cu = 0.35 Kg

Table 4.3 Charge material composition

Melt	Charge material (kg)				
	Fe-Si	Fe-Mo	Fe-Cr	Cu	Pig iron
Melt-1	0.24	0.15	0.054	0.055	10
Melt-2	0.31	0.17	0.07	0.064	10
Melt-3	0.37	0.184	0.085	0.08	10

4.3.5 Induction furnace preparation

Fig. 4.2 shows the 10 kg and 30 KW capacity induction furnace used for casting. Before casting the initial procedure of furnace inspection is done as per manual provided with the

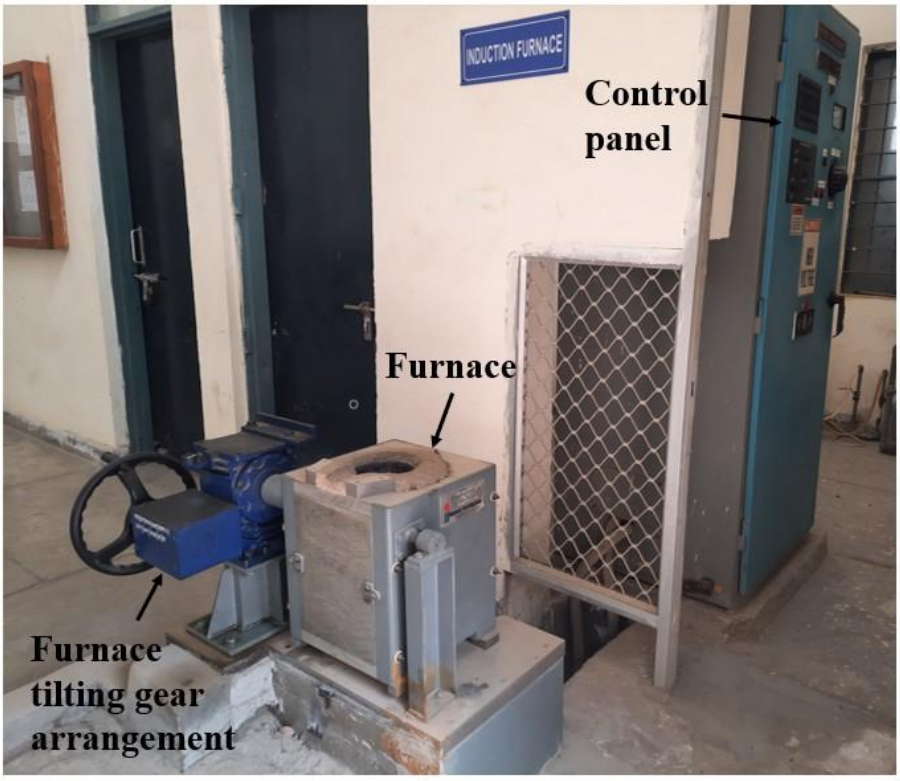

Fig. 4.2 Preparation and setup of induction furnace

furnace. For the proper functioning of different parts of the furnace, continuous cooling of the furnace parts during the melting is a must to avoid overheating. Cooling tower, tank water purifier and cooling channels are checked first for any kind of damage/leakage. The furnace crucible is also checked for any crack or foreign deposition.

4.3.6 Preparation of inoculation and magnesium treatment ladle

For inoculation and magnesium treatment sandwich method is used. A separate ladle is chosen for the said treatment. At the bottom of that ladle a pit is prepared using moulding sand as shown in Fig. 4.3 and left it to get dried for removing moisture content. A cover plate of thin mild steel sheet for covering the pit is prepared in sheet metal shop using different hand tools. On the day of casting the ferro-silicon-magnesium granules covered with ferrosilicon layer are placed beneath the cover plate.

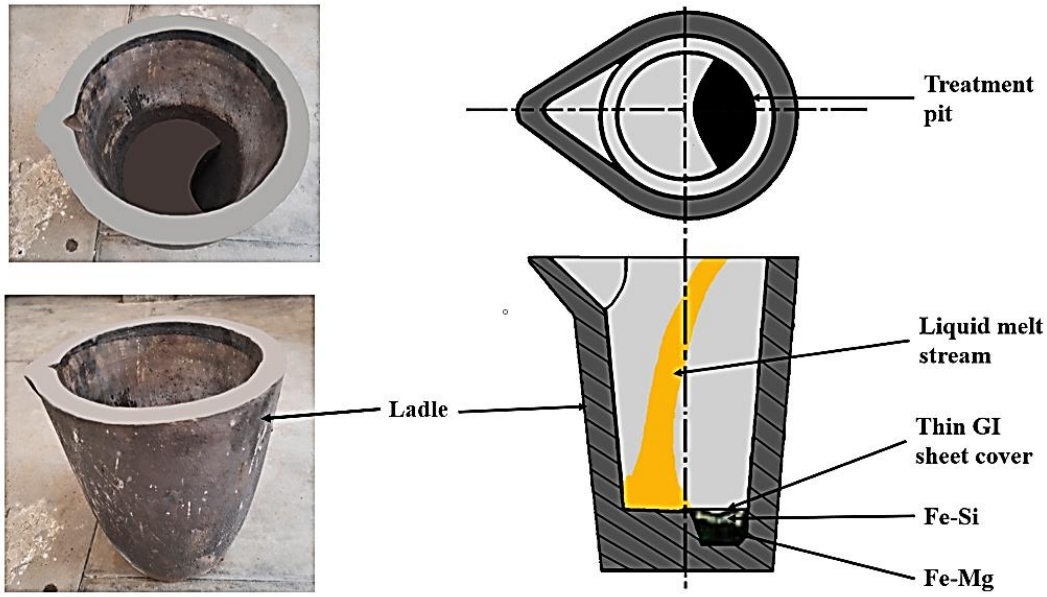

Fig. 4.3 Preparation of treatment ladle

4.3.7 Calculation of the Fe-Si-Mg quantity for magnesium treatment

Magnesium treatment is an important step for the formation of good quality nodules in DCI castings. The quantity of Fe-Si-Mg alloy to be used in magnesium treatment ladle is calculated using the general formula (Cabanne, 2011) given in Eq. 4.1.

$$W_{\text{Fe-Si-Mg}} = W_{ladle} \times \frac{(Mg_f + 0.76(S_i - S_f) + 10^{-3}t}{\%Mg_{Fe-Si-Mg} \times R} \times \left(\frac{T°C}{1450}\right)^2 \quad \text{Eq. 4.1}$$

where,

$W_{\text{Fe-Si-Mg}}$ = Weight of Fe-Si-Mg (Kg)

W_{ladle} = Weight of melt in ladle (Kg)

Mg_f = %wt. in melt after treatment

$\%Mg_{\text{Fe-Si-Mg}}$ = % wt. of Mg in Fe-Si-Mg alloy

S_i = % wt. of initial sulphur content in melt

S_f = % wt. of final sulphur content in melt after magnesium treatment

t = Time taken in magnesium treatment(minutes)

T = Temperature of melt (°C)

R = Yield of mg during magnesium treatment

The quantity of Fe-Si-Mg required for magnesium treatment using Eq. 4.1 for Melt-1

$$W_{\text{Fe-Si-Mg}} = 10 \times \frac{(0.06+0.76(0.064-0.005)+10^{-3}(0.5)}{6\times 50} \times \left(\frac{1470}{1450}\right)^2$$

$$= 0.3 \text{ Kg}$$

Similar calculations are done for Melt-2 and Melt-3 and the quantity found as given in Table 4.4.

Table 4.4 Fe-Si-Mg quantity required for Mg treatment

Melt	Fe-Si-Mg alloy (Kg)
Melt-1	0.30
Melt-2	0.33
Melt-3	0.36

4.4 Melting and casting

The standard operating procedure for augmentation of induction furnace is followed. Initially, the cooling water supply started first and after that the furnace is switched ON with a minimum load for 30 minutes. The furnace is again inspected for any uneven instance of leakage, cracks etc. Firstly, the crucible is filled with the charge material (pig iron and ferrosilicon) in granules form, after that gradually heating the charge material is done by increasing the load in the step of 2.5 ampere per 10-minute step upto a load of 25 ampere. The pig iron contains impurities resulting in the slag formation over the melt surface. Also, the sulphur content present in the melt must be removed or reduced as it is prone to react with the elemental magnesium (added to the melt for magnesium treatment) and form the magnesium sulphide Mg_2S. To avoid such formation calcium powder is added to the melt in small quantity. The calcium powder reacts with sulphur available in the melt and forms calcium sulphide and rises upward in the form of slag

over melt surface. The formed slag is removed time to time. Fig. 4.4(b) shows the process of slag removal. Fe-Mo and Fe-Cr granules are added to the furnace at about 1200° C. A thermal imaging camera is used for recording the furnace temperature rise. When the furnace temperature reached about 1470° C, based on the literature of casting, it is assumed that the whole molten metal in the crucible got homogenized at this temperature and the melt is ready for pouring in treatment ladle. In Fig. 4.4(a) the red-hot crucible is shown in which melting of the alloy starts at around 1200° C. The treatment ladle was placed below the crucible mouth in such a way that when the furnace tilted with the help of gear arrangement, the melt easily poured into the ladle as shown in Fig. 4.4(c). The inoculation and magnesium treatment process are presented in Fig. 4.4(d). The pouring of liquid metal into the treatment ladle is done in such a way that it first strikes the far side of base of the treatment ladle as shown schematically in Fig. 4.3 and then spills over to the cover plate of the treatment pit, melt it and react with the Fe-Si and Fe-Si-Mg granules for the formation of good quality nodules of DCI by inoculation and magnesium treatment of the melt. The Fe-Si provides enough nuclei for the formation of dendritic structure of the melt while the Mg content converts the flakes of graphite into nodules. At the time of pouring the temperature of the melt (approx.1450°C) is more than the boiling point of the Mg (1090°C). The molten metal covers the whole space above the magnesium granules which boil and convert into high pressure magnesium particles. These high-pressure magnesium particles react with the graphite flakes throughout the melt and convert them into nodules. The treated ladle is then transferred from heating area to mould pouring area and pouring of melt into moulds cavities is done as shown in pictorial flow diagram in Fig. 4.4(e). Cu chips are added to the liquid melt in the treatment ladle just before pouring the melt into moulds. The filled moulds are allowed to

cool naturally upto room temperature. A similar method of casting is adopted for Melt-2 and Melt-3 with the charge material calculated as per Table 4.2.

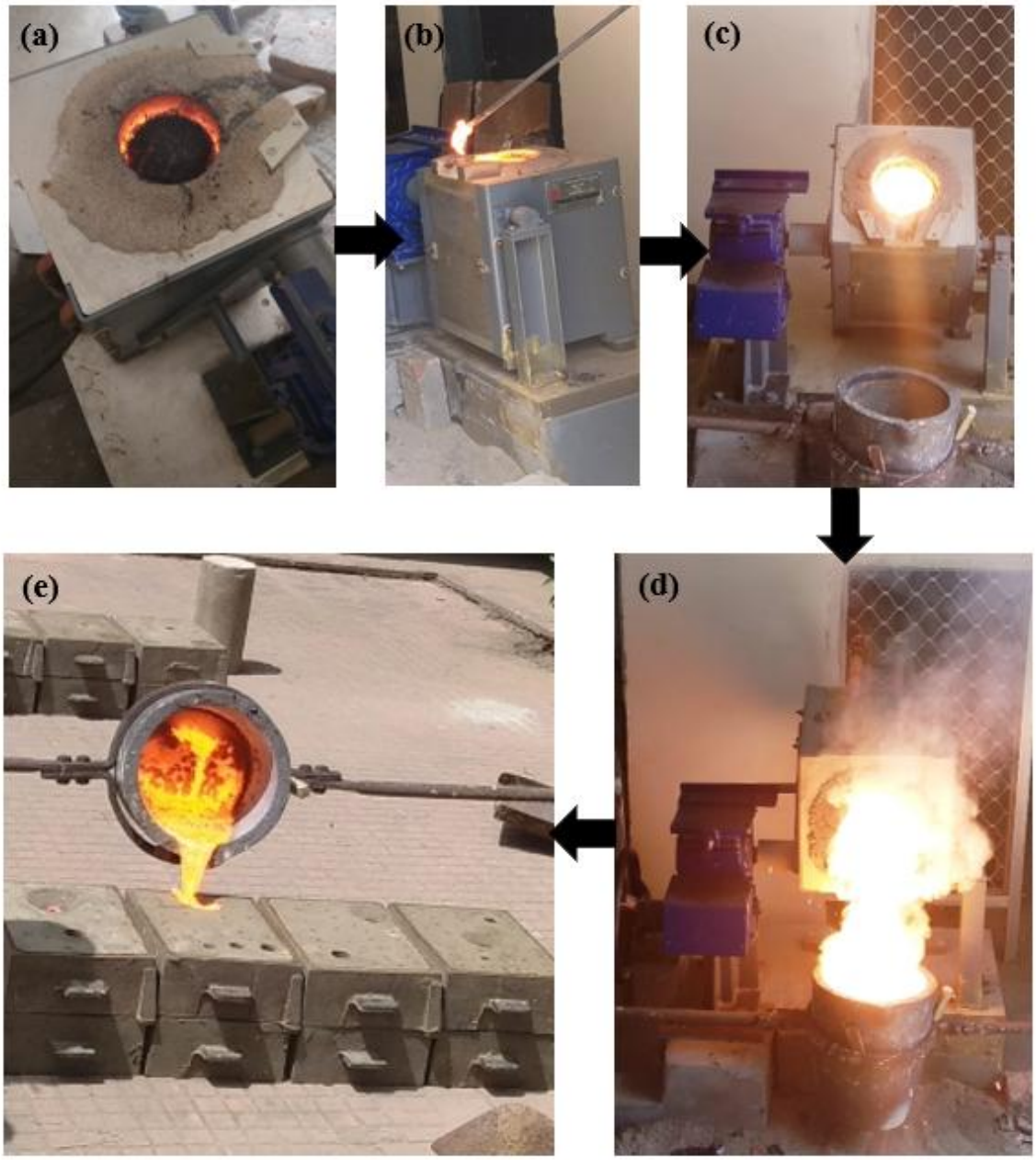

(a) Heat initiation, (b) Slag Removal, (c) Melt ready for pouring, (d) Inoculation and magnesium treatment, (e) Pouring into the moulds

Fig. 4.4 Pictorial flow diagram of SiMoCr DCI casting process

The liquidus to solidus temperature of the melt is recorded using the non-contact type infrared thermometer (±1.5°C) and the variation in melt temperature is presented in the form of cooling curve for the three melts is shown in Fig. 4.5.

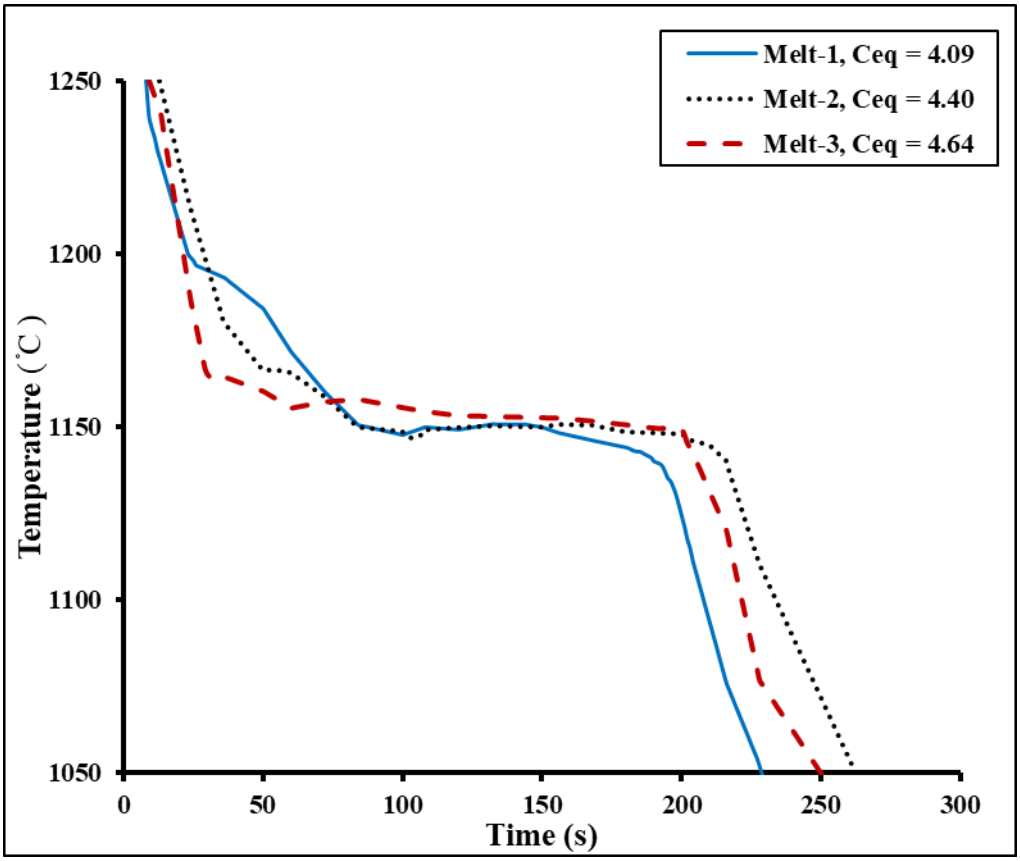

Fig. 4.5 Comparison of cooling plots

It is observed from the cooling curves of the three melts that all the three melts change their phase from liquidus to solidus between 1147°C to 1160°C. Melt-3 cools very rapidly as compared to the rest two from 1250°C to 1170°C, which may be due to the presence of more percentage of carbide former alloyants. A very small effect of undercooling is also observed there in the three melts at varying time span as seen in Fig. 4.5, which confirms that sufficient amount of inoculants is added to the melts. It is observed that all the three melts experience the cooling lag before the phase transition starts, but Melt-1 experiences the more cooling lag as compared to the rest which might be happened due to the presence of austenitic structure in Melt-1 in addition to ledeburite and carbide structure. It is also observed from Fig. 2.1, that Melt-1 is a hypoeutectic ductile cast iron due to its carbon equivalent as 4.09. Melt-2 and Melt-3 belongs to hypereutectic ductile cast iron due to their carbon equivalent values 4.4 and 4.64, respectively. After transforming into

solidus state Melt-2 takes more time to cool while Melt-1 cools comparatively faster. This may be due to the presence of Cu elements in the melts. Melt-2 has lesser amount of Cu elements as compared to Melt-1 and Melt-3. During solidification, carbides may form late in the intercellular regions where the last liquid melt solidifies at lower temperature with higher percentage of carbide former elements. It may be concluded that based on the percentage of alloyants, the microstructure of the Melt-1 will have ferritic dominant matrix due to lesser carbide formation while Melt-3 will have more carbide formation and may be considered as pearlitic dominant matrix.

4.4.1 Evaluation of chemical composition of the developed melts

After casting the components, the specimens, cut carefully from the cast components, are cleaned by removing the dirt etc. The samples of size 10mm are cut from the components to verify the composition of alloying elements in each melt. Three samples from each melt were taken cautiously. These samples are cleaned with acetone solution for the removal of any foreign material on the specimen surfaces. The surfaces of the specimens are prepared by removing any surface irregularity using hand file and emery papers of different grades. These prepared samples are tested on a spectrometer and the typical composition of alloying elements retained in the three melts alongwith the carbon equivalent is given in Table 4.5.

Table 4.5 Chemical compositions of developed DCI

Melt	Major alloying elements (% wt.)								C_{eq}	Density kg/m^3
	C	Si	Mo	Cr	Cu	Mg	P	Fe		
Melt-1	3.2	2.67	0.51	0.23	0.43	0.04	0.02	rest	4.09	7509
Melt-2	3.42	2.96	0.64	0.32	0.38	0.05	0.02	rest	4.40	7518
Melt-3	3.55	3.27	0.77	0.47	0.45	0.06	0.02	rest	4.64	7530

The same samples are weighed for calculating the density of the melts and the average density of the melts is given in Table 4.5.

4.4.2 Microstructural analysis

4.4.2.1 Specimen preparation

The specimens for metallographic evaluation on metallurgical optical microscope are taken from the cast cylindrical and rectangular test bars from each melt. The specimen preparation includes:

1. Sectioning and cutting of the specimen,
2. Mounting of the specimen,
3. Surface finishing operations viz. grinding, polishing,
4. Etching.

The sectioning and cutting of specimen are done using abrasive cutter. The specimens are too small to handle during the surface finishing operations and metallographic analysis. Therefore, the specimens are mounted with a thermosetting resin using a compression-type semi-automatic mounting press for easy handling during microstructural analysis. The mounted specimens are polished in dry and wet conditions using a standard test procedure to achieve a mirror-like finish. To reveal the microstructure, a Nital solution

containing 3% nitric acid in alcohol is used to etch the specimens. After etching the specimens are washed in running water to avoid the specimen surface burning effect of the etchants and wipe off the water droplets from the surface of the specimens using tissue paper. All the specimens are prepared in a similar way for microstructural analysis.

4.4.2.2 Microstructural analysis using optical microscope

A DCI, mainly alloyed with Si, Mo, and Cr is prepared in three different melts to observe the effects of variation of major alloying elements on the microstructure and mechanical properties of the alloy. The chemical composition of carbon is in the range of 3.2 to 3.55% by wt. in the experimental melts. Increase in the carbon content increases castability by improving fluidity and feeding but the carbon content level is usually correlated with the carbon equivalent (C_{eq}). The value of the carbon equivalent is determined by using Eq. 2.1. In the present study, the value of carbon equivalent varies from 4.09% to 4.64% as given in Table 4.5. Due to the presence of higher silicon in combination with molybdenum and chromium, the melts have a very narrow window for the castings to be defect free. A section size of Ø20mm of the casting test bars is observed to be influencing both volume fraction and size of the graphite nodules. Graphite floatation is observed to be more pronounced in Melt-3 which could be attributed to a higher value of carbon equivalent. This further may have resulted in depletion of larger nodules in the middle part of the castings as given in Table 4.6.

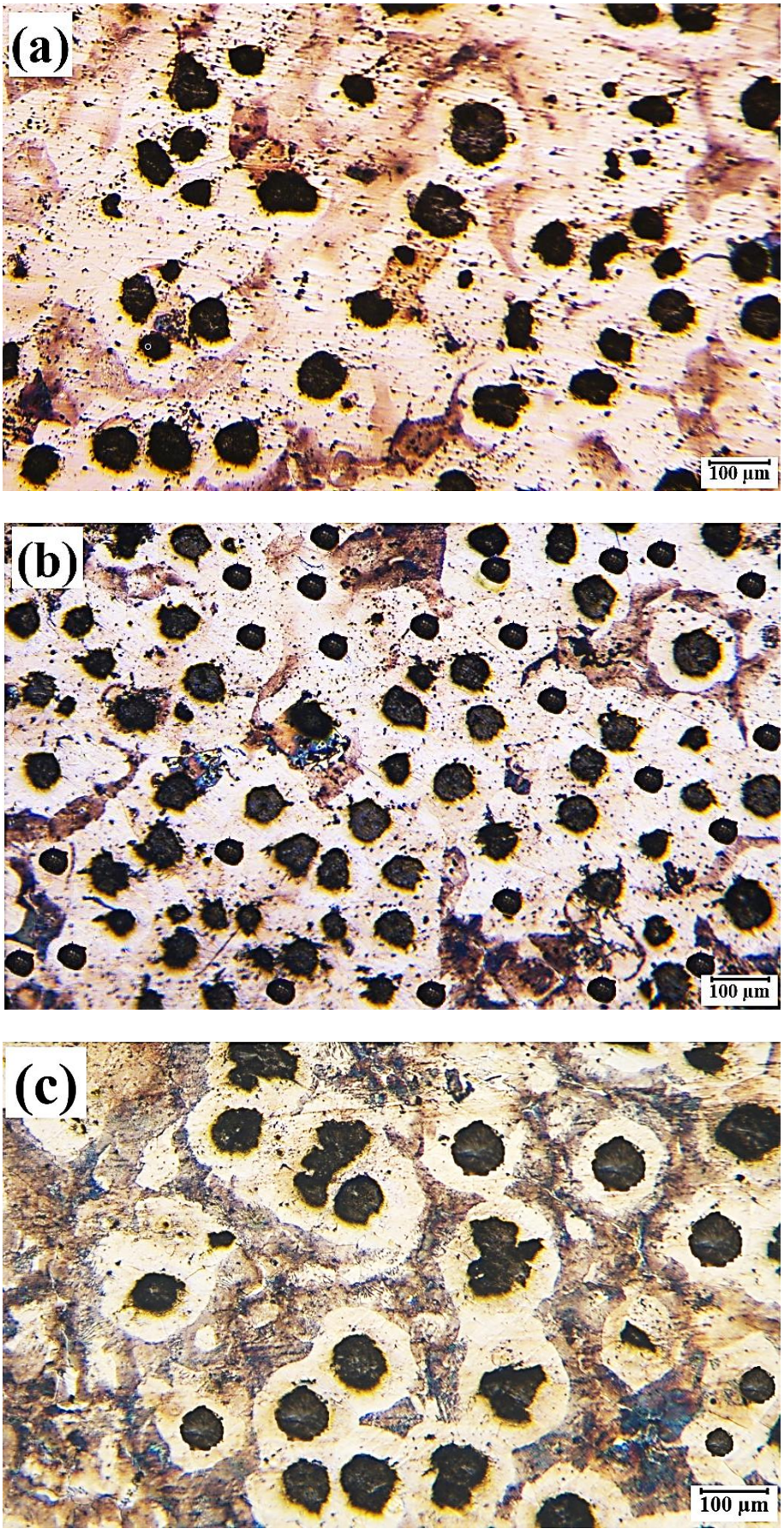

Fig. 4.6 Nodularity matrix in Melt-1(a), Melt-2(b), and Melt-3(c) specimens

The composition of major alloying elements Si, Mo, and Cr is observed to be higher in Melt-3. Representative micrographs of the specimens taken from each melt at a magnification of 100X are shown in Fig. 4.6.

Table 4.6 Microstructural details of SiMoCr DCI

Melt	Microstructural details				
	Nodularity range (%)	Equivalent nodule diameter (μm)	Nodule count (per mm^2)	Ferrite (%)	Pearlite (%)
Melt-1	72 to 80	62	210	57	43
Melt-2	80 to 90	53	223	60	40
Melt-3	68 to 79	73	117	46	54

It is observed that the micrograph of Melt-2 depicts the highest percentage nodularity which varies from 80% to 90% followed by Melt-1 with a nodularity of 72% to 80%. The least percentage of nodularity is observed in the Melt-3 although having the biggest equivalent size of the nodule. The highest number of nodule counts is found in the specimens of Melt-2 and minimum with Melt-3. The variations in islands of ferrite enveloping the graphite nodules and dispersed pearlite are also observed from the micrographs in all the melts. The highest amount of ferrite is observed in Melt-2 followed by Melt-1. Some irregular ferrites, pearlite with chunky graphite, is observed in Melt-3. The microstructural examination reveals the variation in the number of graphite nodules varying from 117 to 223. The highest number of nodules i.e., 223 are observed in the specimens of Melt-2 followed 210 nodules in the specimens of Melt-1 which may be attributed to the respective carbon equivalent. However, specimens of Melt-3 possess the highest value of C_{eq} (4.64%) but the lowest nodule count in the pearlitic structure. The lowest nodule count in the specimens of Melt-3 may be attributed to the graphite floatation during solidification and the combined effects of other alloying elements viz.

silicon, molybdenum and chromium in higher quantities when compared to that of Melt-1 and Melt-2.

4.5 Mechanical Testing

In the present study, mechanical testing includes tests for hardness, tensile strength, fracture toughness evaluation of the three melts of SiMoCr DCI. The hardness and tensile strength of the three melts are studied in the following subsections while fracture toughness of the three melts is studied in Chapter 6. The test bars for uniaxial tensile tests and bend specimens are machined from the central part of the castings to evaluate the various strengths of the three melts.

4.5.1 Hardness evaluation

For evaluating the variation in hardness of the three melts, a microhardness tester, Struers Make (Model: DURAMIN40), shown in Fig. 4.7, is used to evaluate the variation in hardness of the specimens prepared from Melt-1, Melt-2, and Melt-3. A series of equidistant micro-indents are made over the specimen's surface, made from the three melts comprises of graphite nodules in the ferritic-pearlitic region as observed in Fig. 4.6 and Table 4.6, in a straight line which includes the graphite nodules in regions of ferrite and pearlite (Fig. 4.8) and the average variation in the microhardness is plotted for all the specimens of Melt-1, Melt-2 and Melt-3 respectively in Fig. 4.9.

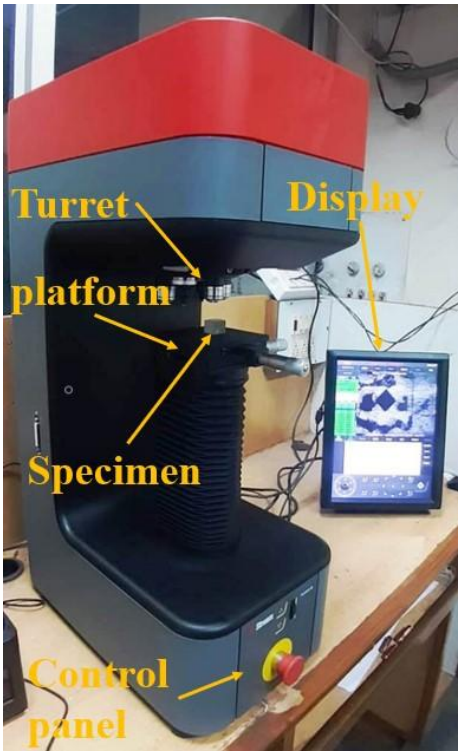

Fig. 4.7 Microhardness Testing setup

(Struers Make: DURAMIN40)

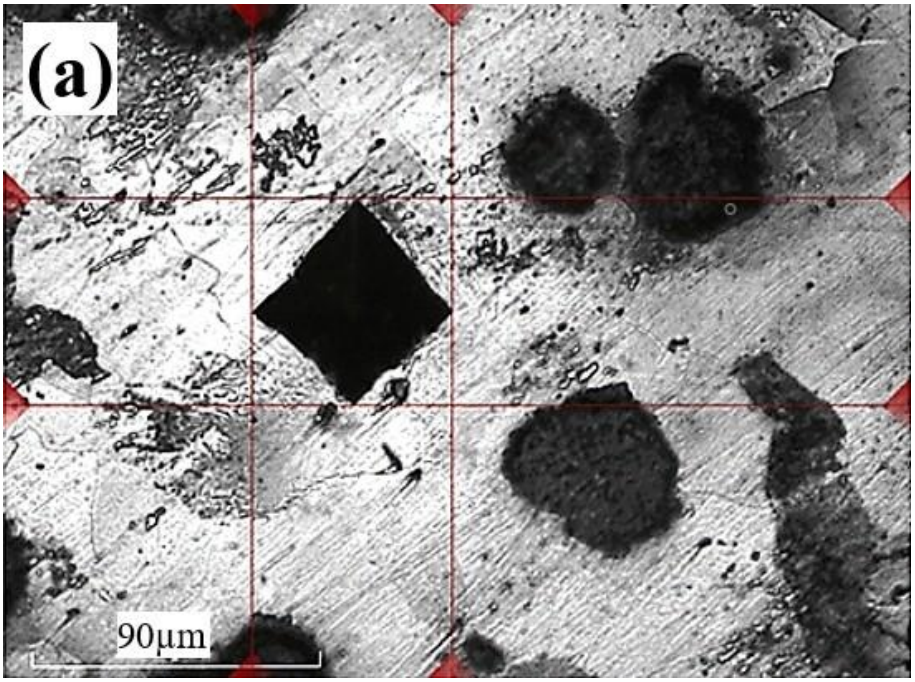

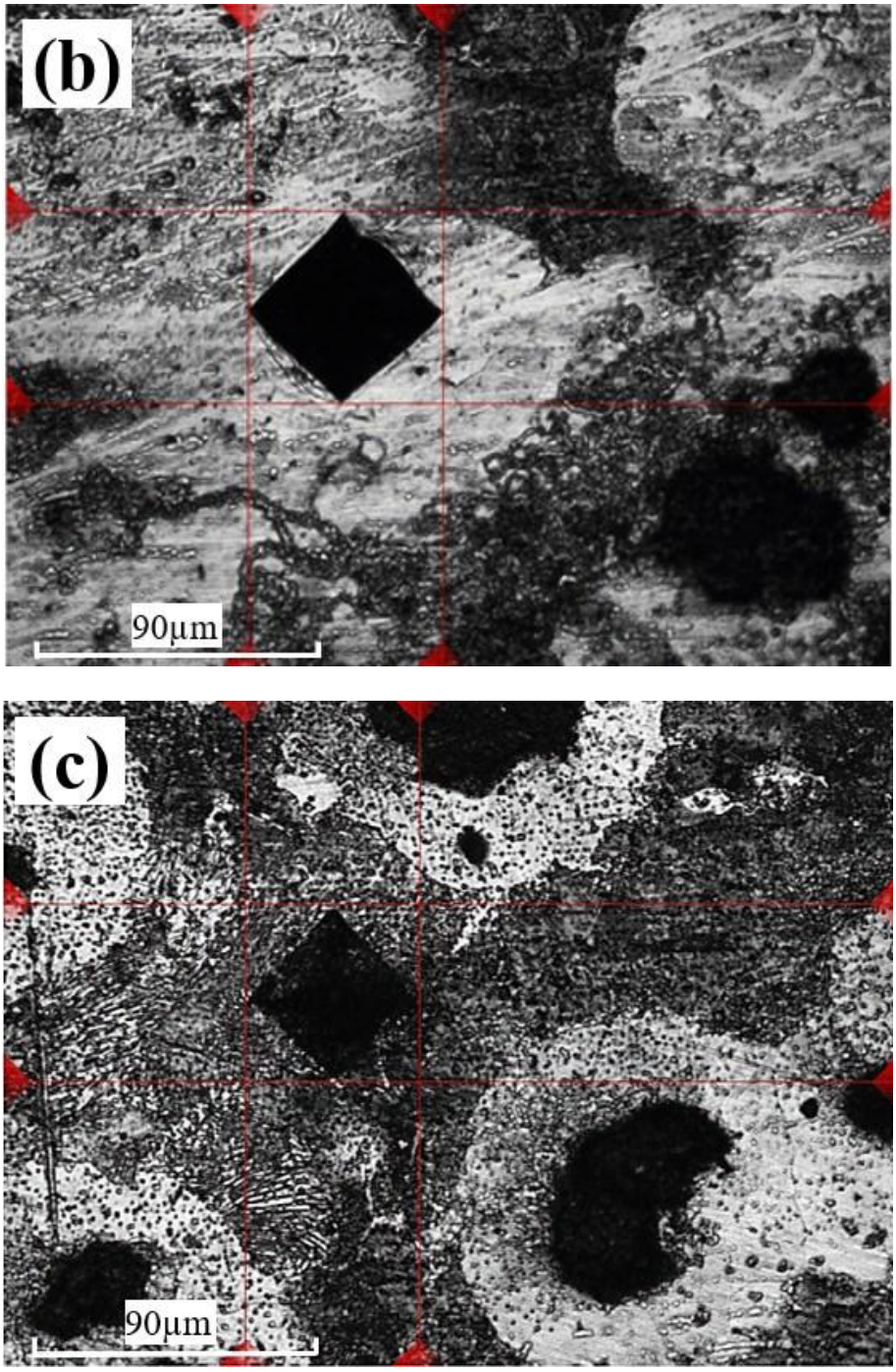

Fig. 4.8 Vickers microhardness indentations on the matrix of ferrite and pearlite in different specimens

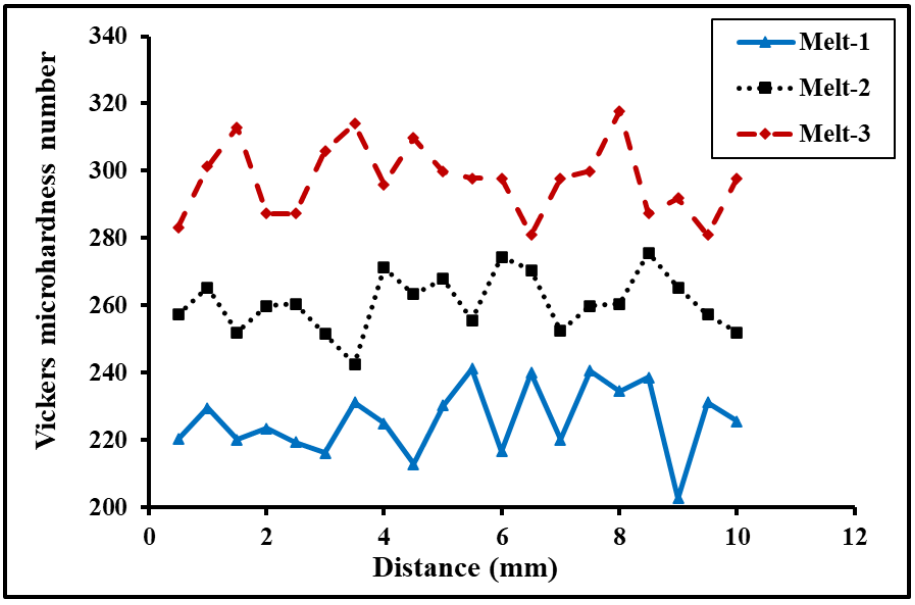

Fig. 4.9 Variation of microhardness observed in samples of Melt-1, Melt-2 and Melt-3

From Fig. 4.9 and Table 4.7, it is observed that the hardness pattern with increasing and decreasing peaks and valleys is found in all the tested specimens. The peaks represent the pearlitic region while valleys represent the ferritic region on the tested regions. The average hardness value of the specimens of Melt-3 is the highest i.e., 298 ± 10.67 HV0.5 followed by hardness in samples of Melt-2 and Melt-1. This higher hardness may be attributed to the higher amount of pearlitic regions in the specimens. The average hardness value in the sample of Melt-2 is observed to be 261 ± 8.60 HV0.5 whereas the hardness in Melt-1is observed to be the lowest i.e. 226 ± 10.29 HV0.5.

4.5.2 Tensile properties

Tensile properties of the as-cast specimens of three melts are found by testing of the prepared specimens on universal testing machine (Tenius Olsen) under tensile loading.

4.5.2.1 Specimen preparation for tensile test

The tensile test specimens, as per ASTM A370-11, are machined from as-cast test bars by the turning operation on lathe machine followed by surface finishing operations on the gauge length area using different grade emery papers. The gripping portion of the test

specimens is kept rough to avoid any slippage during tensile loading of the specimen. The gauge length is marked as per the standard. The detailed drawing and the prepared tensile test specimens are shown in Fig. 4.10.

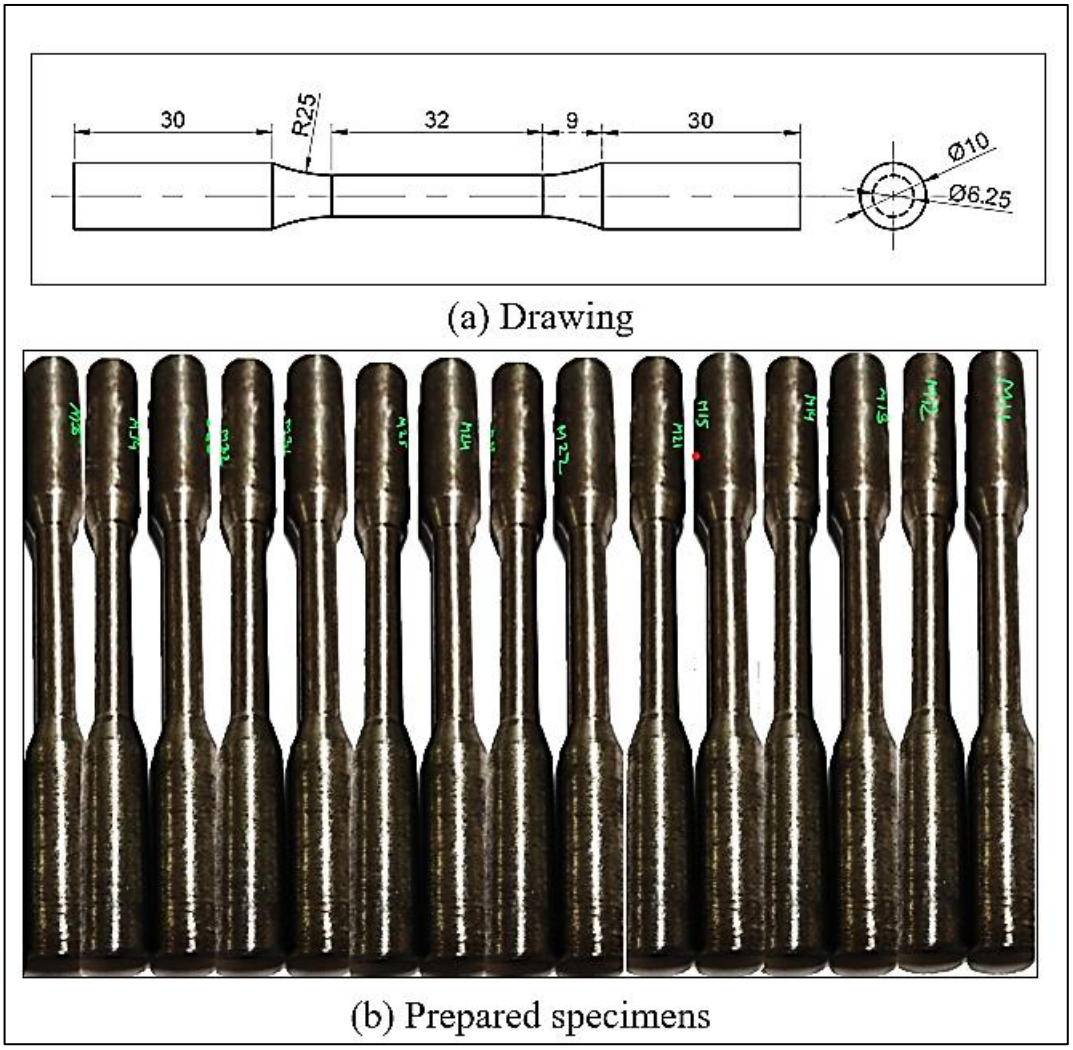

Fig. 4.10 Tensile test specimens (all dimensions in mm)

Fig. 4.11 Tensile test setup on universal testing machine (Tenius Olsen)

4.5.2.2 Tensile strength evaluation

The prepared specimens are tested on the universal testing machine shown in Fig. 4.11. To determine the tensile properties, the samples are clamped in the jaws on a universal testing machine (Tenius Olsen) and Measurement of sample gauge length, gauge diameter is recorded with the help of vernier caliper and entered into machine system as initial gauge length and gauge diameter. When tensile load is applied on the specimen, the gage length starts elongating and resulting in a cup- cone fracture. The specimen breaks at the ultimate tensile strength value and the process automatically stops. The variation in tensile load and in gauge length of the specimen are continuously recorded. The broken specimen is taken out and final gauge diameter at broken edge and final gauge length are recorded A total number of five tensile samples from each melt were tested to capture the scatter in the results. A representative broken specimen is presented in Fig. 4.12. The average engineering stress–strain relation for the three melts is shown graphically in Fig. 4.13 and the average values of ultimate tensile strength and percentage elongation observed in three melts are tabulated in Table 4.7.

From Fig. 4.13 and Table 4.7 it is observed that the lowest tensile strength is seen in the specimens of Melt-1. This can be attributed to the higher microshrinkage porosity,

amount of carbon and other major alloying elements with existing nodule geometry. The percentage elongation in Melt-3 is observed to be 12.01%.The highest values of UTS (606MPa) and

Fig. 4.12 Fracture surface of tensile tested specimen

percentage elongation (13.98%) are observed in Melt-2 due to the presence evenly dispersed graphite nodules smaller in size and of spherical shape. The higher number of nodules with higher nodularity acts as crack arrester during plastic deformation of the tensile samples.

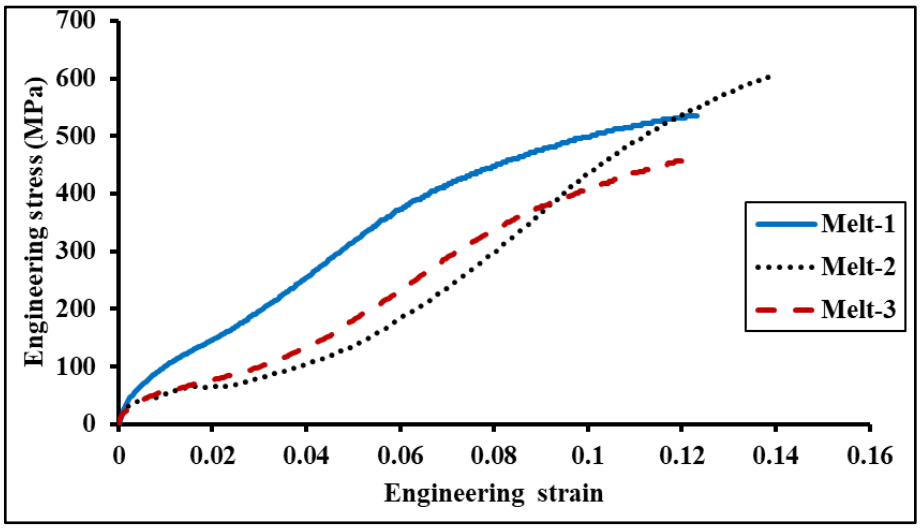

Fig. 4.13 Engineering stress-strain plots

Table 4.7 Comparison in mechanical properties of the three melts

Melt	UTS, MPa	% elongation	Vickers hardness
Melt-1	535	12.3	226 ± 10.29 HV0.5
Melt-2	606	14.0	261 ± 8.60 HV0.5
Melt-3	455	12.01	298 ± 10.67 HV0.5

The higher percentage of graphite nodules in the samples of Melt-2 also plays an important role for its higher strength as compared to the samples of the other two melts.

The comparison of mechanical properties (ultimate tensile strength, percentage elongation and hardness) with other equivalent grades is given in Table 4.8. It is found that the SiMoCr DCI has a higher ultimate tensile strength and hardness than the equivelent DCI grades. The percentage elongation is also observed higher than the two equivalent grades (EN-GJS-500-10 and EN-GJS-600-3) and lower than EN-GJS-400-18.

Table 4.8 Comparison of mechanical properties with equivalent DCI grades

Material	Mechanical Properties		
	UTS (MPa)	% Elongation	Hardness
EN-GJS-400-18	400	18	140-170HV
EN-GJS-500-10	500	7	150-220HV
EN-GJS-600-3	600	3	180-260HV
SiMoCr DCI	**606**	**14**	**298 ± 10.67HV**

Table 4.8 shows that SiMoCr DCI will be a good contender for the engineering applications in which the mentioned DCI grades are used presently.

CHAPTER 5

EVALUATION OF JOHNSON-COOK MATERIAL MODEL PARAMETERS

5.1 Johnson-cook material model

Johnson-Cook is a type of material model used for solving engineering problems where strain rates vary over a large range and adiabatic temperature increases due to plastic heating resulting in the softening of the material. The plasticity model represented by Johnson & Cook (1983), defines the value of plastic stress as the product of three functions as given in Eq. (5.1). The first bracket describes a power function expressing the strain hardening effect during plastic deformation. The second bracket is a function of the influence of strain rate on the value of strain hardening depicting the quotient of strain rate to the strain rate at quasi-static load. The third bracket describes the weakening effect due to recovery or recrystallization temperature. The *J-C* material model (Johnson & Cook, 1983) is given in Eq. (5.1).

$$\sigma_{eq} = (A + B\varepsilon_{eq}^{n})(1 + C ln\dot{\varepsilon}^{*})(1 - T^{*m}) \qquad \text{Eq. (5.1)}$$

Strain hardening effect | Strain rate strengthening effect | Temperature effect

Where, σ_{eq} is the equivalent flow stress, '*A*' is the yield strength of the material under referenced condition, '*B*' is the strain hardening constant, ε_{eq} is the equivalent plastic strain, '*n'* is the strain hardening exponent, '*C'* is the strain rate strengthening co-efficient, $\dot{\varepsilon}^{*}$ is the dimensionless ratio of strain rate to the reference strain rate, *T** is the

homologous temperature and '*m'* is the thermal softening co-efficient. In the present study, the parameters *A, B, n, C* and *m* are determined by taking the reference strain rate and reference temperature as 0.1/s and 623 K respectively.

5.2 Experimental procedure

5.2.1 Specimen preparation

The sub-size tensile specimens are machined on a lathe machine from the cast cylindrical bars of the three melts in accordance with ASTM A370-03a standard.

Fig. 5.1 Tensile test specimens for evaluation of *J-C* parameters

5.2.2 Tensile tests

A series of uniaxial tension tests are performed at four-strain rates (0.1 s^{-1}, 0.01 s^{-1}, 0.001 s^{-1} and 0.0001 s^{-1}) and four temperatures (298K, 423K, 523K and 623K) on a 50 kN universal testing machine (UTM) on the prepared specimens of three melts: Melt-1, Melt-2 and Melt-3 respectively. Three specimens of each melt are tested at each strain rate to capture the scatter in the results. The engineering stress and engineering strain plots are prepared using the Force vs. Displacement data acquired from a HORIZON software connected to the UTM machine. The data obtained from the plots are further converted

into true stress-true strain plots using standard equations. Similarly, the tensile tests are also conducted at 423K, 523K and 623K respectively in an environmental chamber attached with the UTM. The environment chamber is used to maintaintain the requisite temperature for conducting the tensile experiments.

5.3 Results and discussion

5.3.1 Tensile properties

A few of the broken specimens at various strain rates (10^{-4} s^{-1}, 10^{-3} s^{-1}, 10^{-2} $s^{-}1$ and 10^{-1} s^{-1}) are shown in Fig. 5.2. The tensile strength and percentage elongation data of the sub-sized specimens tested is evaluated and converted into true stress-true strain plots.

Fig. 5.2 Representative broken specimens of tensile test

Such true stress-true strain plots for Melt-3 are shown in Fig. 5.3. From these plots, it is observed that the strain rate is directly proportional to the tensile strengths of the specimens i.e., the higher the strain rate higher the tensile strength. This could be attributed to the lower time given to the tensile specimens to undergo recovery during

plastic deformation at a higher rate. It is also observed that ductility is inversely proportional to the rate of deformation i.e., higher the strain rate lower is the ductility.

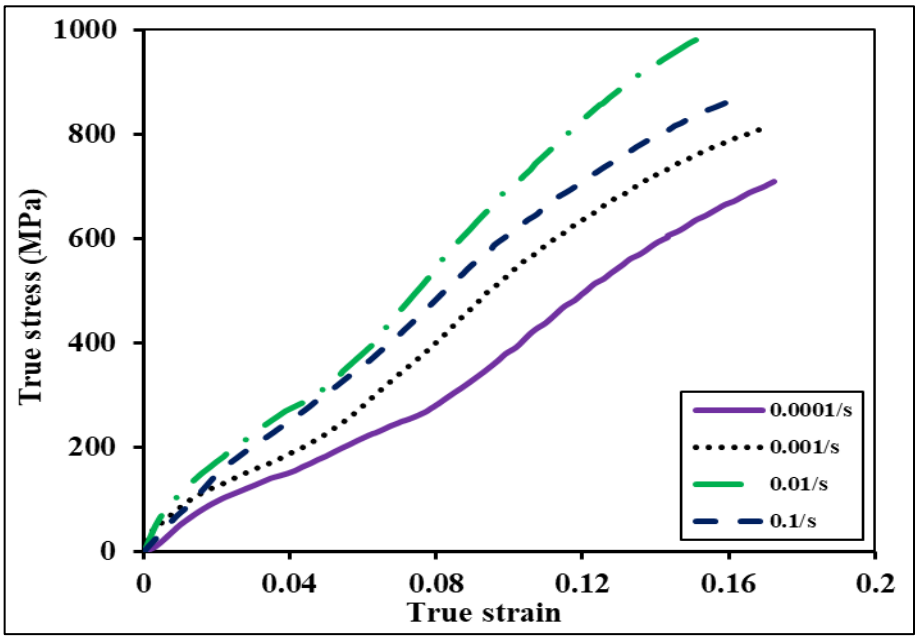

(a) Room temperature

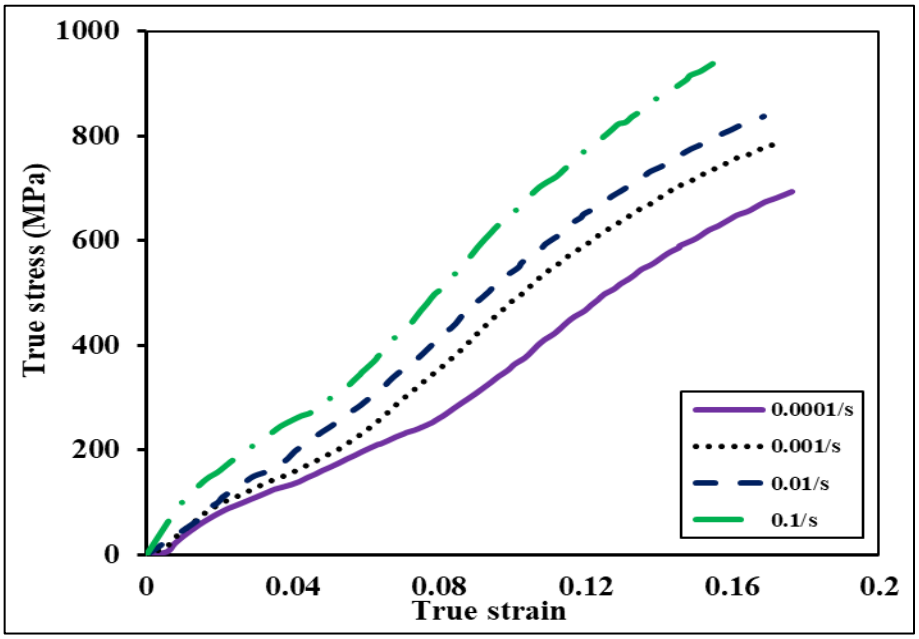

(b) 423K

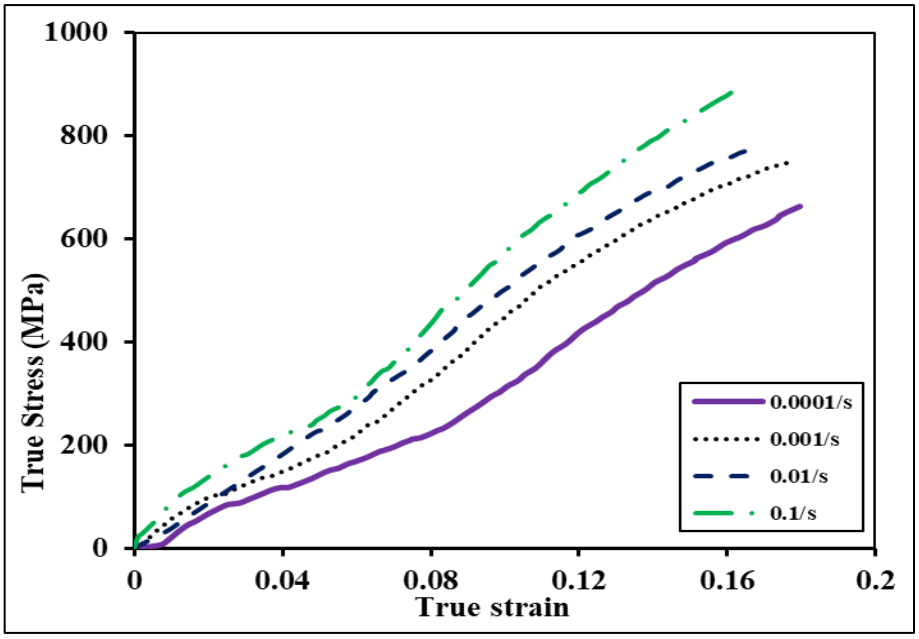

(c) 523K

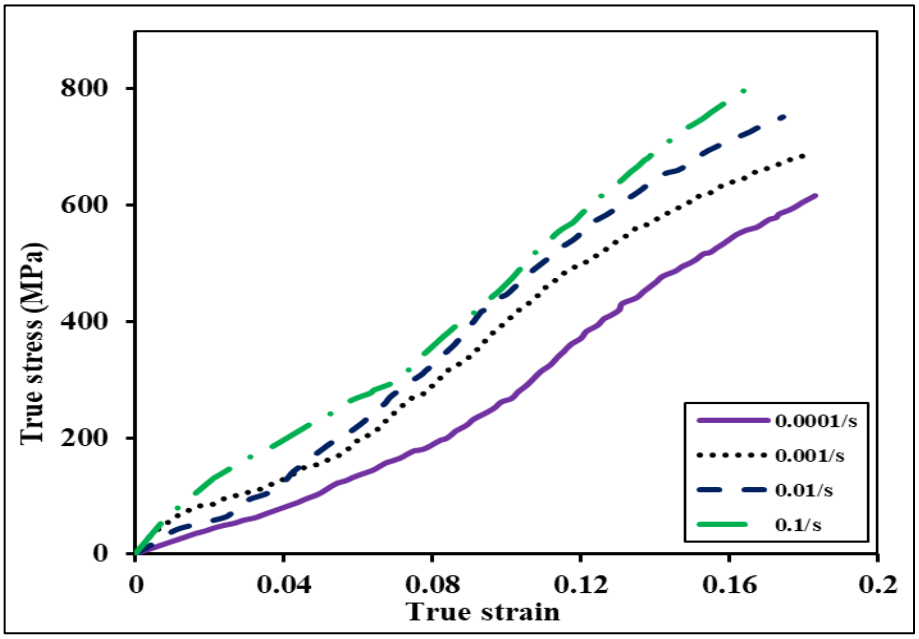

(d) 623 K

Fig. 5.3 True stress-true strain plots of Melt-3

The reason for the lower ductility can be attributed to the sessile dislocations getting locked due to higher strain rates. The tensile tests conducted at elevated temperatures show a lower value of tensile strength and higher ductility as the temperature increases. The phenomenon of recovery gets sufficient time for the glide of dislocations during deformation at higher temperatures.

5.3.2 Johnson-Cook Parameters determination

5.3.2.1 Determination of parameter 'A'

Parameter *'A'* is known as the yield strength of the material. From literature, it is found that some materials do not clearly exhibit the yield stress point and for such materials 0.2 % offset method is used to find the yield point. In the present study, the SiMoCr ductile cast iron does not exhibit the yield point therefore, a 0.2% offset method is used to find the yield strength of the developed material.

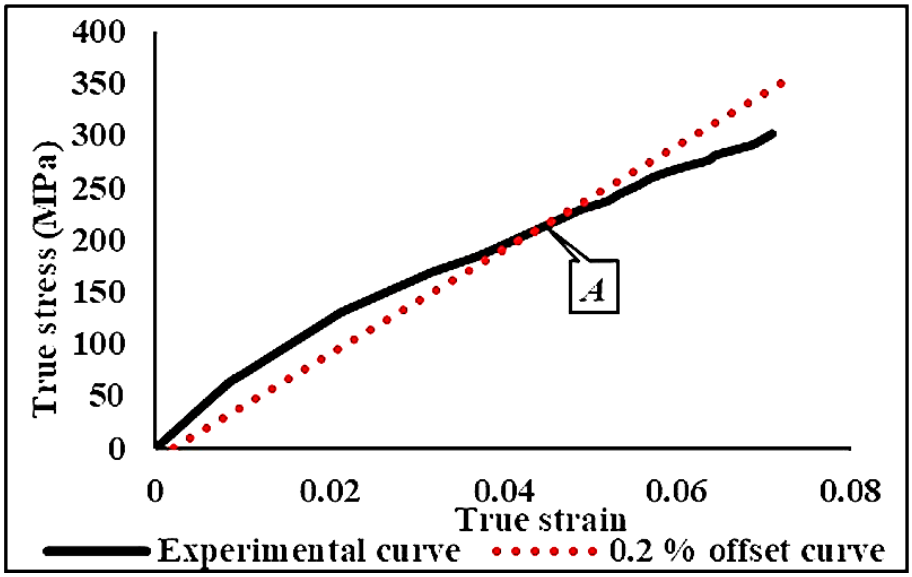

Fig. 5.4 Estimation of yield point *'A'* using 0.2% offset method

The true stress-true strain plot at reference strain rate and reference temperature is taken for finding the yield point as shown in Fig. 5.4 for Melt-3. A straight line is drawn, parallel to the Hooke's line in the elastic region of the curve, which starts from the 0.002 strain offset value and intersects the true stress-true strain curve at some point known as yield point as shown in Fig. 5.4. This point is known as yield point 'A' and its value is observed to be 214 MPa and referred in further calculations for finding the rest of *J-C* parameters. Similar procedures are also followed for Melt-1 and Melt-2 specimens. The yield point for Melt-1 and Melt-2 is observed as 208MPa and 229 MPa respectively.

5.3.2.2 Determination of parameters ‘B’ and ‘n’

The parameters *‘B’* and *‘n’* of *J-C* material model are calculated by considering the deformation experiments at a temperature equal to a reference temperature and a deformation strain rate equal to the reference strain rate. Eq. 5.1 is modified accordingly as

$$\sigma_{eq} = \left(A + B\varepsilon_{eq}^{n} \right) \quad \text{Eq. (5.2)}$$

For uniaxial tensile strength

σ_{eq} becomes σ and,

$\varepsilon_{eq} = \varepsilon$,

therefore, Eq. 5.2 is further modified to

$$\sigma = (A + B\varepsilon^{n})]$$

After rearranging the parameters and taking the natural logarithm on both sides, the modified equation obtained as

$$\mathrm{Ln}(\sigma - A) = lnB + n\, ln\varepsilon \quad \text{Eq. (5.3)}$$

By taking the flow stress and strain values under referenced strain conditions at reference temperature into Eq. 5.3 and using the first order regression mode (Murugesan & Jung, 2019), the linear relationship plot between $'\ln(\sigma - A)'$ and $'ln\varepsilon'$ is drawn and shown in

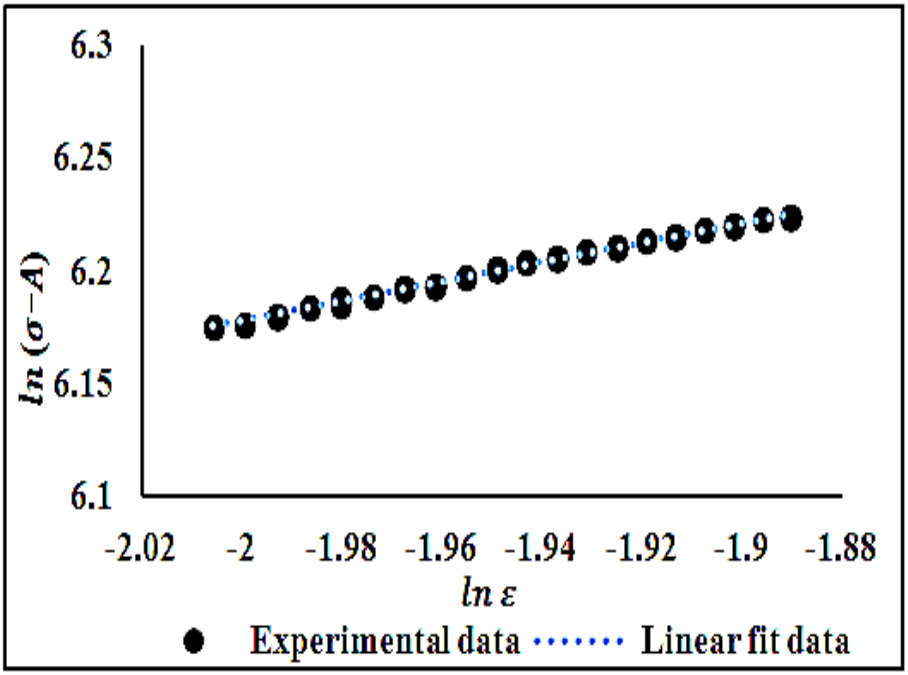

Fig. 5.5 Plot showing $\ln(\sigma - A)$ vs. $ln\varepsilon$ at referenced conditions

Fig. 5.5 for Melt-3. It is found that 99 percent of data lies very close to the regression line confirms the better predictability of the parameters. From the slope and intercept of the fitted curve, the material constant *'B'* and '*n*' are estimated as 1022 MPa and 0.45. Similarly, for Melt-1 and Melt-2, the values of parameter *'B'* and '*n'* are estimated.

5.3.2.3 Determination of parameter '*C*'

For estimation of parameter *'C'* the deformation temperature is considered equal to room temperature under uniaxial tensile test conditions. Eq. 5.1 is modified as given below (Murugesan & Jung, 2019).

$$\sigma = (A + B\varepsilon^{n})(1 + Cln\dot{\varepsilon}^{*}) \qquad \text{Eq. (5.4)}$$

After Rearranging, Eq. 5.4 modified as

$$\sigma/(A + B\varepsilon^{n}) = (1 + Cln\dot{\varepsilon}^{*}) \qquad \text{Eq. (5.5)}$$

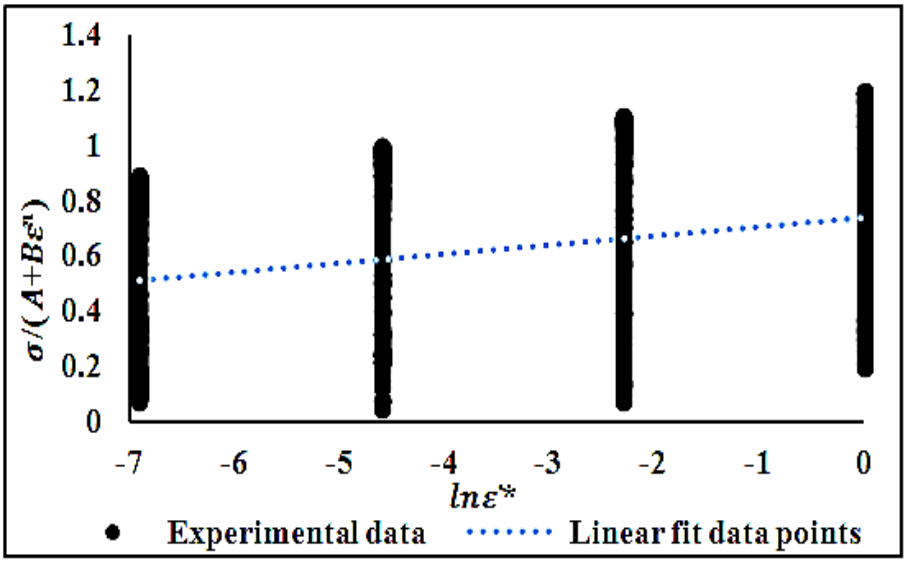

Fig. 5.6 Plot showing $\frac{\sigma}{A+B\varepsilon^n}$ vs. $ln\dot{\varepsilon}$ curve at referenced conditions

The graph $\frac{\sigma}{A+B\varepsilon^n} \sim ln\dot{\varepsilon}$ is drawn, in Fig. 5.6, after putting the values of parameters 'A', 'B' and '*n*' obtained so far in Eq. 5.5. Considering the flow stress value at all the four strain rates (10^{-4} s^{-1}, 10^{-3} s^{-1}, 10^{-2} s^{-1} and 10^{-1} s^{-1}), the linear fitting is carried out using the first order regression model. The slope of linear curve fitting results in the value of the material constant '*C*' and is estimated as 0.033. The fitted curve intercepts the y-axis at a different point other than 1, which is neglected and considered as 1 in this study.

5.3.2.4 Determination of parameter '*m*'

When the reference strain rate and deformation strain rates are equal, Eq. 5.1 can be simplified as given in Eq. 5.6.

$$\sigma_{eq} = \left(A + B\varepsilon_{eq}^{n} \right)(1 - T^{*m}) \quad \text{Eq. (5.6)}$$

The term T^* known as the homologous temperature is expressed as the temperature of the material as a function of its melting point temperature using the kelvin scale (Viswanadham & Singh, 1998) and calculated as

$$T^* = \frac{T - T^{ref}}{T_m - T^{ref}} \quad \text{Eq. (5.7)}$$

where,

T* = homologous temperature

T = Deformation temperature

T^{ref} = Reference deformation temperature (623 K), and

T_m = Melting temperature of the material (1523 K)

After rearranging the Eq. 5.7,

$$1 - (\sigma_{eq} / (A + B\varepsilon_{eq}^{n})) = T^{*m} \quad \text{Eq. (5.8)}$$

By taking log on both sides, Eq. 5.8 becomes

$$\text{Ln}\,(1 - (\sigma_{eq} / (A + B\varepsilon_{eq}^{n}))) = m ln T^{*} \quad \text{Eq. (5.9)}$$

The plot between ln $(1 - (\sigma_{eq} / (A + B\varepsilon_{eq}^{n})))$ and lnT^{*} is shown in Fig. 5.7 for reference strain rate at room temperature, 423 K and 523 K. On observing Fig. 5.7, the slope of the linear fit data points, by using the first order regression model, gives the value of thermal softening coefficient 'm' as 0.37.

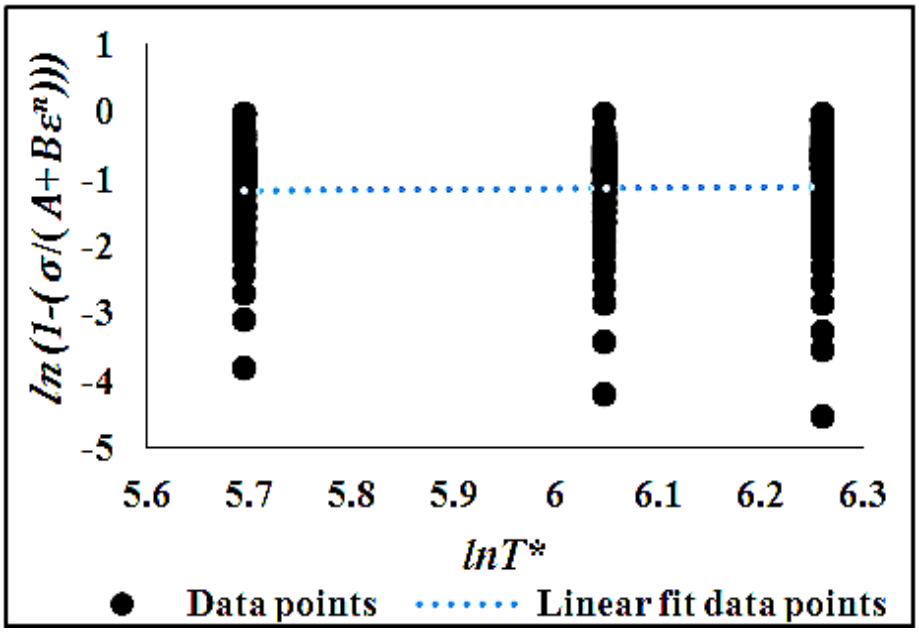

Fig. 5.7 $ln[1 - (\frac{\sigma}{A+B\varepsilon^{n}})]$ and $Ln[\dot{\varepsilon}]$ curve at referenced conditions

Table 5.1 Johnson-Cook material model parameters of SiMoCr DCI

Parameters	Estimated *J-C* parameters values				
	A (MPa)	B (MPa)	n	C	m
Melt-1	208	1053	0.48	0.032	0.38
Melt-2	229	1074	0.46	0.036	0.4
Melt-3	214	1022	0.45	0.033	0.37

Similar methods are adopted for Melt-1 and Melt-2 and the estimated *J-C* parameters for the three melts are summarized in Table 5.1. After putting these parameters values in Eq. (5.1) for Melt-1, the relation among stress, strain, deformation strain rate and estimated flow stress (σ_{est}) at room temperature is given in Eq. (5.10).

$$\sigma_{est} = (208 + 1053\dot{\varepsilon}_{eq}^{0.48})(1 + 0.032 \ln (\frac{\dot{\varepsilon}}{0.1}))(1 - (T^*)^{0.38}) \quad \text{Eq. (5.10)}$$

Similar equations are also formed for Melt-2 and Melt-3 for estimating the flow stress values as Eq. 5.11 and 5.12 respectively.

$$\sigma_{est} = (229 + 1074\dot{\varepsilon}_{eq}^{0.46})(1 + 0.036 \ln (\frac{\dot{\varepsilon}}{0.1}))(1 - (T^*)^{0.4}) \quad \text{Eq. (5.11)}$$

$$\sigma_{est} = (214 + 1022\dot{\varepsilon}_{eq}^{0.45})(1 + 0.033 \ln (\frac{\dot{\varepsilon}}{0.1}))(1 - (T^*)^{0.37}) \quad \text{Eq. (5.12)}$$

The *J-C* parameters, listed in Table 5.1, calculated for Melt-1, Melt-2 and Melt-3 are used in the finite element simulation in various engineering applications using these developed SiMoCr DCI materials.

CHAPTER 6

EVALUATION OF FRACTURE TOUGHNESS

6.1 Fracture toughness

Fracture toughness, a material property, presents important information on the material behaviour under static loading conditions in the presence of a sharp natural crack. For the behaviour of a material in a linear elastic approach prior to the failure by developing a small plastic zone as compared to the dimensions of the specimens, the critical value of Mode-I stress intensity factor K_{IC} becomes a crucial fracture parameter for the material. In ASTM E 399-20, K_{IC} is mentioned as 'plane strain fracture toughness.'

6.2 Experimental procedure

6.2.1 Sample preparation

The samples for fracture toughness i.e., single edge-notched beam (SENB), are prepared by machining and surface finishing operations with a tolerance of ±50μm with the dimensions as shown in Fig. 6.1. A notch size of 1.5±0.05mm in width and 7±0.05mm parallel depth ending with a V-notch of 1.5mm in depth and with an included angle of 45° is prepared by the wire-cut electric discharge machining. To observe the effect of a sharp crack equivalent to a natural crack, samples are prepared with a fatigue pre-crack located at the notch vertex. To find the crack mouth opening displacement (CMOD), the knife edges are required to be fixed on the bottom side of the specimen to accommodate the clip-type gauge for CMOD measurements. The knife edges are prepared separately by machining from a steel strip of equal thickness as that of the three-point bend specimen.

The knife edges are metallic strips of uniform thickness having an acute angle sharp edge at one end for attaching the arm of the clip gauge as shown in Fig. 6.3. Such knife edges are fixed to the notched side of the specimen below the notch using a special epoxy resin along the length in such a way that the span length is not affected during bending, shown in Fig. 6.2.

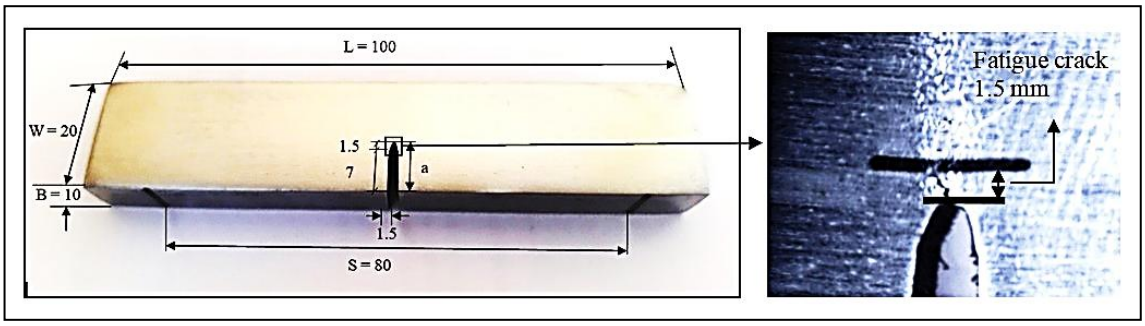

Fig. 6.1 A standard specimen with for the three-point bend test with magnified view of fatigue pre-crack

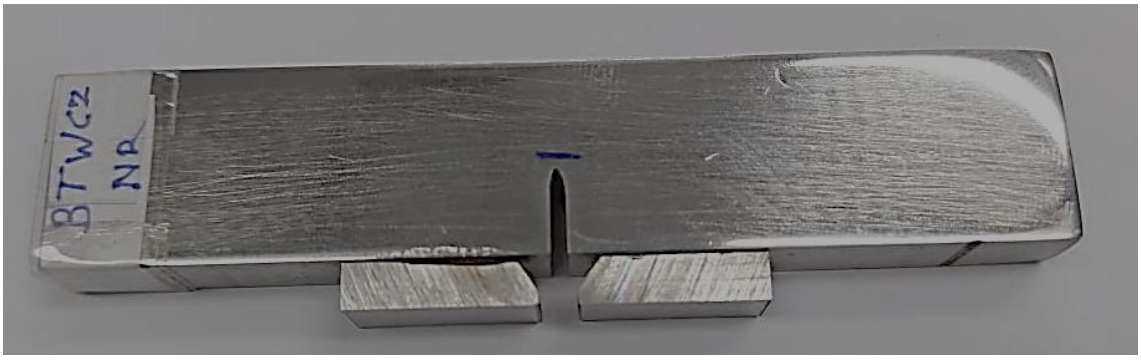

Fig. 6.2 A standard specimen for the 3-point bend test with knife edge attachment

A total of 9 test specimens are prepared with a sharp fatigue crack of zero openings from the three melts. To prepare the specimens with a fatigue pre-crack of length approximately 0.5mm initiated from the vertex of the notch root along the width of the specimens, the specimens are mounted on a dynamic testing machine (make: MTS, Model: 858 Tabletop with 25kN capacity). The mean load and amplitude load used for fatigue pre-crack are 2200N and 1800N, respectively, at a frequency of 20 Hz. The average number of cycles required for producing a pre-crack length of 0.5 mm is

approximately 89,550 cycles in Melt-1 specimens while in Melt-2 and Melt-3 specimens approximately 91000 and 93230 cycles respectively.

6.2.2 Determination of fracture toughness

To determine the fracture toughness, a common three-point bend test is performed as per the standard test procedure. The clip-type gauge is employed to assess the crack mouth opening displacement (CMOD) during the loading of the specimen in bending. For CMOD measurement, clip gauge jaws are rested against the knife edges fixed to the specimen. The specimen is simply supported on the two roller supports and loaded in bending with the help of a roller punch fixed to the crosshead of the machine as shown in Fig. 6.3.

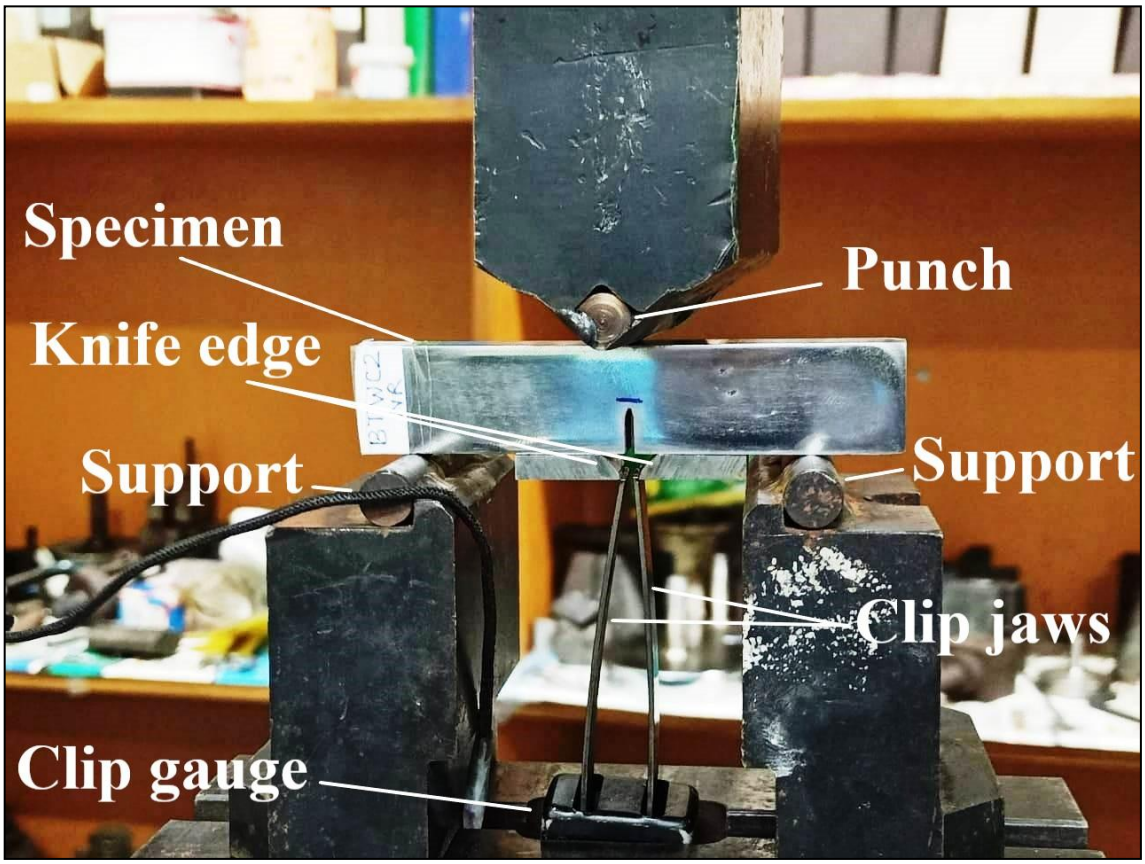

Fig. 6.3 Three-point bend test setup on a dynamic testing machine

Initial position values are recorded, and the bending load is applied gradually till the fracture by following the pre-crack path. The test is repeated for all the specimens made

from Melt-1, Melt-2 and Melt-3. The load, displacement, and CMOD data are recorded for further analysis for calculating the critical stress intensity factor of the material under consideration.

Fracture toughness (K_{IC}) in-plane strain condition for the material is determined by an equation given by Kumar (2009) as given below:

$$K_{IC} = \frac{3S\sqrt{a}}{2BW^2} Y\left(\frac{a}{W}\right).F \qquad \text{Eq. (6.1)}$$

where,

$$Y\left(\frac{a}{W}\right) = \frac{1.99-\frac{a}{W}\left(1-\frac{a}{W}\right)\left[2.15-3.93\frac{a}{W}+2.7\left(\frac{a}{W}\right)^2\right]}{\left(1+2\frac{a}{W}\right)\left(1-\frac{a}{W}\right)^{\frac{3}{2}}}$$

The force '*F*' is obtained from the force vs. displacement diagram obtained from the three-point bend experiments, '*a*' is the initial crack length, *'W'* is the height of the specimen and '*B*' is the thickness of the SENB specimen. '*S*' is the span length between two rollers supports in mm, as shown in Fig. 6.1 and 6.2.

6.2.3 Numerical simulation

To study and analyze the material behaviour several analytical and numerical techniques have been developed by the researchers. Among such methods, Finite Element Analysis (FEA) is currently the most employed mathematical tool in the hands of researchers to get the desired results. Unlike conventional methodologies which comprise empirical formulae and numerous trial-and-error procedures and consequences in wastage of material, time and effort, the finite element analysis approach has developed as an effectual way of simulating the bending procedures and forecasting fracture toughness using three-point bend test simulation. The key idea of FEM is to split the object into finite elements, linked by nodes. To obtain an approximate solution a set of algebraic equations are developed from space and time discretized form of virtual work expression (Fish & Belytschko, 2007). Such finite element equations are worked out to get the nodal

displacements of the element, which further act as input to the element operator matrices for computing the desired outputs at element integration points.

In this present study, the fracture toughness of the material has been predicted using a three-point bend test simulation by finite element analysis in ABAQUS (6.14-1) software. The methodology of modelling and simulation is presented below.

6.2.3.1 Modelling and simulations

To carry out the simulations of the 3-point bend test, a full-sized 2D deformable SENB specimen is modeled separately for each melt's specimen as per the dimensions shown in Fig. 6.4. The material properties obtained from the uniaxial tensile experiments are assigned to the specimen with the Young's Modulus and a Poisson's ratio data taken from the literature. The section is assigned to the specimen with a plane stress/strain ratio of 10. The tensile properties of the material are assigned in the material model by giving the true stress vs. true strain values taken from the uniaxial tension test. The fatigue pre-crack of 0.5 mm is created in the interaction module using contour integral. For this, a sharp crack with zero thickness is generated at the tip of the v-notch by sketching a section of 0.5mm, and a circle with a center at the crack tip is sketched on the specimen surface and extended throughout the section of the specimen to divide into two cells. A seam is assigned to the partition above the notch for a crack. The crack extension direction is also selected in the +y direction by assigning q-vectors which are selected using the crack start and endpoints. A biased mesh is created in the crack tip as shown in Fig. 6.4. Quarter-point nodes value of 0.25 with collapsed element side with the single node is also selected as element control for square-root singularity introduction at the developed crack tip. Quarter-point elements are used at the crack tip to model the square-root singularity of the stress field ahead of the crack tip. Stress intensity factor K_I (SIF) is calculated from the

potential energy release rate or J integral using the expression given in Eq.6.2 for Mode-l plain strain (Kumar, 2009).

$$J = \frac{K_I^2}{\left(\frac{E}{1-v^2}\right)} \qquad \text{Eq. (6.2)}$$

where,

J – is the *J*-integral value obtained from the FE analysis,

E – is the young's modulus,

v – is the poisson's ratio.

A plane strain state exists all along the crack front, the plane strain modulus $\left(\frac{E}{1-v^2}\right)$ is used in the above expression independent of the far-field stress state. *J*-integral is equal to the potential energy release rate per unit of crack extension. *J*-integral is less sensitive to inaccuracy in computations in crack front elements as it is a global parameter. The path-independence property of *J*-integral is used to calculate an accurate value of *J*-integral by taking the contour in the region where finite element analysis yields more accurate calculations of displacements and stresses.

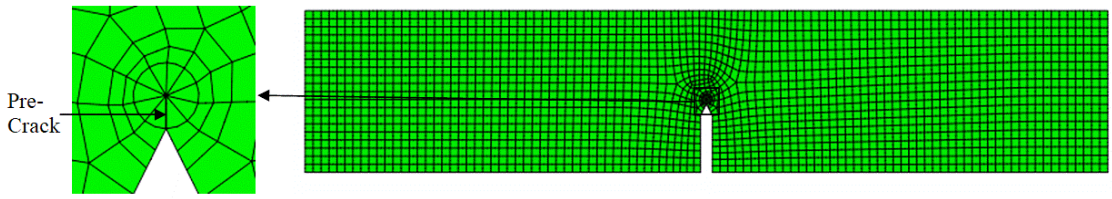

Fig. 6.4 A meshed model of SENB specimen magnified view of pre-crack

A 1mm global seed is assigned to the specimen while the local edge seeds are assigned in the circular region around the crack tip using quad-dominated sweep mesh controls. Quad element shape is assigned to the rest of the part of the specimen using quad elements and medial axis algorithm. Quadratic, reduced integral plane strain elements, CPE8R, are assigned to the whole specimen.

6.2.3.2 Boundary conditions and simulations

The SENB specimen is positioned in such a way that the two datum points at the bottom edge with a span of 80 mm (the same as the distance between the two support pins in the actual experiment) by applying a boundary condition to restrict its vertical displacement during bending simulations. A static general step named step-1 with geometric nonlinearity is selected for the step. The number of increments is restricted upto 1000, with the initial increment set as 0.01, minimum increment set as $1e^{-5}$, and maximum increment set as 1.

Two history outputs are created for the specimen and crack, respectively. In the history output for crack, J-integral is chosen with five numbers of contours. The load is applied in '–y' direction during bending. In the experiment conducted to calculate fracture toughness, the load is found at which the crack starts growing leading to specimen fracture. The stress intensity factor (SIF) calculated at the failure load, for the specimen geometry, is the critical fracture toughness or critical SIF of the material.

A similar procedure of numerical simulation is used for the calculation of fracture toughness for Melt-2 and Melt-3 also.

6.2.4 Scanning electron microscope (SEM) analysis

6.2.4.1 Specimen preparation

The specimen for SEM analysis need not require any special mounting as DCI itself is a good conductor. The specimens of size 10mm×5mm×5mm, shown in Fig. 6.5, are cut from the tested specimens using an abrasive cutter. The specimens are cleaned properly in acetone solution and ultrasonicator for the removal of any foreign material from the specimen surfaces.

Fig. 6.5 Specimens for SEM analysis

6.2.4.2 Scanning electron microscope (SEM) analysis

The microshrinkage porosity of the experimental melts is studied using SEM analysis. Scanning electron microscopic (SEM) examination is carried out on the prepared surface of the specimens, shown in Fig. 6.6. Microscopic examination is done at different working distances and magnification levels in a vacuum chamber designed to have a vacuum pressure of 10^{-4}mbar. The micrographs obtained by scanning electron microscope at a magnification of 200X are analyzed and scanned for micro-cavities over an area of 2.0 mm^2 as per standard ASTM B276-05 and the micrographs are shown in Fig. 6.13.

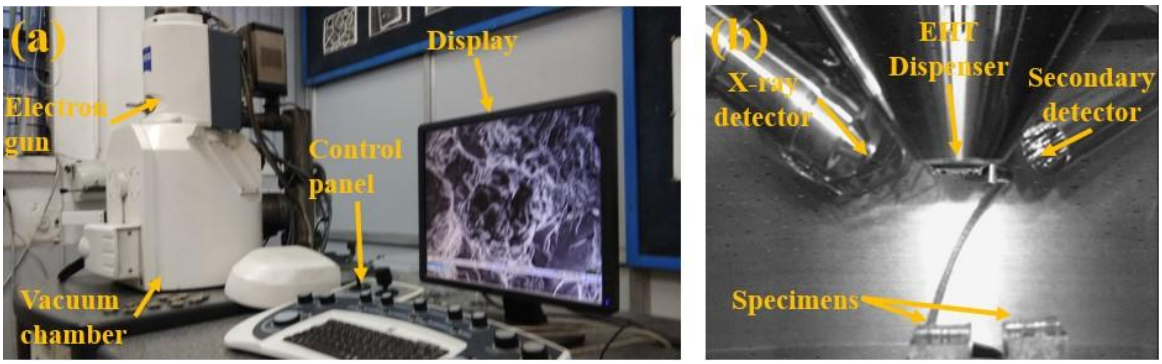

Fig. 6.6 (a) Scanning electron microscope setup, (b) inside view of vacuum chamber

6.3 Results and discussion

6.3.1 Fracture toughness

The force vs. CMOD plots obtained from the experiments of 3-point bend tests of the specimens with fatigue pre-crack are shown in Fig. 6.7. The plot depicts a steep rise in bending load during the first part of the plot and then load decreases gradually indicating the inability of the specimen to sustain further increase in loads due to crack propagation. It is observed during the 3-point bend test that specimens from Melt-2 undergo higher deflection at much higher bending loads followed by the specimens of Melt-1 and Melt-3, respectively. As evident from the values of crack mouth opening displacement, the crack propagates earlier in the specimens of Melt-3 followed by the specimens of Melt-2 and Melt-1. This could be attributed to the nodule numbers and geometry playing a role in arresting and reorienting the crack path.

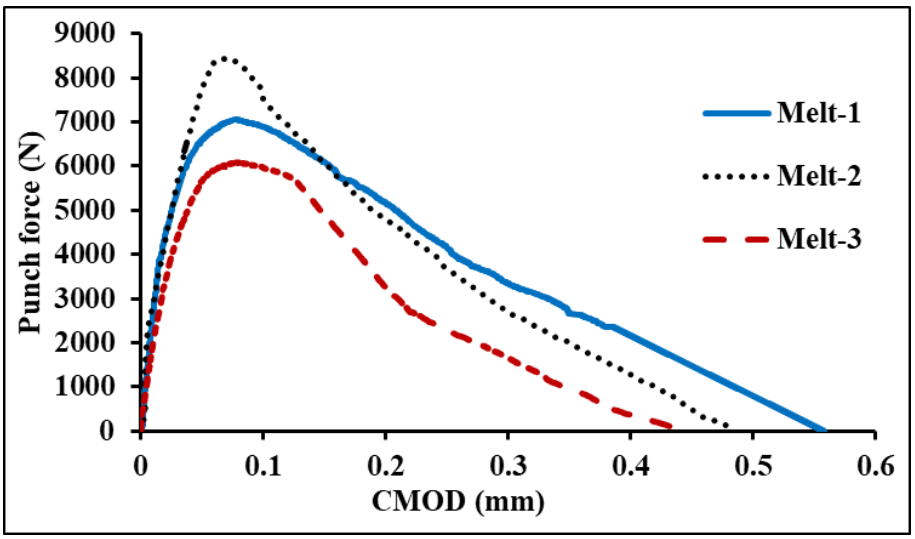

Fig. 6.7 Force vs. CMOD plots

The values of static fracture toughness obtained from the experiments for the specimens taken from Melt-1, Melt-2, Melt-3 and finite element simulations are given in Table 6.1.

The fracture toughness of the specimens of Melt-2 is the highest with a value of 54.49 MPa$\sqrt{m}$ followed by the specimens of Melt-1 and Melt-3 with fracture toughness values of 47.52MPa$\sqrt{m}$ and 39.48 MPa$\sqrt{m}$, respectively.

Table 6.1 Comparison of experimental and simulation results

Melt	Fracture toughness (MPa √m)		J-integral (N/m)	
	Experimental	Simulations	Experimental	Simulations
Melt -1	47.52	49.17	14061.38	15055.01
Melt -2	54.49	56.56	20064.85	20124.79
Melt -3	39.48	41.88	10528.96	10921.8

The results of fracture toughness values computed from the simulations for the samples of Melt-1, Melt-2 and Melt-3 are 49.17MPa$\sqrt{m}$, 56.56 MPa$\sqrt{m}$, and 41.88 MPa$\sqrt{m}$, respectively which are found in good agreement with the obtained findings from empirical relations using experimental data. The values of *J*-integral obtained from experimental data and simulations are also given in Table 6.1.

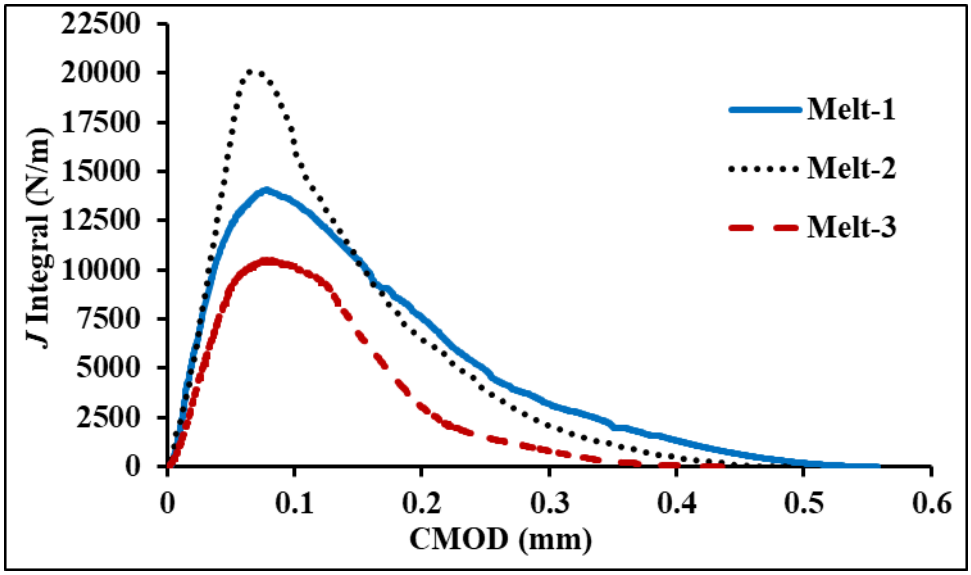

Fig. 6.8 Variation of J-integral w.r.t. crack mouth opening displacement plots

The value of *J*-integral is highest for the specimens of Melt-2 followed by the specimens of Melt-1 and Melt-3. A similar trend is reflected in the results obtained from the simulations. The variation of values of *J*-integral concerning CMOD obtained from experiments is also shown in Fig. 6.8, which depicts the consistent trend as observed in Fig. 6.7.

The results obtained from the simulations of the 3-point bend of SENB specimens representing the Melt-1, Melt-2, and Melt-3 are shown in Fig. 6.9.

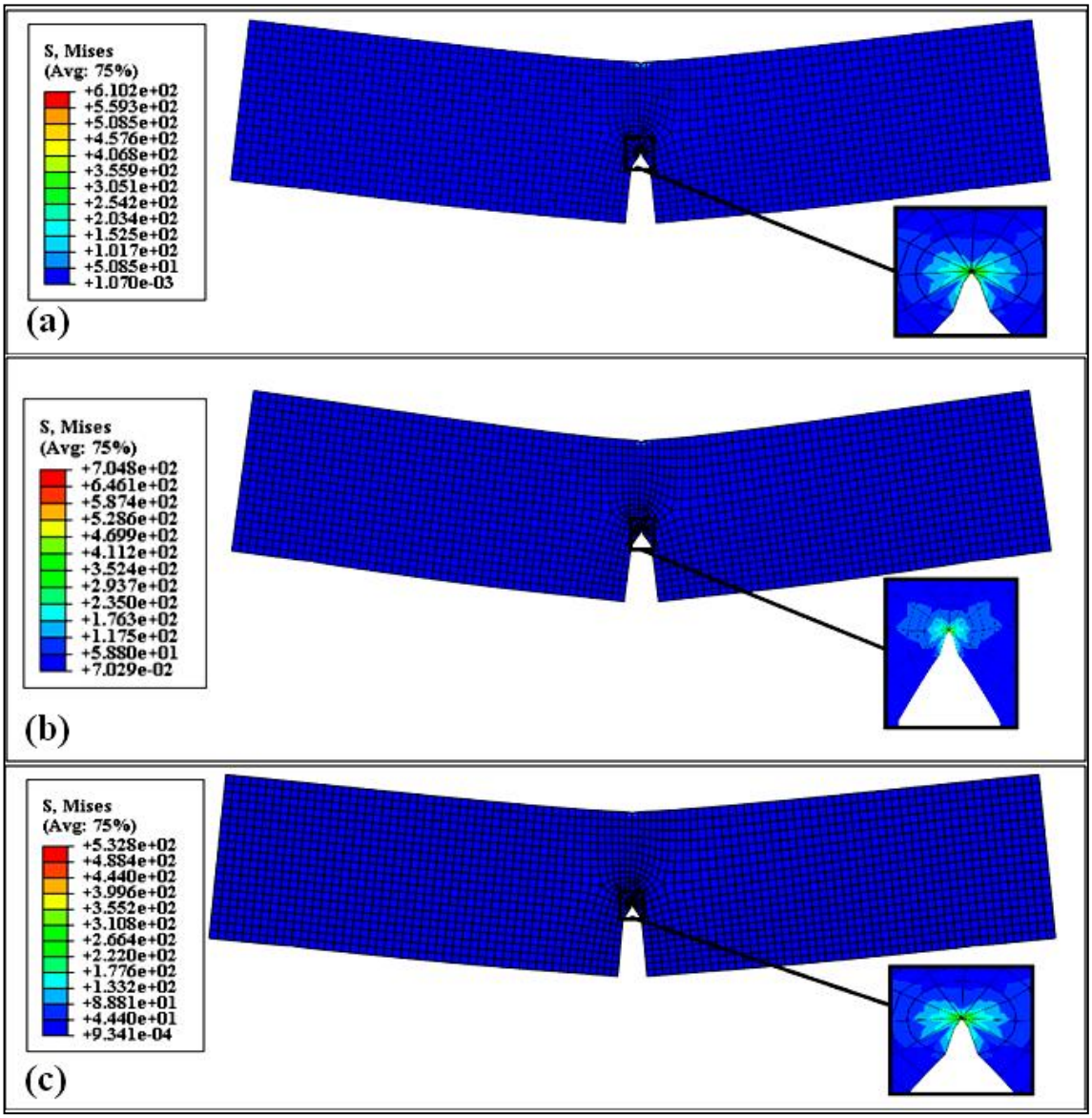

Fig. 6.9 Simulation results showing variation in stress during the 3-point bend test of SENB specimens of Melt-1(a), Melt-2(b), and Melt-3(c)

It is observed from the stress contour plots that the simulation results of bending of the specimen of Melt-2 show the maximum stress under the same deflection followed by the results of the bending simulation of the specimens of Melt-1 and Melt-3, respectively. This can be attributed to the tensile strengths of the respective materials. A tested SENB specimen is also shown in Fig. 6.10. The true stress-true strain data taken from the tensile test experiments and the load and displacement data obtained from the bending experiments are used in numerical simulation to determine the stress distribution in the SENB specimens.

The values of J-integral are calculated from the resulting stress distribution. Thus, critical fracture toughness is calculated which is observed to be close to the values from the experimental results.

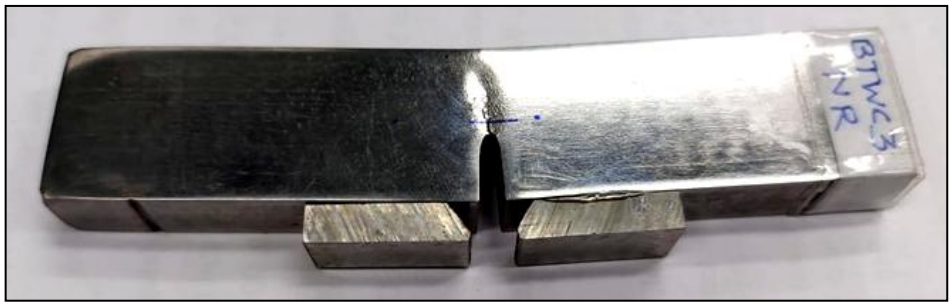

Fig. 6.10 A tested SENB specimen

6.3.2 Microstructural analysis of fractured surface

To explain the variation of material properties regarding the microstructure, a comprehensive study is done on the selected tested SENB samples of the 3-point bend experiment using a scanning electron microscope. All the tested specimens revealed an irregular fractured surface having uneven peaks and valleys as shown in Fig. 6.11. Some small inclusions are also observed in the micrograph.

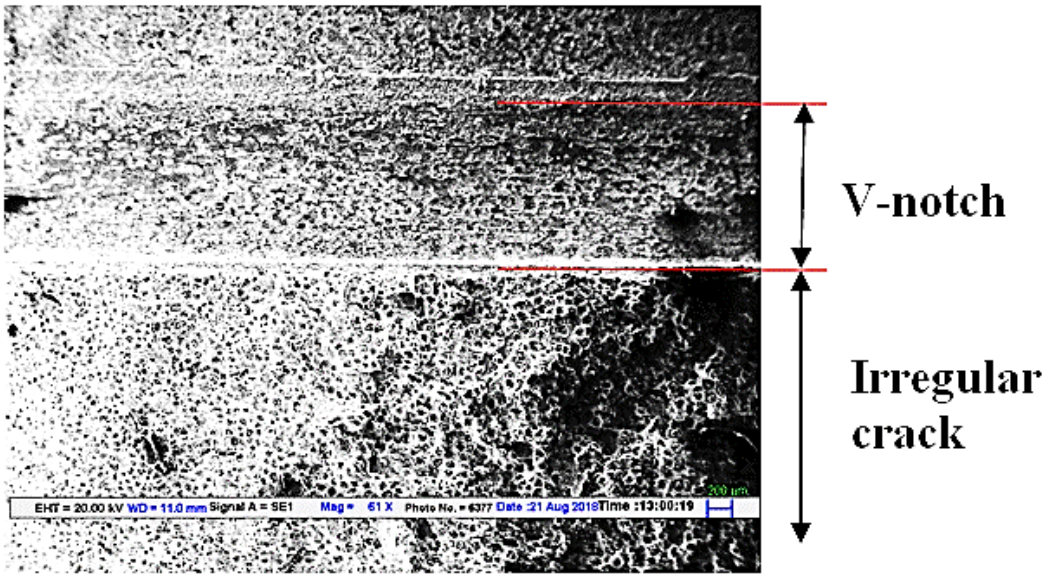

Fig. 6.11 A micrograph showing a fractured surface with an irregular crack front

The spherical nodule plays a significant role in arresting the crack and reorients the crack path around the nodule as observed at higher magnification in the tested specimens of Melt-1 as shown in Fig. 6.12. A fibrous cleavage appearance is also observed in the nodules as observed in Fig. 6.12.

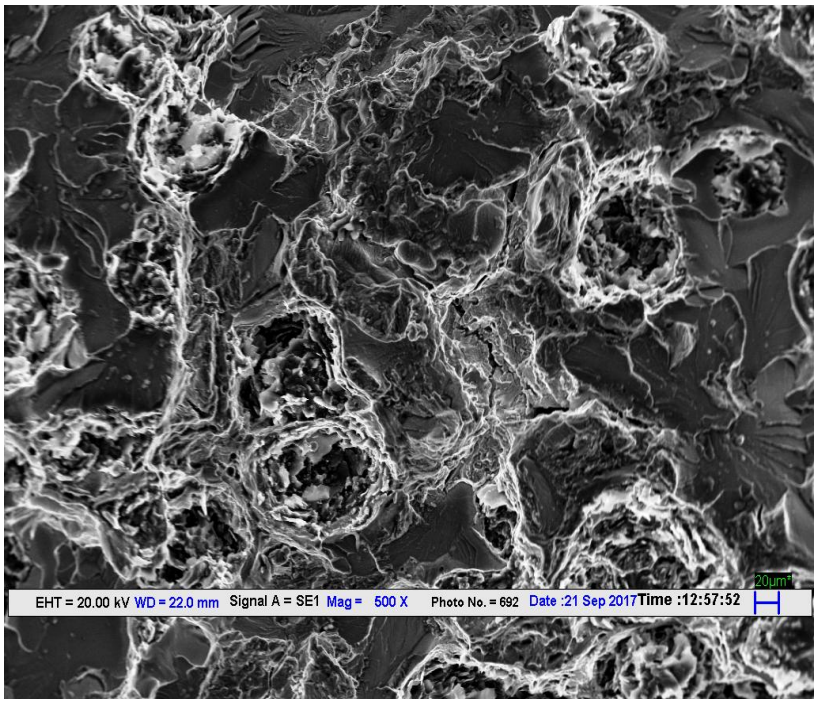

Fig. 6.12 Crack path reorientation phenomenon in the specimen of Melt-1

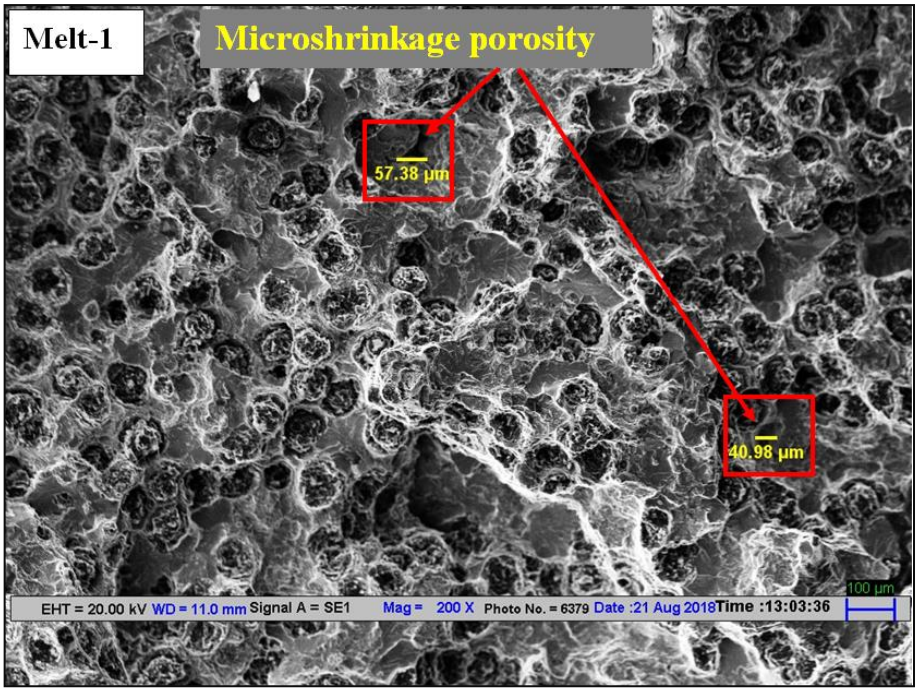
Melt-1
Microshrinkage porosity
57.38 µm
40.98 µm
EHT = 20.00 kV WD = 11.0 mm Signal A = SE1 Mag = 200 X Photo No. = 6379 Date :21 Aug 2018 Time :13:03:36
100 µm

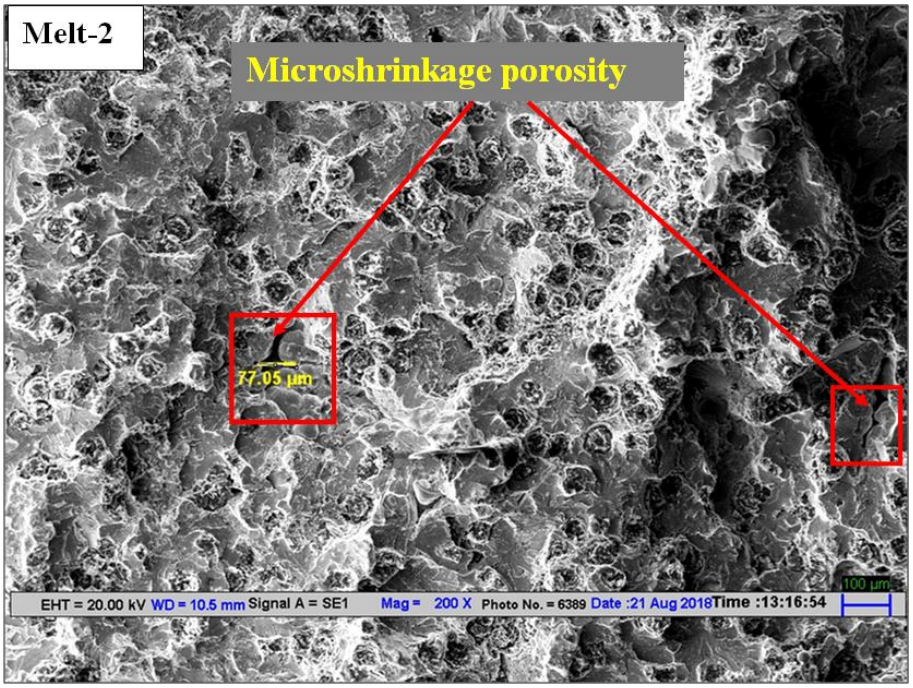
Melt-2
Microshrinkage porosity
77.05 µm
EHT = 20.00 kV WD = 10.5 mm Signal A = SE1 Mag = 200 X Photo No. = 6389 Date :21 Aug 2018 Time :13:16:54
100 µm

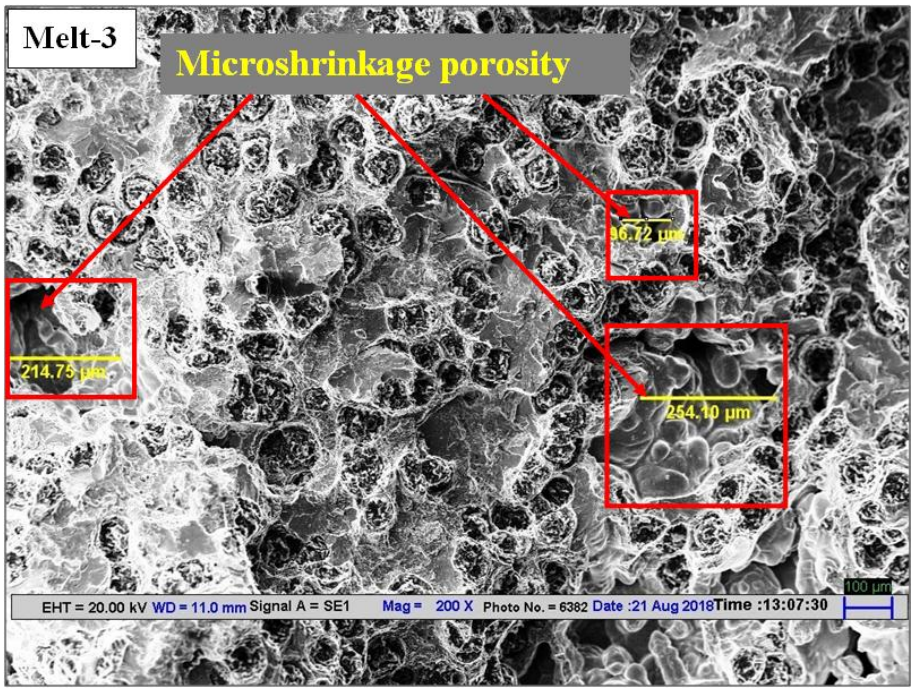

Fig. 6.13 SEM micrographs showing microshrinkage porosity

It is observed from Fig. 6.13 that minimum porosity is seen in the specimens of Melt-1 followed by the specimens of Melt-2, whereas the highest microshrinkage porosity is in the samples of Melt-3. The linear size of the micro-cavity obtained from image analysis software varies from 40 µm to 57 µm in the specimens of Melt-1 and 77 µm to 80 µm in Melt-2. The size of the micro-cavity scanned in an area of 2.0 mm^2 in the samples of Melt-3 varies from 96 µm to 254 µm which indicates higher microshrinkage porosity than that of the specimens of other melts. The higher microshrinkage porosity in the samples of Melt-3 may be attributed to the formation of complex carbides due to the presence of higher content of molybdenum in conjunction with chromium. The formation of complex carbides thus increases the likelihood of micro-porosity in the castings. Molybdenum and chromium

are known to act as strong carbide stabilizers. The addition of molybdenum stabilizes the pearlite and increases its strength by refining the grains whereas the addition of chromium increases the oxidation resistance of the material.

CHAPTER 7

CHARACTERIZATION OF WEAR PROPERTIES

7.1 Introduction

A light weight, wear resistant and good heat dissipation rate are the basic requirement of a brake disc material. Development of materials that meet the requirements is a continuous process, upgraded time-to-time and used in braking systems throughout the world since inception. Effective and efficient braking is a need of the automobile industry. The study of wear properties of a material is itself a complex procedure due to several variables, constituents of material, surface properties of the material, temperature, sliding method: translatory or rotary, sliding velocity: high or low, sliding type: dry or wet and sliding pressure, etc. Surfaces are a very complex form of the material, which includes a variety of defects and distortions, resulting in a strong influence on the wear properties of the material. In sliding wear, a nano peak on the hard surface of the sliding pair will increase the rate of surface wear of the relatively softer material surface. The rise in temperature due to rubbing the surfaces during sliding also contributes to higher wear.

In the present study, the developed SiMoCr DCI materials being the harder surface are tested for specific wear rate and coefficient of friction against the relatively soft material of brake disc pad. Specific wear rates and coefficient of friction of the three melts are found against a brake disc pad material using pin-on-disc sliding wear tests. The results of pin-on-disc wear are analyzed and optimized using statistical software for the melt, among the three melts, having better specific wear rate and coefficient of friction.

7.2 Experimental procedure

7.2.1 Specimen preparation- pin and disc

7.2.1.1 Pin

The assembly of a small pin and a pin holder is written as a pin throughout this study. The pin holders (Ø 12mm & 40mm length) are made from mild steel round bars. The pins are made from brake disc pad friction material. The chemical composition of brake disc pad friction material is summarized in Table 7.1.

Table 7.1 Chemical composition of friction pad in %wt.

Si	P	S	Ti	V	Mn	Fe	Cu	Zn	Zr	Sb	C	Al
7.55	4.46	5.26	26.95	4.29	0.36	7.43	15.18	0.21	19.13	3.26	0.069	5.85

In the present study, a 10mm diameter pin size is chosen. For pins, the disc brake pad material is cut into Φ12mm size pieces with the help of a hacksaw and its outer surface is turned into a round shape of Φ10mm diameter on the lathe machine and outer finishing is done with the help of file in such a way that it can easily fit into the blind hole of the pin holder. The pins are cut into pieces of length 10mm using the hacksaw. Pin holders of outer diameter Φ12mm of 40 mm length are prepared with a 5mm deep blind hole of Φ10mm diameter as shown in Fig.7.1. For preparing these pin holders, a mild steel rod of Φ14mm size is taken and turned to the size of Φ12mm on lathe machine. These mild steel rods are further cut into 40mm long pieces using the hacksaw. The drill bit of Φ10mm is used to make the blind holes of 5mm depth on one side of the specimen. Epoxy adhesive is used during the fitting of the pin into the pin holder so that the pin may not get away with the rotating disc from the pin holder during the wear test. A total of sixteen pins are fabricated.

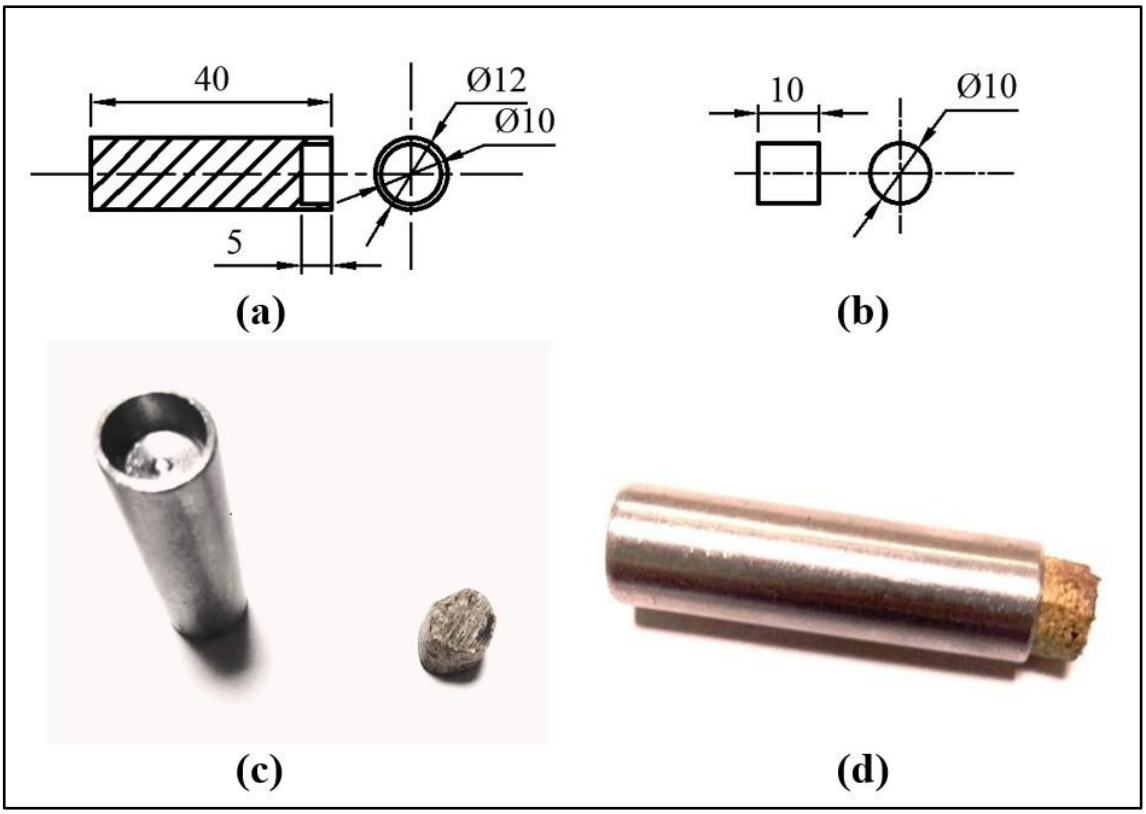

Fig. 7.1 Pin assembly details: (a) pin holder drawing**,** (b) pin drawing, (c) pin holder and pin specimen, (d) pin assembly

7.2.1.2 Disc

The discs for the pin-on-disc wear test as presented in Fig. 7.3, eight in number, are prepared from as-cast plates of SiMoCr DCI by machining and surface finishing operations. The geometrical drawing of the disc is shown in Fig. 7.2. For utilizing both side surfaces of the disc, six equidistantly spaced holes (Ø 4mm) are drilled at a pitch circle diameter of Ø 90mm. These holes are further drilled alternately with the countersunk of Ø 8mm diameter and 4mm deep holes on both sides of the disc as shown in Fig. 7.3 to accommodate the head of screws for fixing the wear disc on the disc holder.

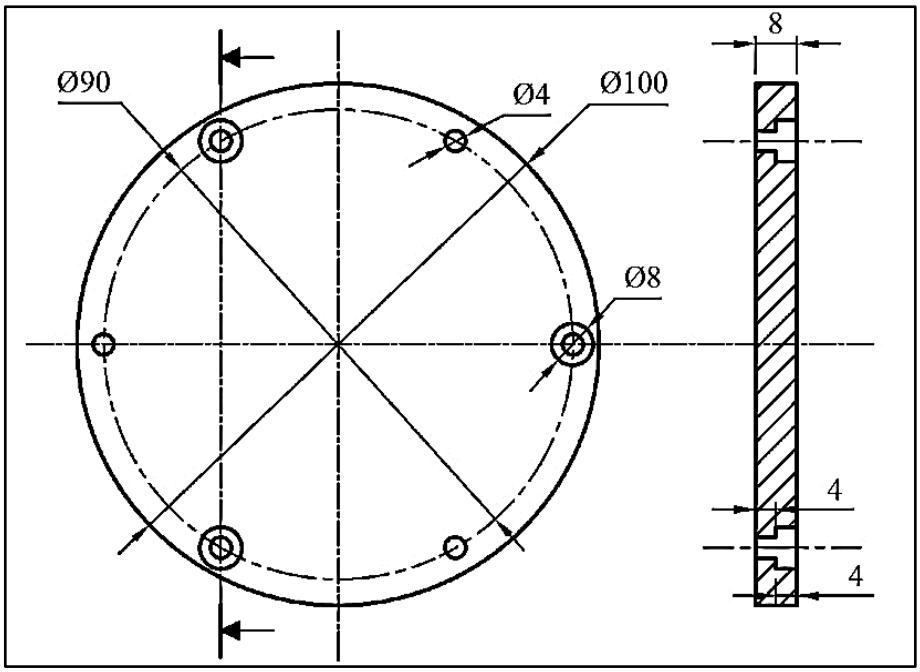

Fig. 7.2 Drawing of disc specimen

Fig. 7.3 Disc specimen

7.2.2 Selection of wear parameters

The wear parameters and their levels are chosen from the literature study and by considering the limitation of the tribometer's parameters to be used for the test. The sliding distance is kept as 3000m deliberately in all tests. The levels for load, sliding velocity and temperature are selected as double the previous one deliberately with the motive to minimize the number of tests and maximize the variation in the selection of levels. The highest level of temperature is selected as 240°C because the maximum temperature reaches approximately 190°C in an automotive disc brake with intermittent brake loads (Talati & Jalalifar, 2009). The highest level of load and sliding velocity are restricted due to tribometer limitations. The finally selected wear test parameters and the levels chosen are given in Table 7.2

Table 7.2 Wear test parameters

Sr. no.	Wear test parameters	Levels			
		1	2	3	4
1	Load, F (N)	20	40	80	160
2	Sliding Velocity, ν (m/s)	1.1	2.2	4.4	8.8
3	Temperature, T (°C)	30	60	120	240

7.2.3 Selection of design of experiment

The design of experiments is an important stage in conducting a series of experiments. It helps in reducing the repetition of experiments and in optimizing the number of experiments to be performed. Ideally, $4^3 = 64$ experiments need to be performed for each melt, where '4' is the level number and '3' represents the wear parameters selected for the wear test. Numerous methods are available for optimizing the number of experiments. In the present study, based on a rigorous study of available literature, the Taguchi L_{16} array is selected for optimizing the total number of experiments which reduces the number of

experiments from 64 to 16 only and the design of the experiment based on Taguchi L_{16} array is given in Table 7.3.

Table 7.3 Design of experiment

/ Test No.	Parameters		
	Load, F (N)	Sliding Velocity, ν (m/s)	Temperature, T (°C)
1	20	1.1	30
2	20	2.2	60
3	20	4.4	120
4	20	8.8	240
5	40	1.1	60
6	40	2.2	30
7	40	4.4	240
8	40	8.8	120
9	80	1.1	120
10	80	2.2	240
11	80	4.4	30
12	80	8.8	60
13	160	1.1	240
14	160	2.2	120
15	160	4.4	60
16	160	8.8	30

7.2.4 Wear test

The wear experiments are conducted as per ASTM standard G99-17 on a temperature-controlled rotary tribometer setup (Make: Ducom) with a complete data acquisition system as shown in Fig. 7.4.

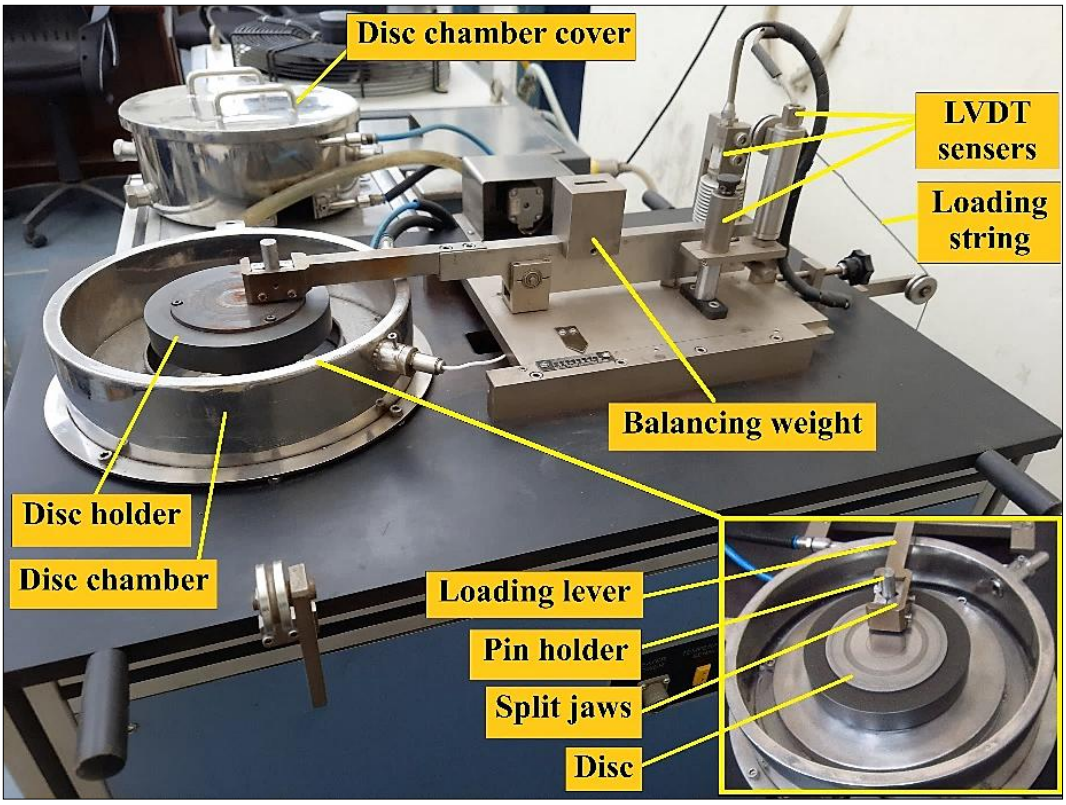

Fig. 7.4 Experimental set-up for pin-on-disc wear test

The disc is fixed on the disc holder. The pin is also fixed in the jaws of the tribometer pin holder at the specified track radius. The requisite weight is placed in the load hanger and the balancing weight is adjusted on the loading lever. The LVDT sensors are also adjusted to the 'zero position'. The formal trial run-in sliding wear of 2-3 minutes is done before the start of the actual test to remove unevenness/debris from the surface of the disc and the pin in contact. The disc and pin are cleaned initially and after each trial run-in using acetone. The disc and pin are weighed separately on a digital scale (least count 0.1 mg) and noted accordingly before and after every test. The initial values of friction force, wear and coefficient of friction value are reset to zero. The requisite wear parameters are

fed into the data acquisition system of the tribometer. After switching on the tribometer, the disc chamber is allowed to gain the desired temperature fed in the data acquisition system before the start of the wear test. The change in different parameters like frictional force, coefficient of friction, wear and temperature due to the rubbing action of the pin over the disc are visualized on the screen and recorded continuously. After every test, the disc and the pin surfaces are cleaned before the final weight measurement.

7.2.5 Optimization of wear parameters

After conducting the pin-on-disc wear test, optimization of wear parameters is an essential step to analyze the material behavior concerning the wear parameters. For this, the data obtained from the tribometer is processed in MINITAB software for the melt which has lesser specific wear rate and higher coefficient of friction among the three melts.

7.2.6 Microstructural analysis of wear surface

Scanning electron microscopy (SEM) and Energy dispersive x-ray microanalysis (EdX) is carried out on the wear surface of the tested specimens after the wear test using Zeiss EVO 50 microscope with Bruker EdX (Quantax 200) attachment. The tested specimens having the wear surfaces are cut into the size of 20×10mm for SEM and EdX analysis. These specimens are cleaned in the acetone solution and dried to ensure all the surfaces are free from moisture, debris, grease, oil, etc. These cleaned and dried specimens are placed on the pallet (Φ50mm) inside the vacuum chamber designed to have a vacuum of 10^{-4} mbar. The microscopic examination is done at different analytical working distances and magnification levels using a beam of electrons with an acceleration voltage of 30 KV. The EdX analysis is done on the same Zeiss EVO50 microscope using Bruker's Quantax 200 attachment to examine the embedded pin material over the disc's surface.

7.3 Results and discussion

7.3.1 Specific wear rate and coefficient of friction data

The test data obtained from the pin-on-disc wear tests of all the specimens made from Melt-1, Melt-2 and Melt-3 is processed and tabulated in Table 7.4. The coefficient of friction data is directly taken from the sensor's recorded data in tribometer software, while the specific wear rate is calculated using Eq. 7.1 (Stachowiak & Batchelor, 2013).

Specific wear rate, $k = \frac{V}{F*d}$ $\mu m^3/_{Nm}$ Eq. (7.1)

where,

V- Wear volume, μm^3

F –Load applied, N

d –Sliding distance, m

Table 7.4 Experimental data

Test No.	Experimental data					
	Melt-1		Melt-2		Melt-3	
	Specific wear rate, k (μm^3/Nm)	Coefficient of friction, μ	Specific wear rate, k (μm^3/Nm)	Coefficient of friction, μ	Specific wear rate, k (μm^3/Nm)	Coefficient of friction, μ
1	663.8	0.4474	675.75	0.4434	683.75	0.4514
2	1012.46	0.44565	1030.68	0.4423	984.99	0.4473
3	2212.4	0.4298	2252.23	0.4202	1712.52	0.4394
4	2682.49	0.42915	2730.77	0.4239	2654.98	0.4344
5	819.57	0.4173	834.33	0.3953	804.37	0.4393
6	1003.23	0.4365	1021.09	0.4372	995.62	0.4558
7	2323.1	0.42555	2364.92	0.4153	2123.11	0.4358
8	2765.6	0.4219	2815.38	0.4187	2565.61	0.4251
9	1140.3	0.42365	1160.83	0.417	1090.31	0.4303
10	1741.81	0.40935	1773.16	0.3894	1648.74	0.4293
11	1714.6	0.42865	1745.46	0.4113	1514.68	0.446
12	2185.9	0.42755	2225.25	0.4225	2135.93	0.4326
13	1717.5	0.39335	1748.42	0.3793	1661.56	0.4074
14	1878.4	0.40675	1912.21	0.4033	1627.42	0.4102
15	1853.69	0.4116	1887.06	0.4039	1769.99	0.4193
16	2213.8	0.4078	2253.65	0.3996	2174.21	0.416

After rigorous analysis of the data obtained from the pin-on-disc test, plotted in Fig.7.5 and Fig.7.6, it is observed that overall Melt-3 has a lesser specific wear rate and good coefficient of friction among the three melts. On observing Fig. 7.5, for the comparison of

specific wear rate data, the lowest value of specific wear rate is observed in test no.1 while test no. 8 shows the highest specific wear rate. From Table 7.4, it is revealed that test '1' represents the lowest level of wear parameters (20N load, 1.1m/s sliding velocity and room temperature 30℃) while test '8' represents the combination of 40N load (level 1), the sliding velocity of 8.8m/s (level 4) alongwith 120℃ (level 3) of the disc temperature. From the test results of all the tests, it is observed that Melt-3 samples have a lesser specific wear rate followed by Melt-1 and Melt-2 respectively. This may be happening due to the presence of a higher percentage of carbide former elements in the Melt-3, as compared to other melts, which results in higher surface hardness of the wear discs. Also, from these results, it may be concluded that sliding velocity is the prime factor for higher specific wear rates.

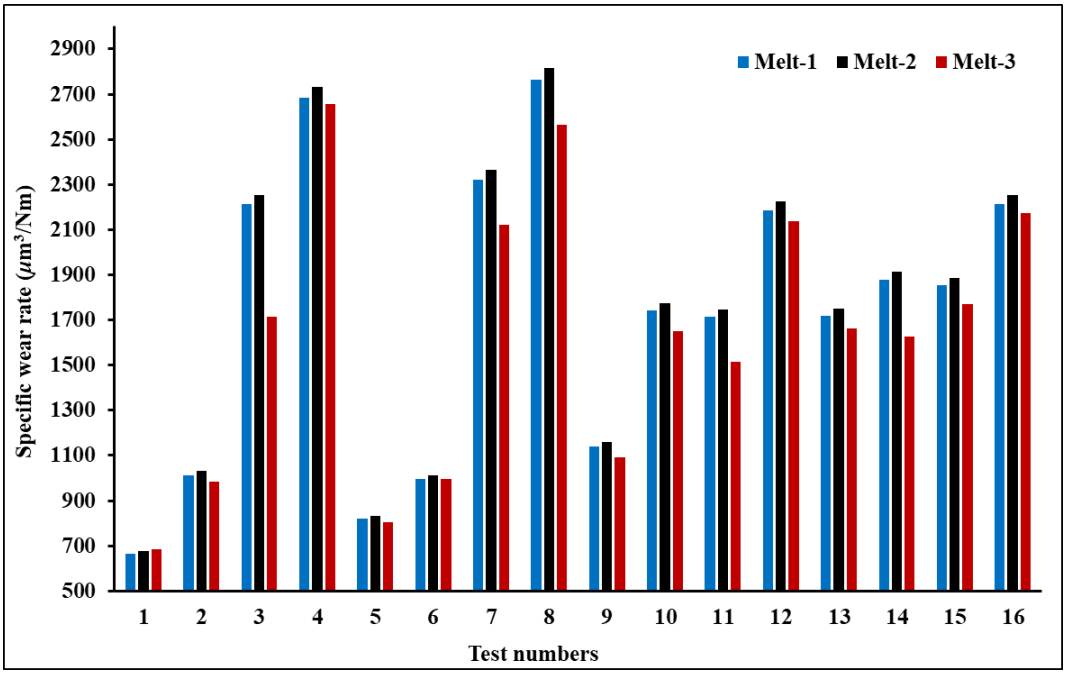

Fig. 7.5 Specific wear rate data

Similarly, Fig.7.6 depicts the coefficient of friction values of the three melts in all the 16 tests performed as per the Taguchi L_{16} array. On observing Fig. 7.6, test '6' reflects the highest value of the coefficient of friction for Melt-3 followed by Melt-1 and Melt-2 in test '1'. Test '6' comprises of 40N Load (level 2), 2.2m/s (level 2) at room temperature

(level 1). From these results for the coefficient of friction, one may imagine that load and sliding velocity have a great influence on the coefficient of friction of Melt-1 and Melt-2 and slightly lesser on Melt-3 due to the presence of higher amounts of Mo, Cr, Cu and Si as compared to rest of the melts. An increase in the values of load and sliding velocity results in a lower coefficient of friction.

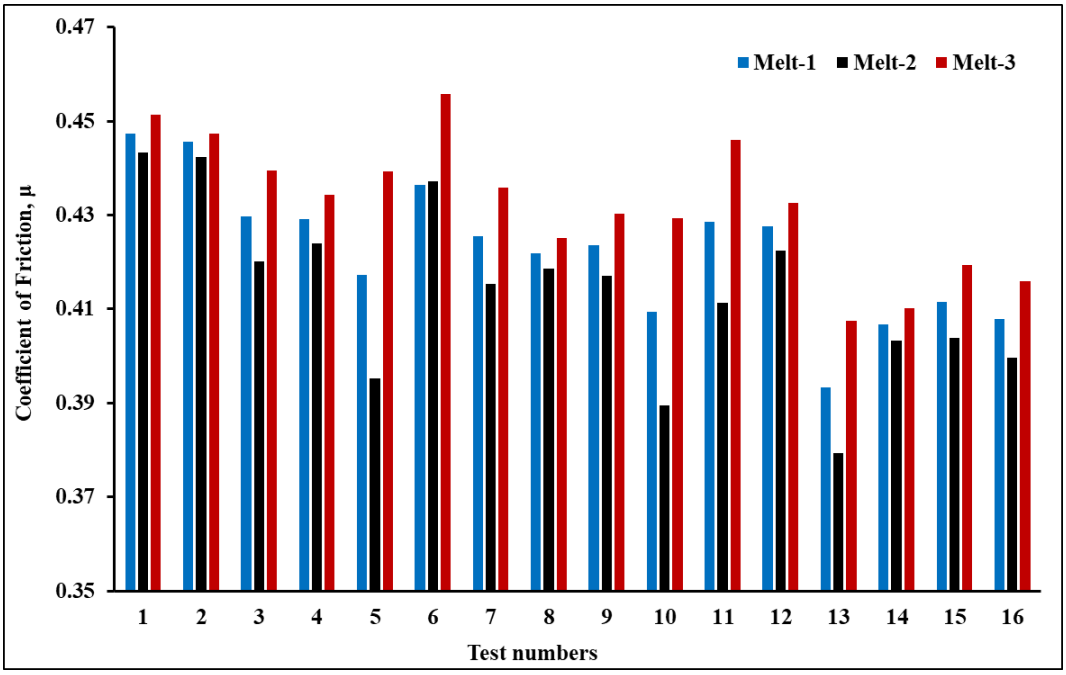

Fig. 7.6 Coefficient of friction data

The detailed analysis of this data is further done to study the behavior of the three melts based on the disc temperature in the form of graphs plotted in Fig. 7.7 to Fig. 7.10 for both disc's specific wear rate and coefficient of friction separately. The results of the disc's specific wear rate and the coefficient of friction are found to be in the same line as given in the literature. The specific wear rate increases with the increase in load, sliding velocity and temperature. Similarly, the coefficient of friction is found to be decreasing with the increase in either of the wear parameters i.e., load, sliding velocity and disc temperature. From the keen study of these plots, it is revealed that the sliding velocity and disc temperature seem more responsible for the variations in specific wear rate and coefficient of friction. It is also seen that the behaviour of the three melts is almost similar

at combinations of the least levels of the wear parameters. In Fig. 7.7 (a, b), at room temperature, Melt-3 reveals the lowest specific wear rate and the highest coefficient of friction among the three melts. An inversely linear relation is observed for the coefficient of friction with the increase in load and sliding velocity at room temperature while Melt-3 shows the higher coefficient of friction at 40N load and 2.2m/s sliding velocity.

Similarly, Fig. 7.8-7.10 display the impact of load and sliding velocity at various temperature levels on the melt's wear behaviour. At 60℃ temperature, Fig. 7.8 reveals that the specific wear rate is found lower in Melt-3 at 40N load, 1.1m/s sliding velocity and higher coefficient of friction at 20N load, 2.2m/s sliding velocity. At 120℃ temperature, Fig. 7.9 reveals that the specific wear rate of Melt-3 is found lower at 80N load, 1.1m/s sliding velocity and higher coefficient of friction at 20N load, 4.4m/s sliding velocity. At 240℃ temperature, Fig. 7.10 reveals that the specific wear rate of Melt-3 is found lower at 80N load, 2.2m/s sliding velocity and higher coefficient of friction at 40N load, 4.4m/s sliding velocity.

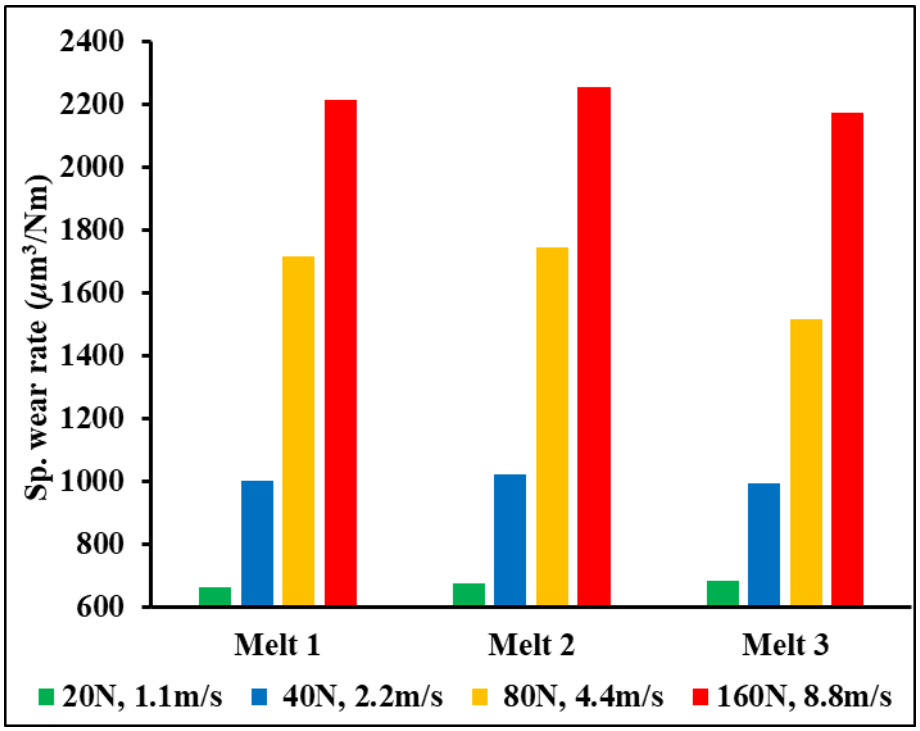

(a) Comparison of melt's specific wear rate

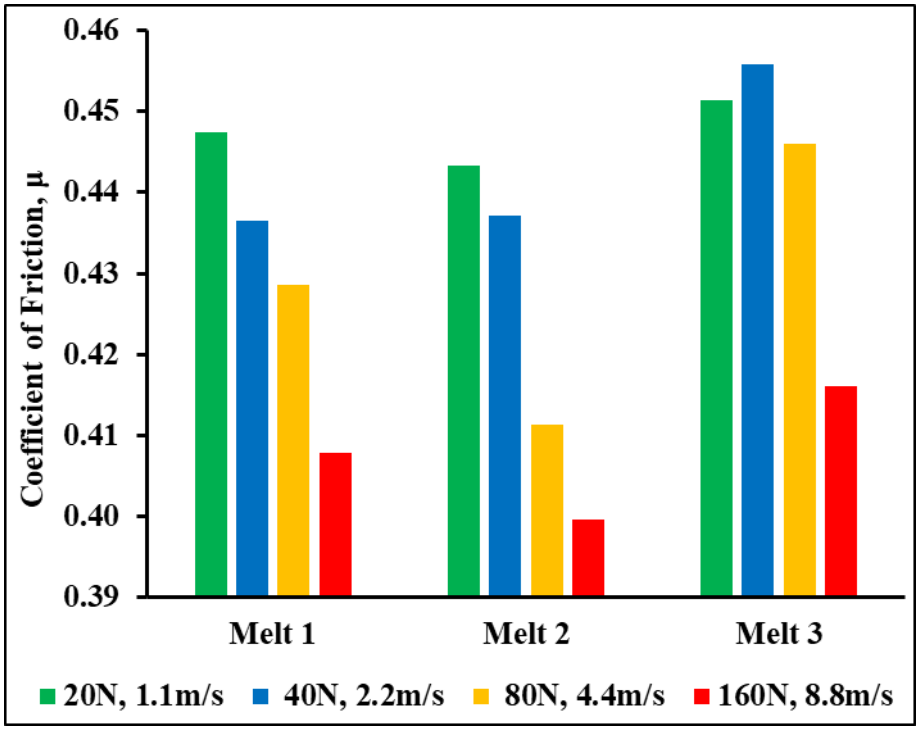

(b) Comparison of melt's coefficient of friction

Fig. 7.7 Comparison of Melt's specific wear rate and coefficient of friction at 30℃

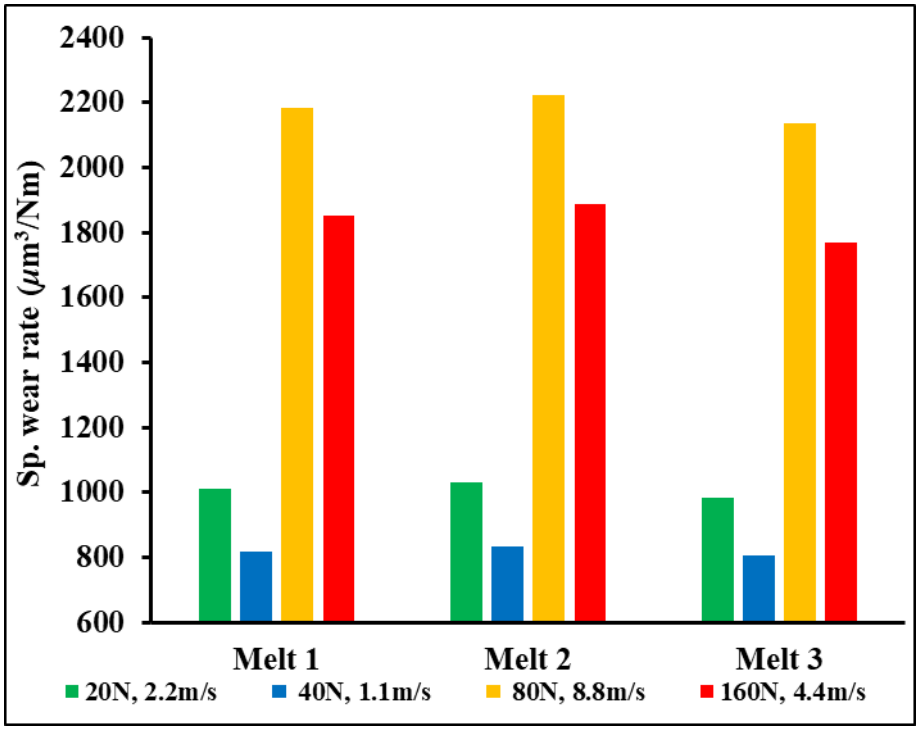

(a) Comparison of melt's specific wear rate

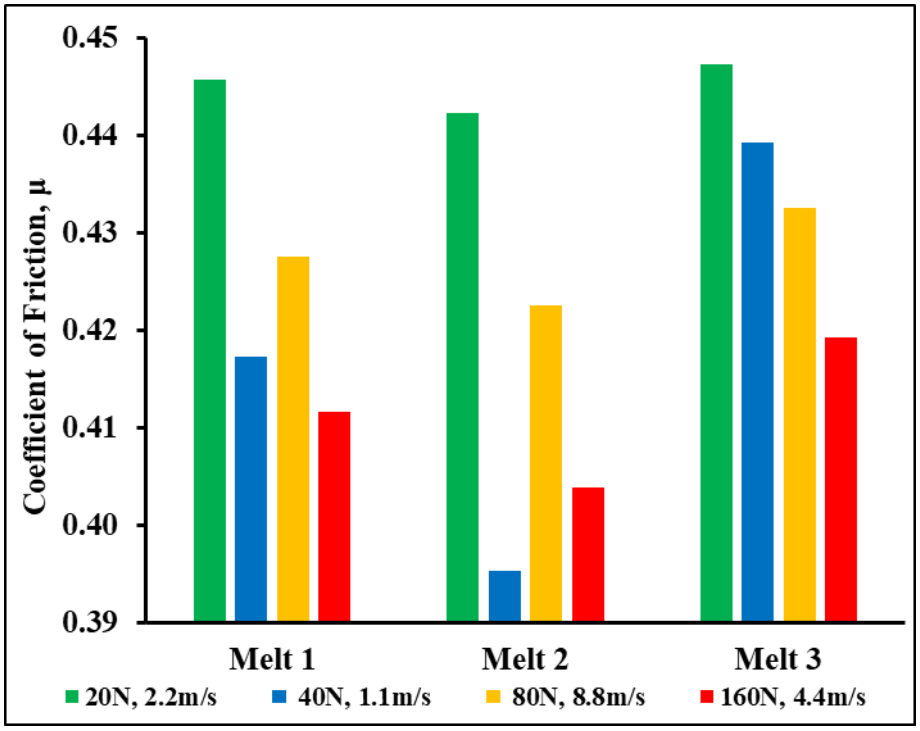

(b) Comparison of melt's coefficient of friction

Fig. 7.8 Comparison of Melt's specific wear rate and coefficient of friction at 60℃

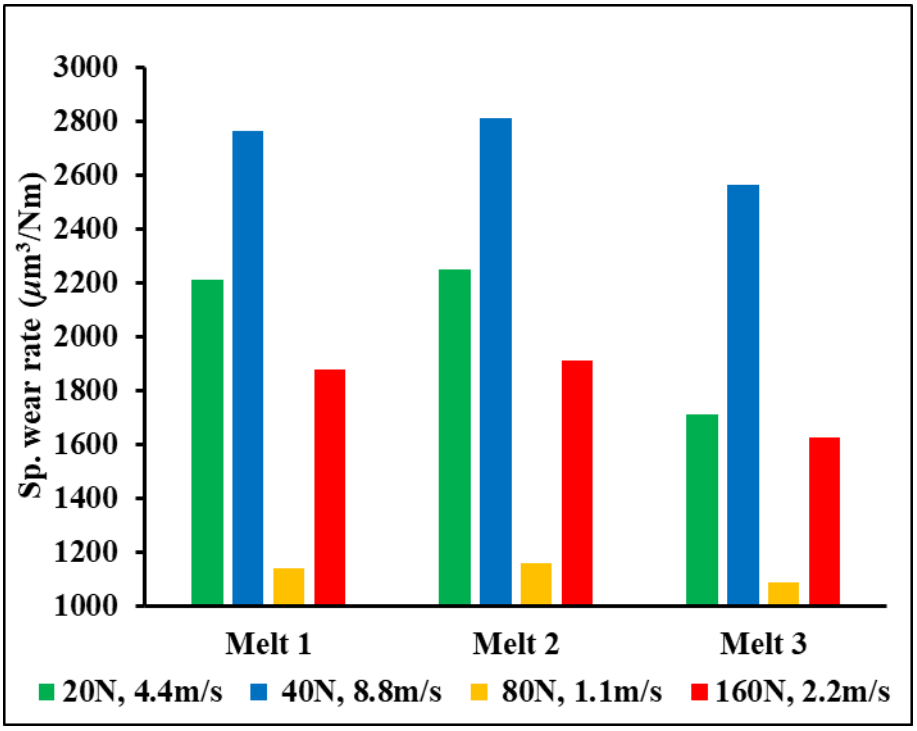

(a) Comparison of melt's specific wear rate

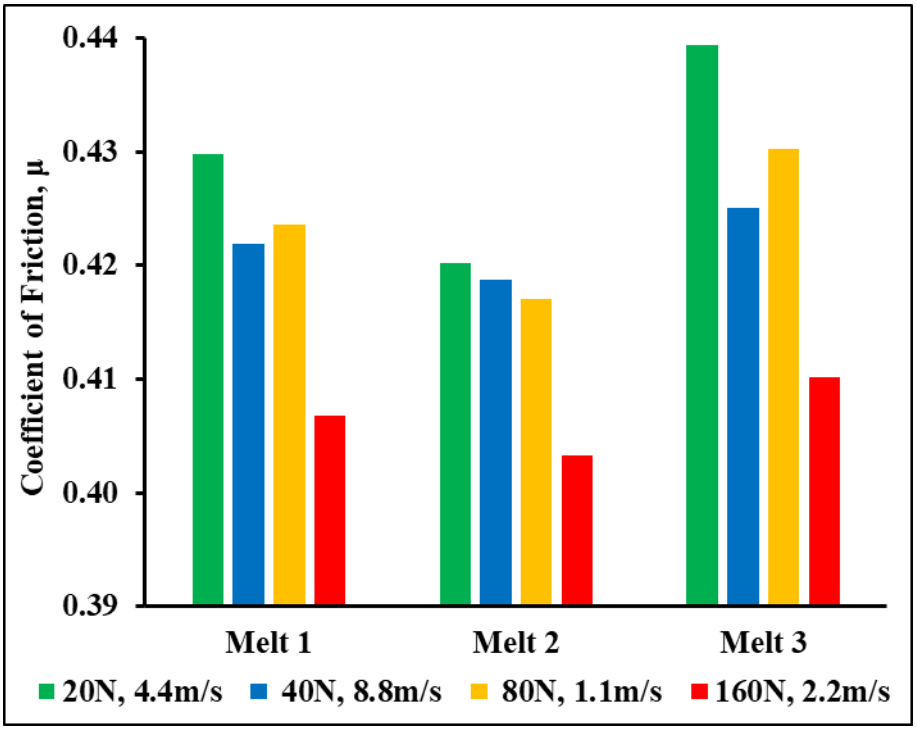

(b) Comparison of melt's coefficient of friction

Fig. 7.9 Comparison of Melt's specific wear rate and coefficient of friction at 120℃

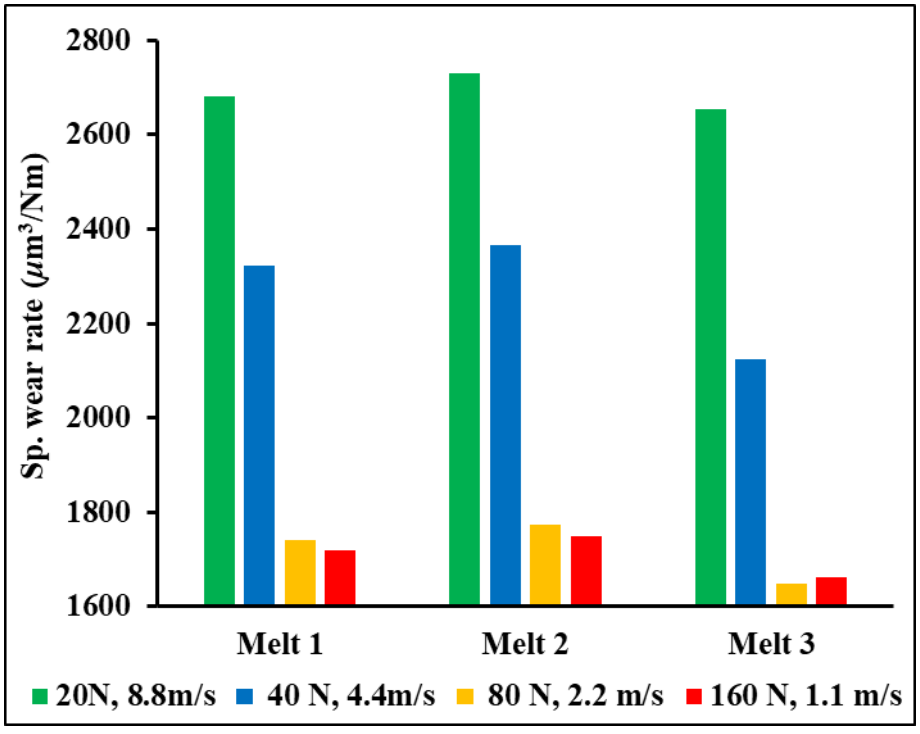

(a) Comparison of melt's specific wear rate

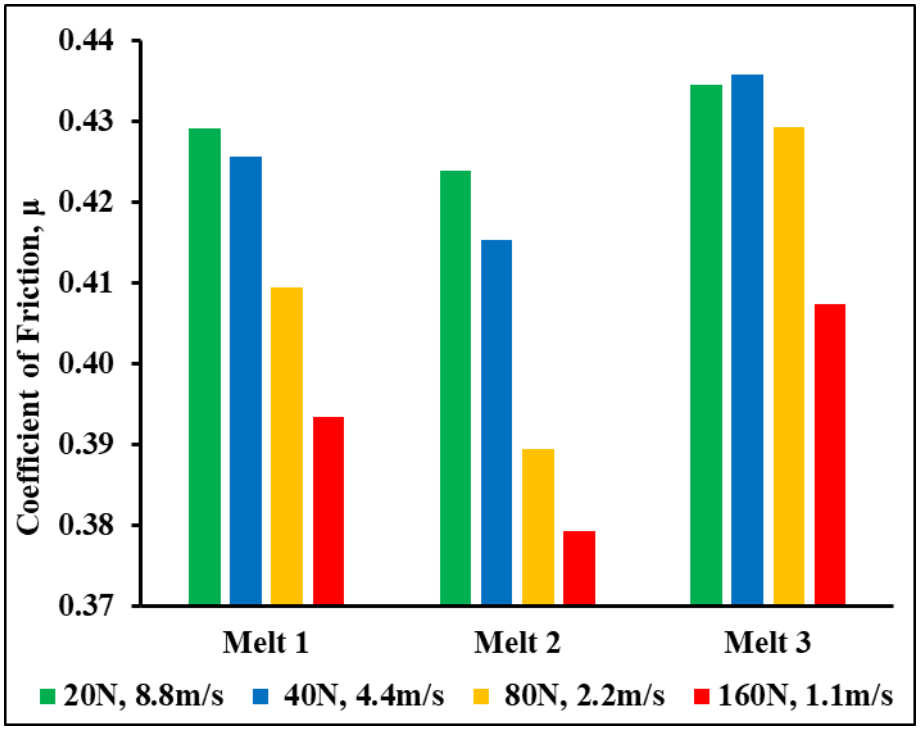

(b) Comparison of melt's coefficient of friction

Fig. 7.10 Comparison of Melt's specific wear rate and coefficient of friction at 240℃

Overall, it is concluded that Melt-3 of SiMoCr DCI, having a higher percentage of Mo, Cr, Cu and Si, has a lower specific wear rate and higher coefficient of friction in comparison with Melt-1 and Melt-2.

Therefore, based on the above discussion and results only the wear data of Melt-3 is further processed for optimizing the wear parameters for lower specific wear rate and higher coefficient of friction.

7.3.2 Optimizing the wear behaviour of Melt-3

Optimization means the selection of input parameters for better output. The requisite output value may be smaller, nominal, or higher. The design analysis uses the signal-to-noise (S/N) ratio responses for optimizing the wear behaviour of the SiMoCr ductile cast iron, proposed by Taguchi (1987). The 'signal (S)' is the required data while the 'noise (N)' is the unwanted data and the ratio of these two is termed as S/N ratio which expresses the scattering of obtained data around the requisite data.

From the results obtained from the pin-on-disc tests, it is found that Melt-3 has a lesser specific wear rate and higher coefficient of friction among the three melts. For optimizing the wear behaviour of the SiMoCr DCI, Melt-3's pin-on-disc wear results are considered and processed further using MINITAB statistical software to optimize the wear behaviour of the material so developed.

7.3.2.1 Taguchi design analysis for optimizing the wear behaviour

Taguchi categorized the S/N ratio as 'smaller the better', 'nominal the better' and 'higher the better' categories and proposed the following equations for each category.

$$\text{Smaller the better} = -10*\log(\Sigma(Y^2)/n \quad \text{Eq. (7.2)}$$

$$\text{Nominal the better} = 10*\log((Y^2)/\sigma^2) \quad \text{Eq. (7.3)}$$

$$\text{Larger the better} = -10*\log(\Sigma(1/Y^2)/n) \quad \text{Eq. (7.4)}$$

Where in each factor level combination,

Y is responses,

N is the number of responses and

σ is the standard deviation of the responses for all noise factors.

The aim of the present study is to minimize the specific wear rate and maximize the coefficient of friction of the SiMoCr DCI Melt-3. Therefore, Eq.7.2 and Eq.7.4 are selected for lower specific wear rate '*k*' and higher coefficient of friction *'μ'* respectively. The S/N ratios for specific wear rate and coefficient of friction of SiMoCr DCI Melt-3 are calculated using Eq. 7.2 and 7.4 and tabulated in Table 7.5.

Table 7.5 S/N ratio data for Melt-3

Test No.	Experimental results		S/N ratio	
	Specific wear rate, k (μm3/Nm)	Coefficient of friction, μ	Specific wear rate, *k* (dB)	Coefficient of friction, μ (dB)
1	683.75	0.4514	-56.6979	-6.9088
2	984.99	0.4473	-59.8687	-6.988
3	1712.52	0.4394	-64.6727	-7.1428
4	2654.98	0.4344	-68.4812	-7.2422
5	804.37	0.4393	-58.1091	-7.1448
6	995.62	0.4558	-59.9619	-6.8245
7	2123.11	0.4358	-66.5395	-7.2143
8	2565.61	0.4251	-68.1838	-7.4302
9	1090.31	0.4303	-60.751	-7.3246
10	1648.74	0.4293	-64.343	-7.345
11	1514.68	0.446	-63.6064	-7.0133
12	2135.93	0.4326	-66.5917	-7.2783
13	1661.56	0.4074	-64.4103	-7.7996
14	1627.42	0.4102	-64.23	-7.74
15	1769.99	0.4193	-64.9594	-7.55
16	2174.21	0.416	-66.746	-7.6181

7.3.2.2 Effect of wear parameters on specific wear rate and coefficient of friction

Fig. 7.11 shows that the specific wear rate ‘k’ increases with the increase in applied load, sliding velocity and temperature. From Fig. 7.12, it is found that the coefficient of friction ‘μ’ is higher at lower loads and as the load increases, it decreases slightly.

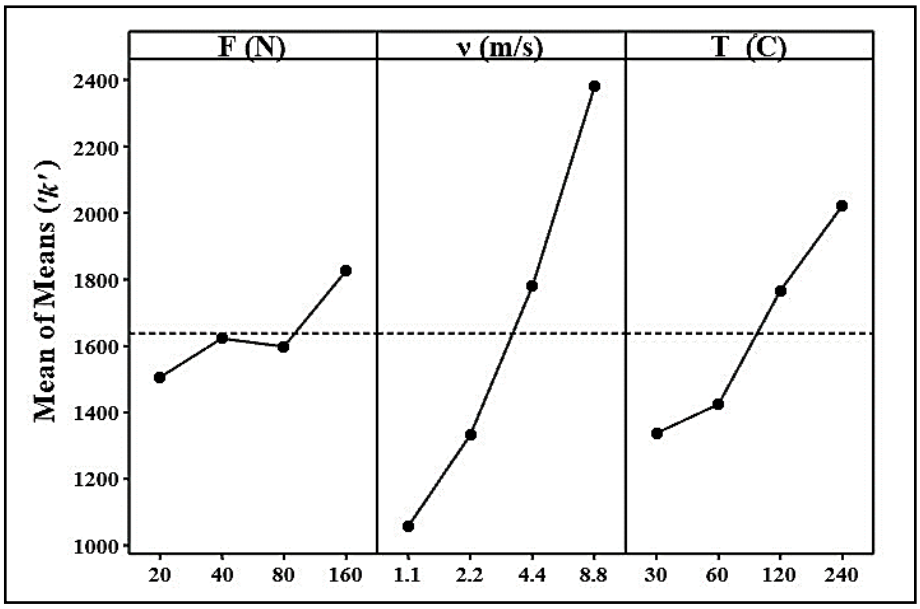

Fig. 7.11 Effect of wear parameters on specific wear rate *'k'*

In the initial stage, it is observed that as the load is applied, the surface contact area between the pin and the disc is significantly less due to the contact between surface peaks only. As the test progresses, the surface peaks are worn off and converted into wear debris, increasing the contact surface area. These wear debris roll over the disc surface in the pin contact area, reducing the specific wear rate '*k*' and *'μ'* as well as increasing the surface temperature of the disc due to rubbing action, The 'specific wear rate '*k*' remains almost constant when the load varies from 40 N to 80 N. This may be attributed to wear debris that revolves over and along the disc under the pin contact region. At initial sliding velocity, the rubbing surfaces of the pin and disc are fine enough and start deteriorating with time with the increase in the sliding friction due to load and temperature. This increase in sliding friction results in the thermal softening of the surface material of the disc, which further helps in the kick-off of the surface molecules from the disc surface and results in surface wear. Such molecules get piled up to form wear debris lumps. These wear lumps run over and along the disc surface in the pin contact area and further help in enhancing the surface wear rate by increasing the separation rate of more

molecules from the disc surface and the pin surface. These debris lumps with sufficient mass intermittently runoff from the disc surface due to centrifugal forces.

The varying trend in coefficient of friction 'μ' values with an increase in sliding velocity is also depicted in Fig. 7.12. The variation may be attributed to the variation in sliding friction, debris lumps and temperature. It is observed that *'μ'* initially increases with an increase in sliding velocity and then remains almost constant. After this, the *'μ'* decreases with the increase in the sliding velocity. This decrease in *'μ'* may be attributed to the stick and slip phenomenon of the rubbing surfaces. The *'μ'* value decreases as the temperature rises to 120°C and, after that, increases a little bit and remains almost constant. It indicates that the effect of temperature ceases to affect the value of *'μ'* and could be attributed to the thermal softening of the contacting surfaces.

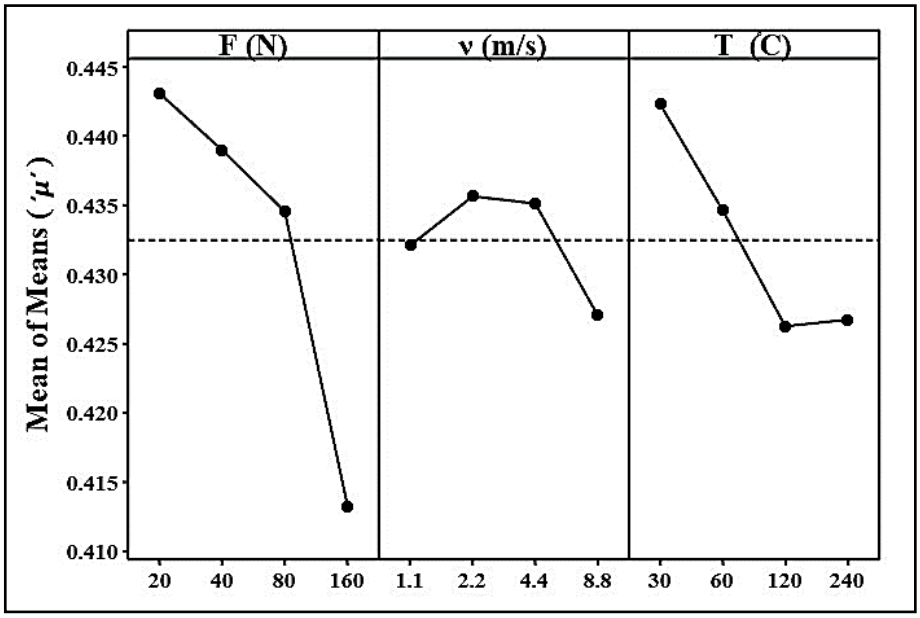

Fig. 7.12 Effect of wear parameters on coefficient of friction *'μ'*

7.3.2.3 'Selection of optimum wear behaviour conditions for '*k*' and *'μ'*

A higher value of the S/N ratio depicts the minimum variation among the desired output and the measured output. Based on a higher S/N ratio, the predicted optimum process parameters for the least specific wear rate '*k*' are observed at 20 N, 1.1 m/s and 30°C,

while for the higher coefficient of friction *'μ'*, is observed at 20 N, 2.2 m/s and 30°C. The corresponding level values (F_1-v_1-T_1) for specific wear rate '*k*' are highlighted in Table 7.6 and in Fig. 7.13.

Table 7.6 Mean S/N ratio response for specific wear rate *'k'*

Wear parameters	Mean S/N ratio					
	Level 1	Level 2	Level 3	Level 4	Delta	Rank
Load, F (N)	**-62.43**	-63.2	-63.82	-65.09	2.66	3
Sliding Velocity v (m/s)	**-59.99**	-62.1	-64.94	-67.5	7.51	1
Temperature (℃)	**-61.75**	-62.38	-64.46	-65.94	4.19	2

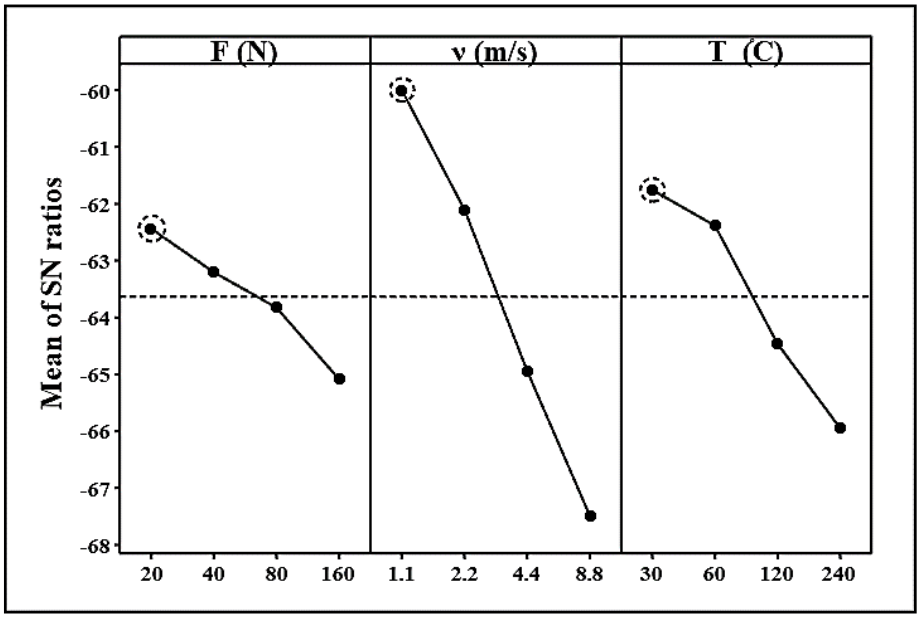

Fig. 7.13 Mean S/N ratio for specific wear rate *'k'*

Similarly, (F_1- v_2-T_1) values are highlighted in Table 7.7 and in Fig. 7.14 for highest coefficient of friction *'μ'*.

Table 7.7 Mean S/N ratio response for coefficient of friction *'μ'*

Wear parameters	Mean S/N ratio					
	Level 1	Level 2	Level 3	Level 4	Delta	Rank
Load, F (N)	**-7.07**	-7.153	-7.24	-7.677	0.606	1
Sliding Velocity, ν (m/s)	-7.294	**-7.224**	-7.23	-7.392	0.168	3
Temperature, T (℃)	**-7.091**	-7.24	-7.409	-7.4	0.318	2

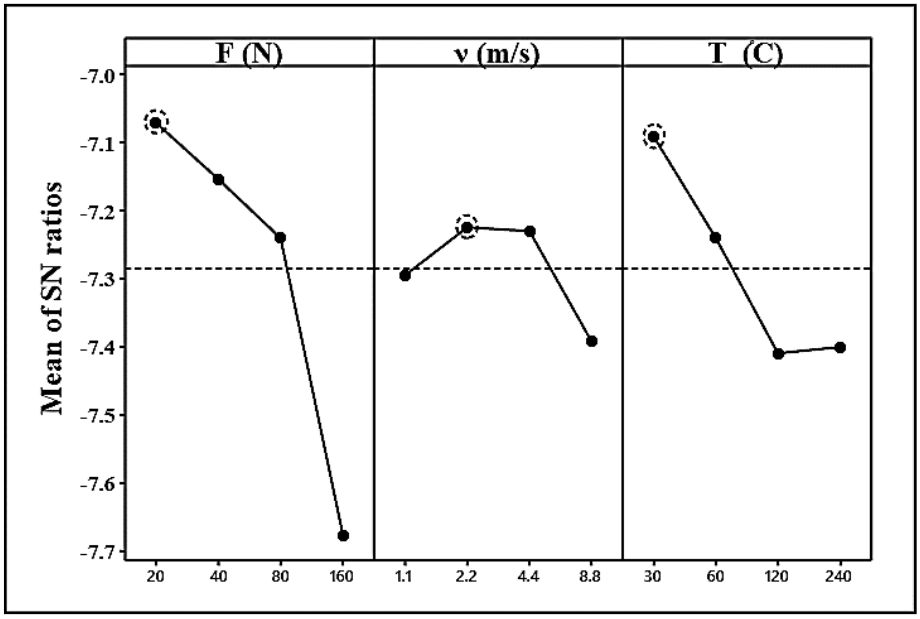

Fig. 7.14 Mean S/N ratio for coefficient of friction *'μ'*

7.3.2.4 Confirmation test

For estimating and verifying the responses at predicted optimum values, the predicted S/N ratio (ε) is used and calculated by using Eq. 7.5 (Sahin & Durak, 2007)

$$\varepsilon_{predicted} = \varepsilon_l + \sum_{i=1}^{x}(\varepsilon_0 - \varepsilon_l) \quad \text{Eq. (7.5)}$$

where,

ε_l Total mean S/N ratio

ε_0 Mean S/N ratio at optimum level

x No of input process parameters

From Tables 7.3 and 7.6, it is found that the test for optimum level parameters (F_1- v_1-T_1) for the least specific wear rate '*k*' has already been performed. Therefore, there is no need to repeat the test. Similarly, as per Tables 7.3 and 7.7, it is found that the confirmation test needs to be performed for the optimum level parameters for the highest 'μ' are found as F_1- v_2-T_1. The results for optimum values of specific wear rate *'k'* and *'μ'* are given in Tables 7.8 and 7.9, respectively. The initial process parameters are chosen as F_1- v_1-T_1 for the least specific wear rate *'k'* and higher *'μ'*. On analyzing Tables 7.8 and 7.9, no change is observed in the specific wear rate *'k'* and *'μ'* at optimal process parameters.

Table 7.8 Mean S/N ratio response of specific wear rate *'k'*

	Initial wear parameters	Optimal wear parameters	
		Prediction	Experimental
Level	F_1- ν_1-T_1	F_1- ν_1-T_1	F_1- ν_1-T_1
S/N ratio (dB)	-56.6979	-56.9062	-56.6979
k (μm^3/Nm)	683.75		683.75

Table 7.9 Mean S/N ratio response of coefficient of friction *'μ'*

	Initial wear parameters	Optimal wear parameters	
		Prediction	Experimental
Level	F_1- ν_1-T_1	F_1- ν_2-T_1	F_1- ν_2-T_1
S/N ratio (dB)	-6.9088	-6.8155	-6.9088
μ	0.4514		0.4514

From the above-mentioned results, it is opined that the Taguchi optimization method significantly optimized the specific wear rate '*k*' and coefficient of friction *'μ'* of the specimens of SiMoCr DCI.

7.3.2.4.1 ANOVA analysis for specific wear rate *'k'* and coefficient of friction *'μ'*

The parameters which affect the specific wear rate *'k'* and coefficient of friction *'μ'* of the material are observed by ANOVA analysis. Table 7.10 and 7.11 shows the analysis of variance results of wear parameters for specific wear rate and coefficient of friction.

Table 7.10 ANOVA response for specific wear rate *'k'*

Source	Degree of freedom	Sum of squares	Mean squares	F-Value	Contribution
Load, F (N)	3	15.137	5.0456	6.8	7.84%
Sliding velocity, ν (m/s)	3	129.131	43.0437	58.01	66.84%
Temperature (°C)	3	44.48	14.8267	19.98	23.02%
Error	6	4.453	0.742		
Total	15	193.201			

Table 7.11 ANOVA response for coefficient of friction *'μ'*

Source	Degree of freedom	Sum of squares	Mean squares	F-Value	Contribution
Load, F (N)	3	0.8755	0.2918	53.05	69.78%
Sliding velocity, ν (m/s)	3	0.0732	0.0244	4.43	5.83%
Temperature (°C)	3	0.2733	0.0911	16.56	21.78%
Error	6	0.0327	0.0055		
Total	15	1.2547			

From these Tables, it is noticed that the specific wear rate is significantly influenced by the sliding velocity while the coefficient of friction is significantly influenced by the

applied load. From ANOVA analysis, it is perceived that load has the least influence on the specific wear rate and the highest on the coefficient of friction and sliding velocity has the least influence on the coefficient of friction and the highest on specific wear rate. The temperature has balanced effects on both specific wear rate and coefficient of friction values.

7.3.2.4.2 Modeling for specific wear rate *'k'* and coefficient of friction 'μ'

To develop the predictive mathematical models for dependent variable parameters of specific wear rate and coefficient of friction as a function of applied load(F), sliding velocity(ν) and temperature(T) respectively, regression analysis is done and limited to first order only. The predictive equations obtained from first-order regression analysis for specific wear rate and coefficient of friction are given in Eq. 7.6 and 7.7 respectively.

$$k = 421.0+(1.906*F) +(169.38* \nu) +(3.303*T) \quad \mathbf{(R^2 = 92.05\%)} \qquad \text{Eq. (7.6)}$$

$$\mu = 0.45932-(0.000212*F) +(0.00855* \nu) -(0.000066*T) \quad \mathbf{(R^2 = 85.84\%)} \qquad \text{Eq. (7.7)}$$

The potentiality of the developed models for specific wear rate and coefficient of friction is checked by the correlation coefficient 'R^2'(Montgomery, 2017). The value of 'R^2' varies from zero to one and the values closer to one indicate a good fit for the developed regression model.

In the present study, the value of 'R^2' for specific wear rate and coefficient of friction are found as 92.05% and 85.84%, respectively. The normal probability plots of residuals for specific wear rate and coefficient of friction are shown in Fig. 7.15 and 7.16, respectively. These residual plots are also validating the developed regression models. The closeness to the straight line of the residual plot indicates the normal distribution of the residual error and correlation coefficient significance.

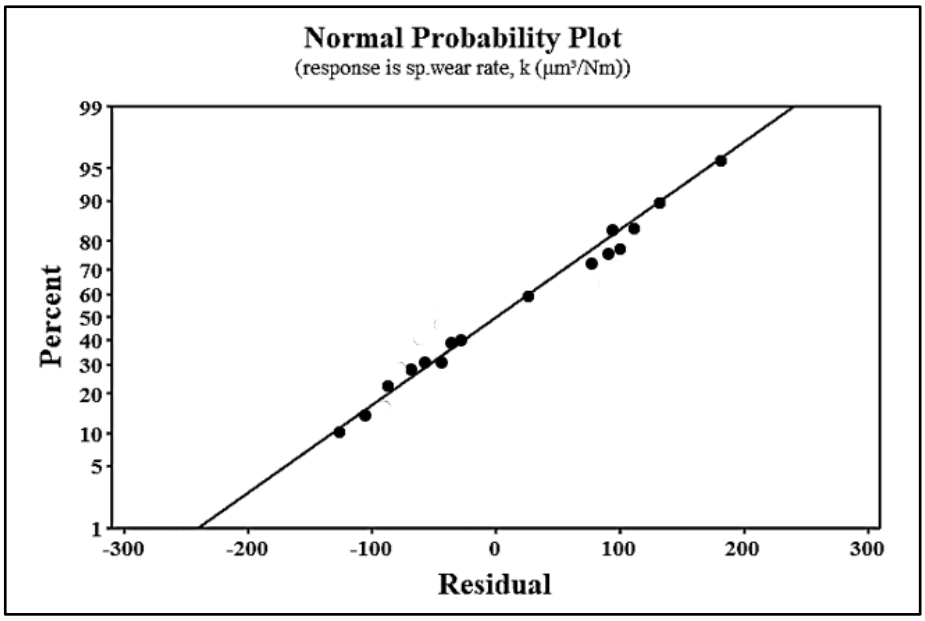

Fig. 7.15 Normal probability plot of the residual of specific wear rate *'k'*

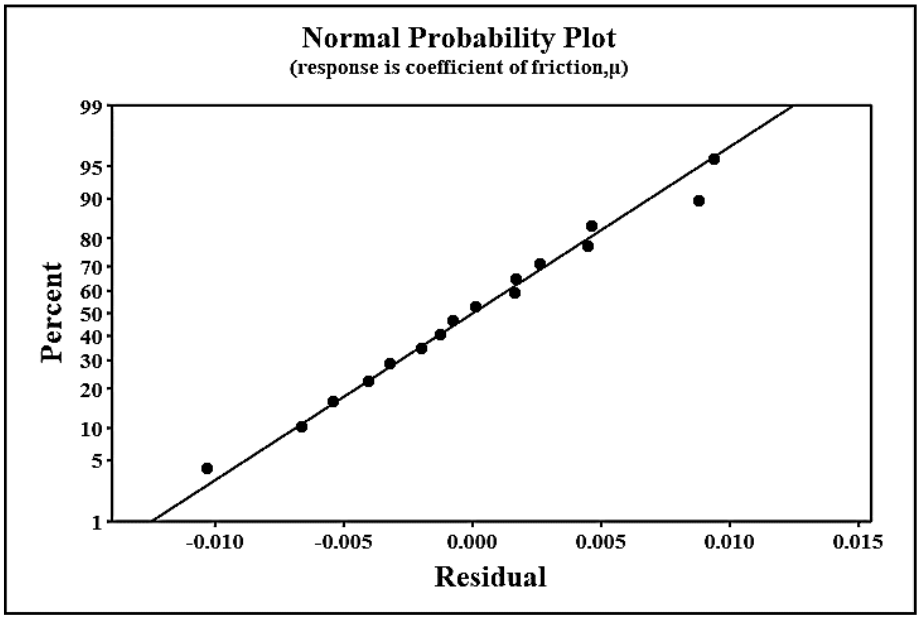

Fig. 7.16 Normal probability plot for the residual of coefficient of friction *'μ'*

The confirmation tests are conducted for the randomly chosen wear test data given in Table 7.4 and the comparison of experimental and predicted results is tabulated in Table 7.12. It is observed that the predicted results and the experimental results are in good agreement. Eq. 7.6 and 7.7 will provide the predicted results at par with the experiment results arbitrarily using any combination of the wear parameters.

Table 7.12 Confirmation results for the developed models

Test No.	Experimental		Predicted		Residual		Error	
	k	μ	k	μ	k	μ	k	μ
2	984.995	0.447	1029.9	0.453	-44.941	-0.0057	4.56	1.27
4	2654.98	0.434	2742.4	0.4468	-87.399	-0.0124	3.29	2.85
6	995.619	0.456	968.97	0.4507	26.6533	0.00506	2.68	1.12
8	2565.61	0.425	2384.1	0.4504	181.465	-0.0253	7.07	5.95
10	1648.74	0.429	1738.8	0.4284	-90.095	0.0009	5.46	0.21
12	2135.93	0.433	2262.2	0.4459	-126.28	-0.0133	5.91	3.07
14	1627.42	0.41	1495	0.4194	132.468	-0.0092	8.14	2.24
16	2174.21	0.416	2315.6	0.4309	-141.39	-0.0149	6.5	3.58

The contour plots given in Fig. 7.17 show the relationship among the wear parameters concerning specific wear rate and coefficient of friction. Contour plots in Fig. 7.17(a,c,e) show the colour scheme, in the form of inclined strips, lighter to dark from lower values to higher values of wear parameters for specific wear rates, while Fig. 7.17(b,d,f) show the colour scheme, in the form of inclined colour strips, darker to light to show the variation in coefficient of friction in respect of wear parameters. The lighter colour shade shown in 7.17(a,c,e) reflects the combination of wear parameters for a minimum specific wear rate. Any combination of wear parameters within the lighter triangle will result in the least specific wear rate.

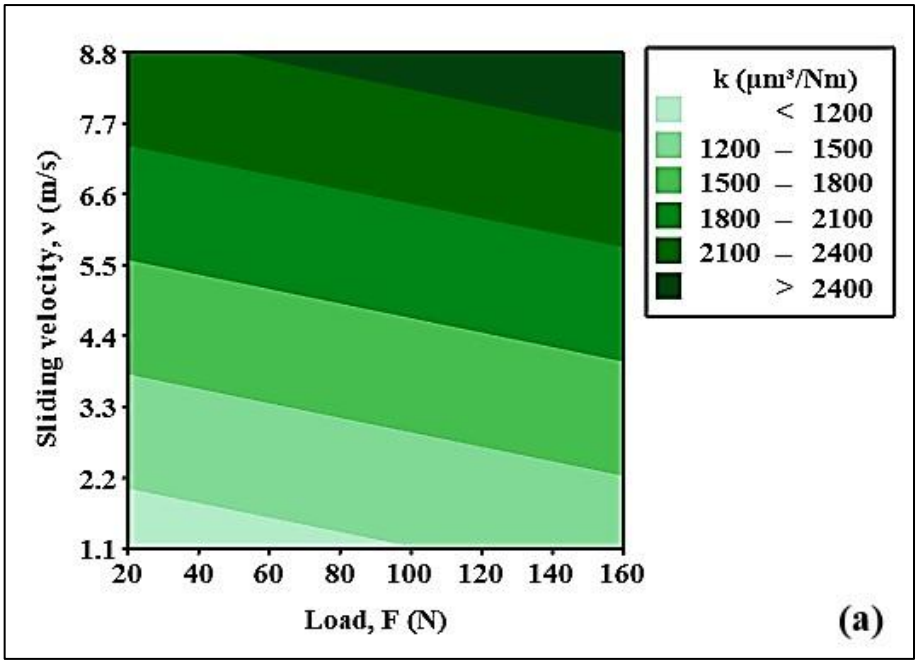
8.8
7.7
6.6
5.5
4.4
3.3
2.2
1.1
Sliding velocity, v (m/s)
20
40
60
80
100
120
140
160
Load, F (N)
k (µm³/Nm)
< 1200
1200 – 1500
1500 – 1800
1800 – 2100
2100 – 2400
> 2400
(a)

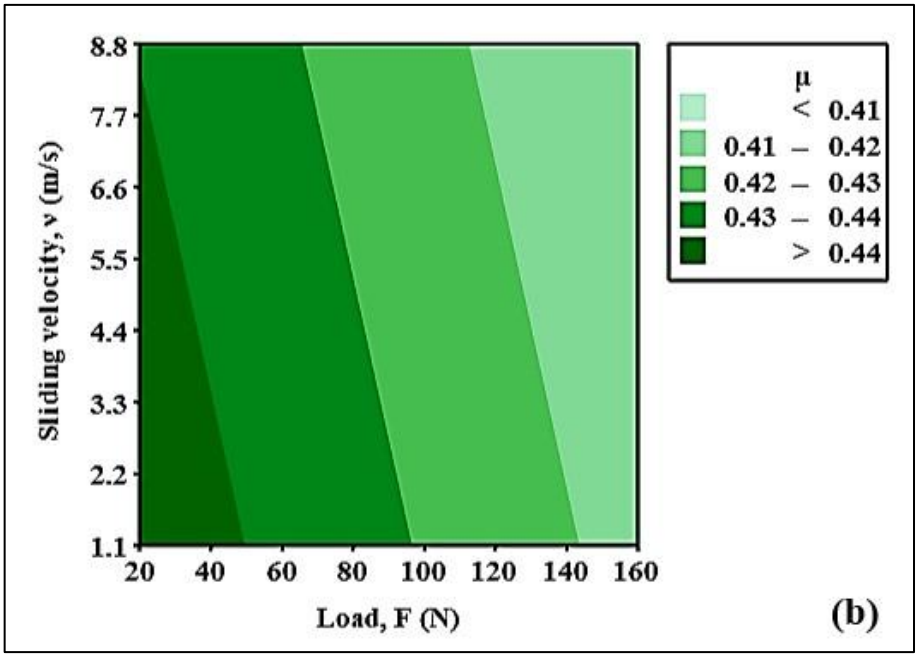
8.8
7.7
6.6
5.5
4.4
3.3
2.2
1.1
Sliding velocity, v (m/s)
20
40
60
80
100
120
140
160
Load, F (N)
µ
< 0.41
0.41 – 0.42
0.42 – 0.43
0.43 – 0.44
> 0.44
(b)

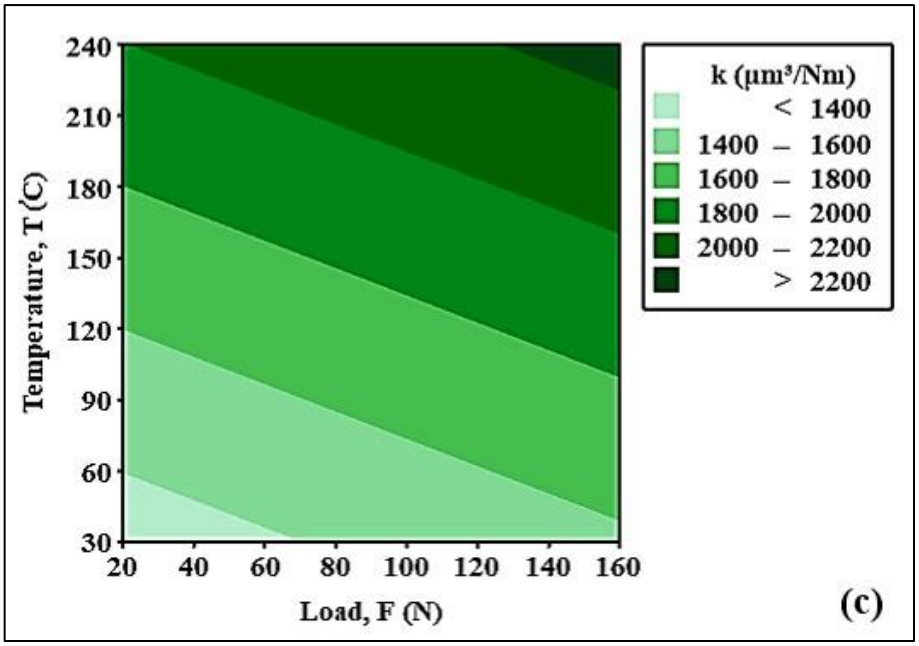
Temperature, T (C)
240
210
180
150
120
90
60
30
20
40
60
80
100
120
140
160
Load, F (N)
k (µm³/Nm)
< 1400
1400 – 1600
1600 – 1800
1800 – 2000
2000 – 2200
> 2200
(c)

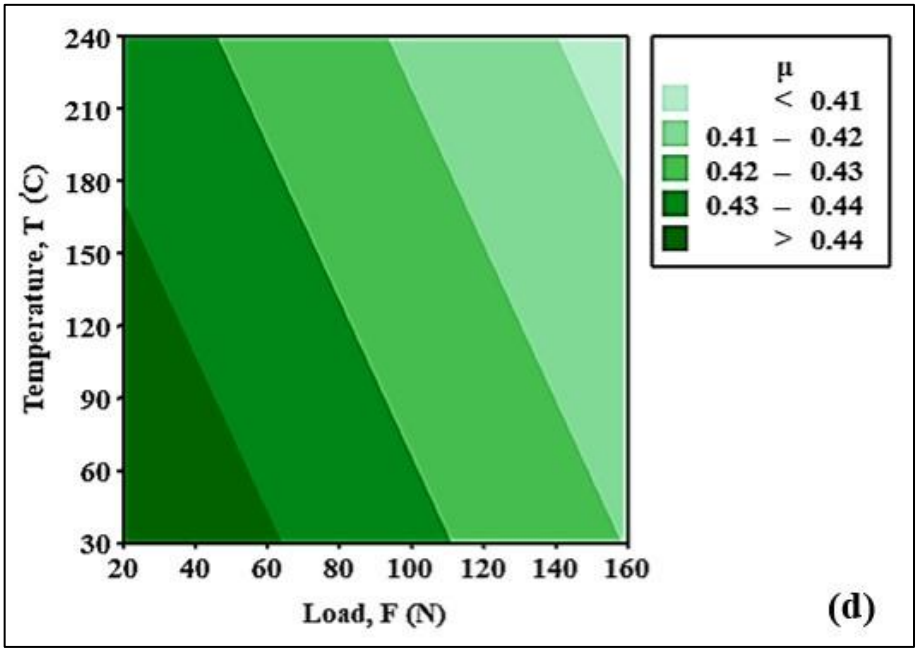
Temperature, T (C)
240
210
180
150
120
90
60
30
20
40
60
80
100
120
140
160
Load, F (N)
µ
< 0.41
0.41 – 0.42
0.42 – 0.43
0.43 – 0.44
> 0.44
(d)

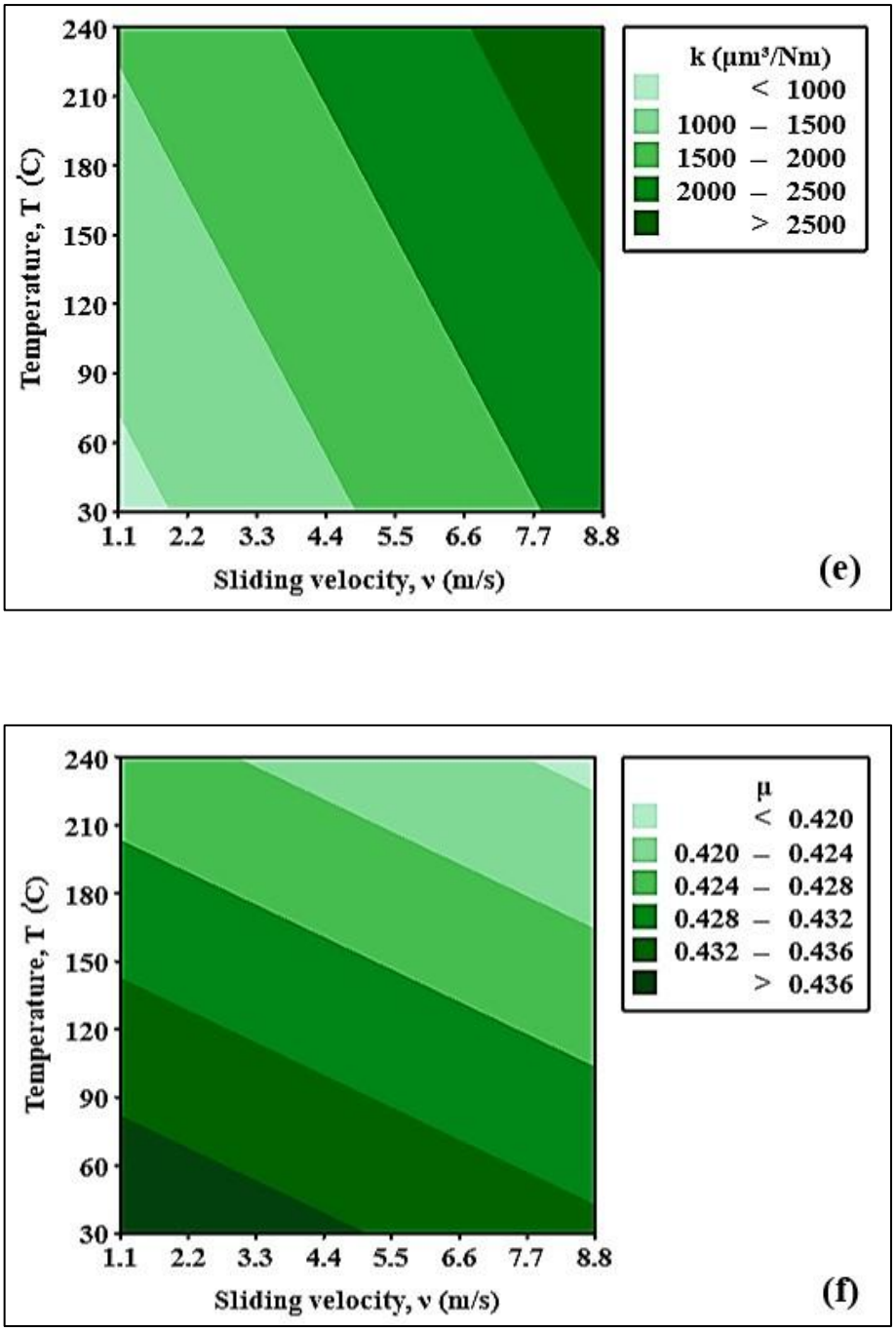

Fig. 7.17 Contour plots for specific wear rate and coefficient of friction

Similarly, The darker colour shade shown in 7.17(a,c,e) reflects the combination of wear parameters for the higher coefficient of friction. Any combination of wear parameters within the darker triangle will result in a higher coefficient of friction. These contour plots are very useful in accessing the response parameters for the different combinations of wear parameters.

7.3.3 SEM and EdX analysis

The representative images of the disc's wear surface, obtained from the SEM, are shown in Fig. 7.18, in which two different micrographs are shown. From Fig. 7.18(a, b), it is observed that the wear debris formed during the sliding of the disc under the loaded pin at a controlled temperature gets lodged onto the surface of the disc forming a wear lump which further helps in accelerating the wear rate of the disc surface. Some wear lumps intermittently move out of the surface contact area between the pin and disc under the influence of centrifugal action, while some debris sticks to the surface of the disk as is evident from Fig. 7.18

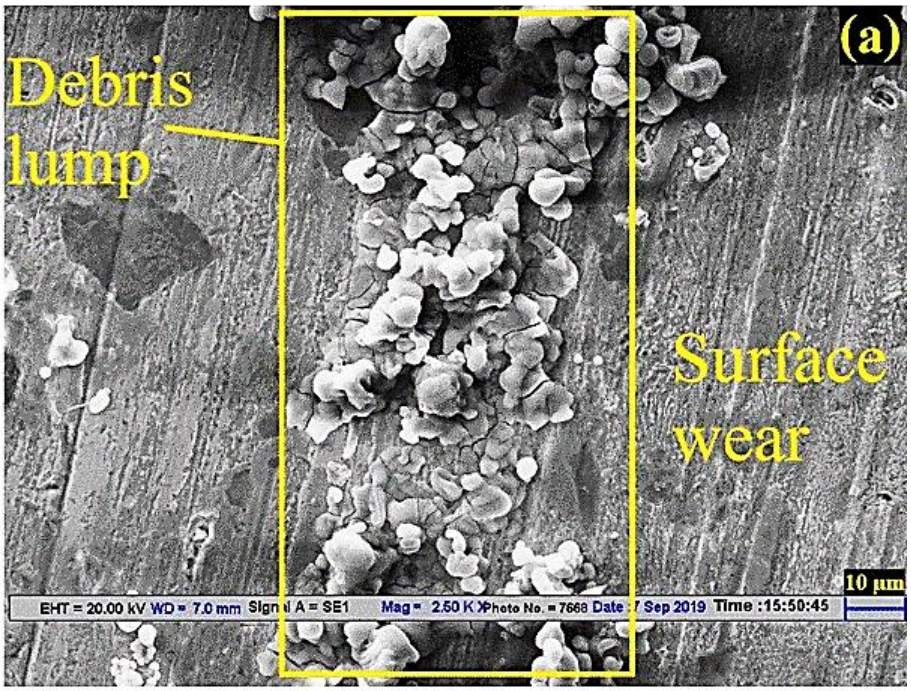

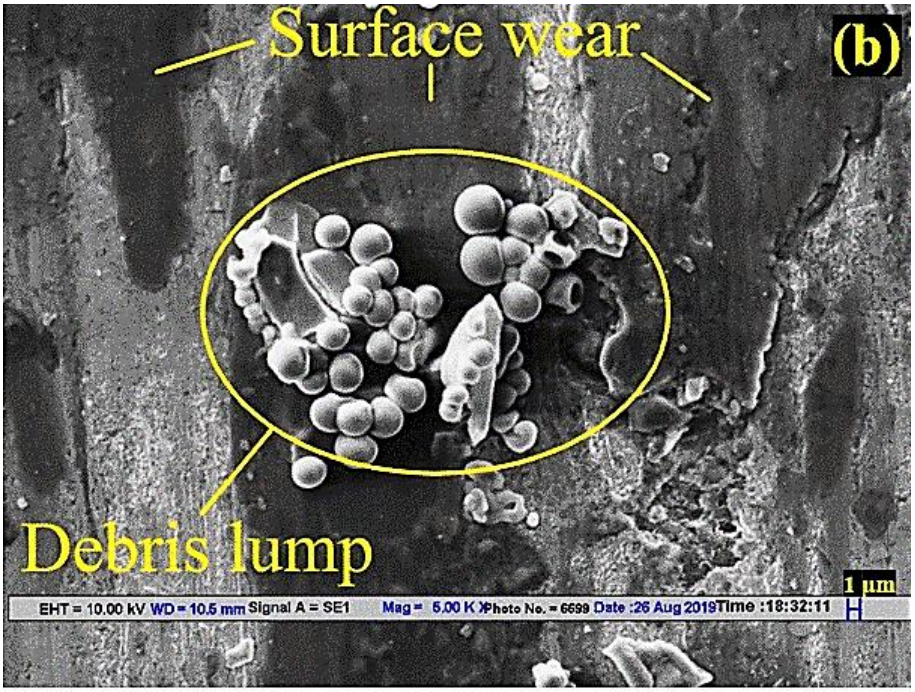

Fig. 7.18 Micrographs of wear surface

On observing Fig. 7.18(a), the wear track traces are visible on the disc surface. The friction material of the pin is also found embedded on the surface. As the friction material is non-conducting in nature, the shadow of the friction material particles is also clearly visible. In Fig. 7.18(b), the chipping-off of the material from the disc surface is visible.

Fig. 7.19 shows the EdX microanalysis of the representative wear surface. Fig. 7.19(a) shows the surface under observation while Fig. 7.19(b) shows the embedded material over the surface of the specimen. The percentage of the embedded microconstituents is given in tabular form in Table 7.13.

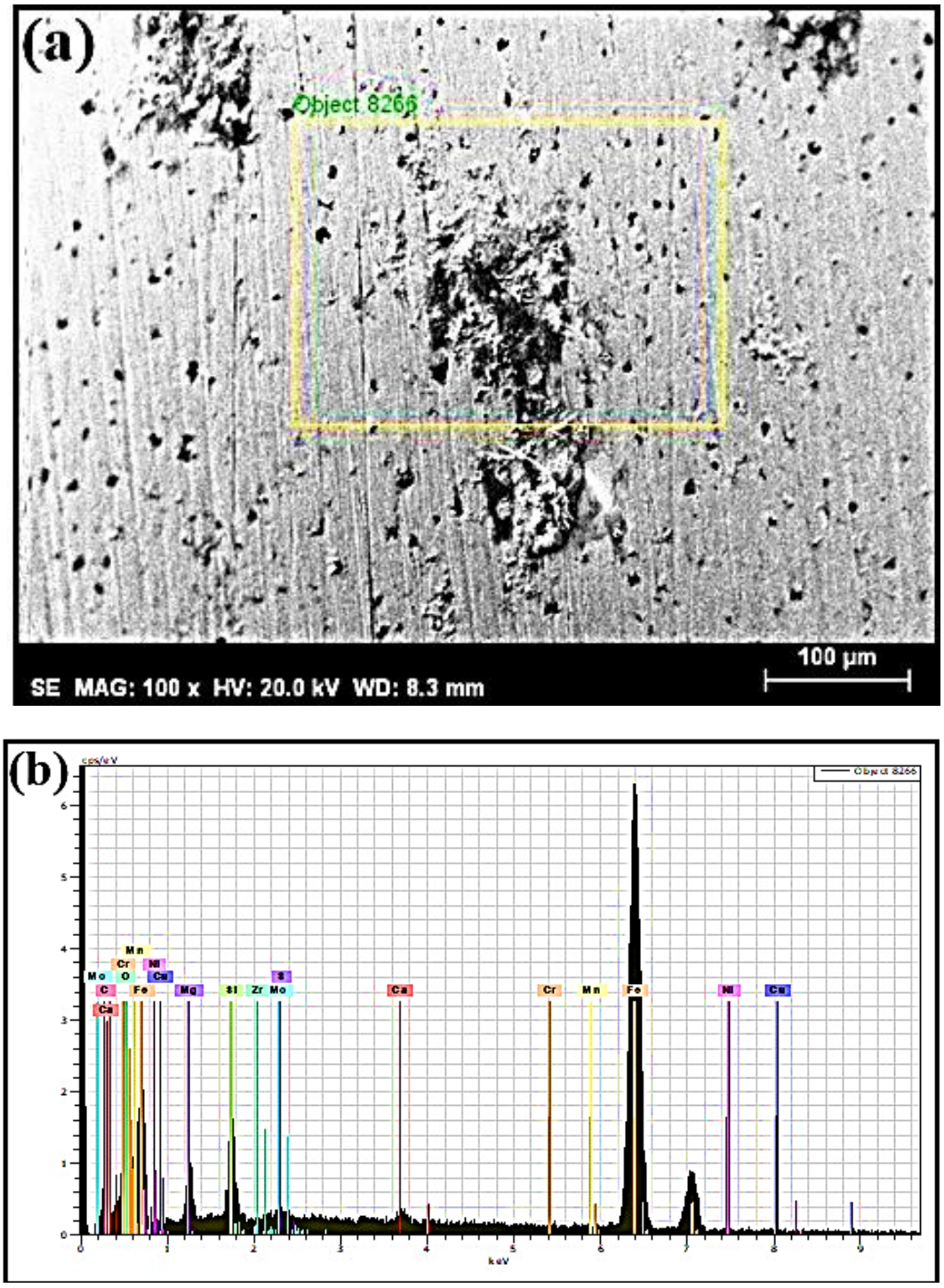

Fig. 7.19 (a) Micrograph and (b) Energy dispersive x-ray plot of representative wear surface of the disc

Table 7.13 Composition of material embedded on the wear surface of the disc

Embedded material on disc surface (% भार/wt.)											
Fe	O	Mg	Si	C	Cu	Mo	Ca	Ni	Mn	Cr	Zr
71.15	11.9	4.45	3.7	2.7	1.52	1.46	1.08	0.77	0.65	0.43	0.3

From Fig. 7.19(a), (b) and Table 7.13, it is observed that some of the wear debris is also found embedded over the disc's surface. Such embedded wear debris, having iron as a major contributor, is composed of the alloying elements of both disc surface and pin material.

CHAPTER 8

EXPERIMENTAL AND NUMERICAL INVESTIGATIONS OF A BRAKE DISC

8.1 Introduction

The behaviour of any newly developed material should be observed by tested in actual conditions after characterizing its various properties. For doing so, the actual components need to be developed and tested in real-world situations. In the present study, the aim is to develop the material for disc brake applications. Therefore, the brake disc is made from SiMoCr DCI and tested in actual braking situations against the brake pads used in the two-wheelers. For doing so a disc brake test rig is developed consisting of a power source, power transmission mechanism, brake shaft and the brake caliper installed on a robust frame. A brief description of the disc brake is as follows.

8.1.1 Disc brake

In a moving vehicle, the function of the braking system is to slow down the speed or take it to in rest position within the shortest span of distance at any time. Brakes are responsible for the still position of the vehicles on slopes against the gravity pull. The basic working of brakes implies the frictional resistance developed by the brake lining/pads which restrict the rotating motion of the wheel whenever brakes are applied. In simple words, the braking actions cause the conversion of, either kinetic energy/potential energy or both into frictional heat which may dissipate through the brake disc and brake lining/pads. Based on the operating mechanisms, there are many types of brakes used in vehicles like pneumatic brakes, magnetic brakes, mechanical brakes, etc.

On a steep slope, it is the effectiveness of the brakes which controls the vehicle's motion. In such situations, brakes continuously in action mode for longer durations making it essential to disperse the heat evolved during braking to the surroundings as speedily as possible. Generally, a vehicle is fitted with two types of brakes; the first one is the service brakes or foot-operated brakes and the second one is known as hand brakes or emergency brakes. The foot-operated brakes, under the action of applied force on the brake pedal, control the vehicle speed and stop it, whenever desired. The hand-operated brakes, with the application of force on the brake lever, are used to restrict the vehicle movement when parked or during emergency braking when service brakes fail. (Reif, 2014).

In the present era of modern transportation systems, braking systems have also developed a lot. Presently, disc brakes are mostly used in high-speed vehicles. Despite the benefits of self - energization and ease of parking brake integration, drum brakes suffered from numerous drawbacks like mainly the heat dissipation rate, and the fading of brake lining due to prolonged or repeated braking. Also, the presence of moisture in drum brakes turns the braking operation noisy with a reduced frictional coefficient between brake shoes and brake drum.

The components of the disc brake viz. brake disc, brake pads and brake caliper are briefly introduced in the following subsections:

8.1.1.1 Brake Disc

The brake disc, or the brake rotor, is attached to the hub of the wheel. The brake disc and the brake pads are the two main components that provide the requisite friction, thus producing the braking torque to control/stop the wheel movement. Studies showed brake discs must be strong enough to sustain the braking force and the heat produced due to the rubbing action of the brake pad over the brake disc surface. In addition to this local overheating of the brake disc may also damage the disc material structure. Generally, the

brake discs are made from cast iron, have good antifade properties and are relatively less costly among the available brake disc materials. Grey cast iron (GCI), Ductile cast iron (DCI), Martensitic stainless steel (MSS) and Aluminium metal matrix composite (ALMMC) are the commonly used disc brake materials. Different types of brake discs employed are namely solid disc, vented disc and drilled disc subject to the application. The selection of brake discs depends upon numerous factors; type of vehicle, environment, stable coefficient of friction, ability to withstand higher temperature, higher heat resistance, higher strength, durability, good thermal conductivity and heat transfer rate. In the present study, drilled disc used in two-wheelers as shown in Fig 8.1 is selected for studying its behaviour under the application of varying brake force.

Fig. 8.1 Two-wheeler brake disc assembly

8.1.1.2 Brake Pads

Brake pads play an important role in braking applications, when pressed against the brake disc, control/restrict the wheel rotation by converting the kinetic energy of the wheel into thermal energy. Brake pads are made from highly insulating material having low thermal conductivity so that it absorbs maximum heat generated during braking and allows only a part of heat conducted through it to the piston assembly preventing the vaporization of brake fluid. Friction material consists of abrasives (aluminium oxide, iron oxides, quartz, silica and zirconium silicate, etc), fillers, friction modifiers and binding materials as given in Table 7.1. The Friction material matrix bonded to a stamped steel backing plate alongwith wear indicator is a general representation of a brake pad. Fig. 8.1 shows the two brake pads positioned within the brake caliper in the front wheel of a two-wheeler, with their friction surfaces facing the brake disc. Fig. 8.2 shows the labelled brake pads.

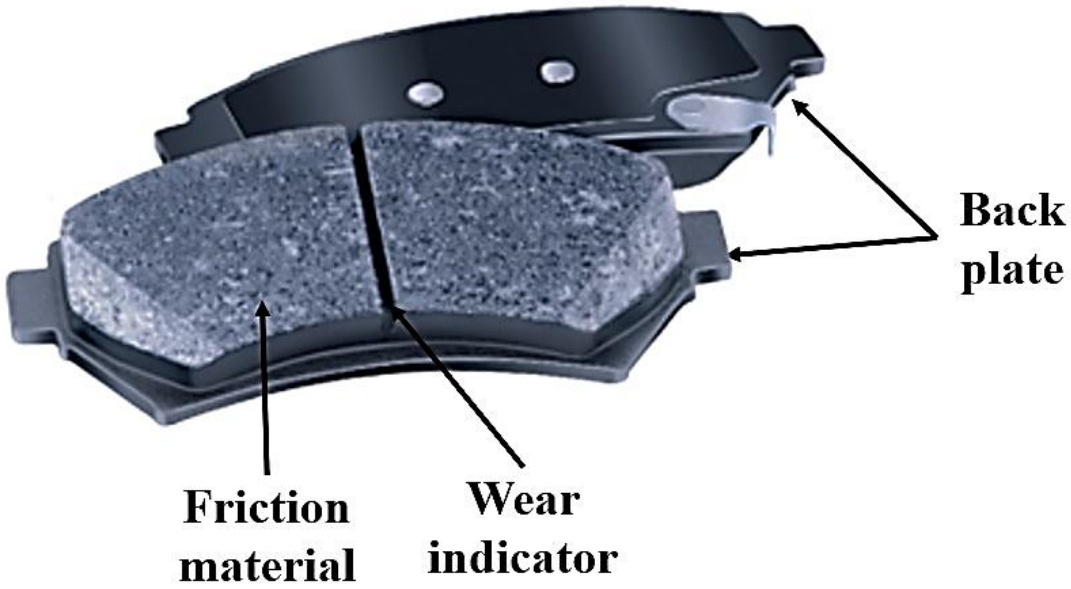

Fig. 8.2 Brake pad

When the brakes are applied, the hydraulic mechanism forces the brake fluid to press the brake pads against the rotating brake disc by clamping or squeezing the brake pads.

During rubbing of the brake pad against the brake disc under partial brake force or due to the effect of heat produced, few of the friction material is embedded over the brake disc surface. The heating of the brake pad by continuous rubbing over the brake disc surface loosens the friction material from the pad surface due to thermal softening and forms the friction film in the contact area and leaves stray marks of dull grey shades all over the disc surface in contact. (Xiao et al., 2016)

8.1.1.3 Brake Caliper

The brake caliper is the assembly of brake pads and pistons. Two types of calipers are generally used viz. fixed type calipers and floating type calipers. A caliper that does not move relative to the disc is termed as fixed-type calipers while the calipers which move with respect to the brake disc along a line parallel to the disc's axis of rotation are termed as floating-type calipers. A fixed type of caliper is less tolerant to disc imperfections, complex and more expensive than the floating type calipers. Floating-type calipers are also subjected to sticking failure which results in the rubbing of brake pads on the brake disc even when the brake force is removed. The brake caliper assembly houses the pistons, and these pistons apply the activation force to the brake pads. The brake caliper may accommodate one to six pistons, subject to the vehicle under consideration.

8.2 Experimental Setup

For studying the temperature and sliding wear behaviour of developed SiMoCr ductile cast iron, an experimental setup is to be assembled in the form of a test rig. The test rig consists of a power source, power shaft, power transmission drives, brake shaft, brake disc, caliper, brake lever, etc mounted on a metal frame. The brake disc is made from the Melt-3 as it has good wear properties in comparison to the other two developed melts. The brake disc is mounted on the driven shaft of the test rig and there is an arrangement

for fixing the brake caliper inline with the brake disc in such a way that the brake disc rotates freely within the brake pads. Both brake disc and brake pads are experiencing sliding friction on the application of brake force. The rubbing action of pads against the rotating disc will result in temperature rise as well as sliding wear or in simple words abrasive wear.

8.2.1 Power source

The selection of power source for conducting the brake disc experiments is based on the general calculation without going into the deep study of the two-wheeler brake force analysis based on static and dynamic load calculations. In the present study, for the selection of a power source the following assumptions are made:

Average weight of a two-wheeler including driver, M = 500 kgf (with a FOS of 2)

Average speed , v = 60km/hr (16.67m/s)

Time taken to stop, t_s = 4-5 sec

Therefore,

Energy dissipation involved in stoping

= Kinetic energy

$= \frac{1}{2} kMv^2 - 0$

Where,

k is the correction factor for rotating masses (Rudolf Limpert, 2011)

$= (\frac{1}{2} \times 1 \times (500) \times (16.67)^2) - 0$

= 69472 Joules

Brake power required in stoping the two wheeler in 4 seconds = 69472/4 = 17368 watt

This brake power is assumed equally distributed among the two wheels.

Then brake power required in stoping per wheel, q_0 = 17368/2 = 8684 watt

Brake torque required to apply brakes:

Angular velocity of 16 inch wheel

Distance covered by wheel in 1 revolution

$= \pi D = 1.43m$

RPM of wheel at 60Km/hr (1000m/minute), N $= \frac{1000}{1.43} = 699.3 \sim 700$ RPM

Angular velocity = $\frac{2\pi N}{60}$ = 73.16 rad/s

Torque = $\frac{\text{Brake power}}{\text{Angular velocity}}$ = 118.7 Nm

From the above calculations, it is clear that the requisite power source should have more than 120 Nm torque and 700 rpm which rotates the brake disc at the requisite speed, torque. For simplicity, an electric motor is a better option for this and preferably an induction motor for its advantages over the other which need not be explained here deliberately. The capacity of the induction motor is chosen based on the above calculations and this is fulfilled by the use of a 15 hp three-phase induction motor having 1440 rpm and 66 Nm torque. The use of a speed reduction mechanism having a speed reduction ratio of 2 will fulfill the rpm and torque requirements i.e. 720 rpm and 132 Nm torque.

8.2.2 Selection of drives for transmission and braking

For the transmission of power from the induction motor to the brake disc shaft, the chain and sprocket system is selected because it prevents any slip and additional losses in transmission when the rubbing action begins, unlike the belt pulley system. The size of the sprocket for the chain drive is selected in such a way that it reduces the rpm of the brake disc shaft to half that of the power shaft. It means the number of sprocket teeth on the driver shaft should be half of that on the driven shaft which will double the torque on the brake disc while reducing its rpm to 720. The ease and cost-effectiveness of

manufacturing sprockets allows for different ratios to be used by changing the sprockets thereby changing the rpm, torque and the rubbing force then can be modulated for different sets of readings on different brake discs. For the braking application, a hydraulic disc brake caliper set, used in motorcycles, is installed in position and the brake lever is fixed to a handheld shaft with a load adjuster for intermittent braking.

8.2.3 Brake disc

Brake discs are made from the as-cast brake disc of Melt-3. The various machining and surface finishing operations are shown in Fig. 8.3.

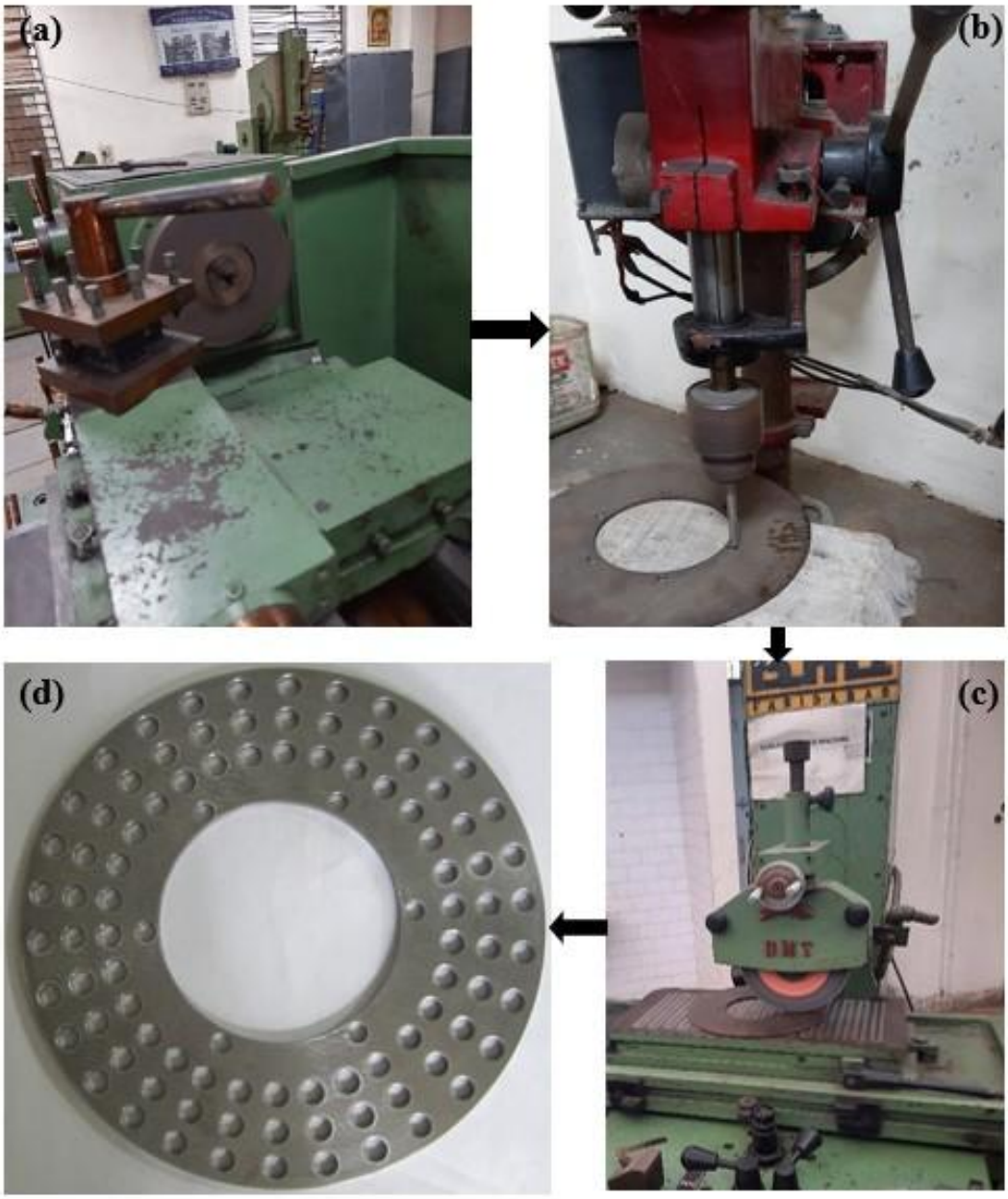

Fig. 8.3 Brake disc specimen preparation (a) machining, (b) Surface drilling, (c) Surface finishing, (d) prepared disc

The brake disc is made perforated by drilling 8mm holes throughout the surface for better dissipation of the heat produced during braking. The final size of disc prepared is:

Outer diameter of brake disc	= 240 mm
Inner diameter of brake disc	= 110 mm
Thickness of brake disc	= 4 mm
Size of drilled holes	= 8 mm

8.2.4 Frame

Frame, made from the mild steel hollow rectangular box section pipes, is the most robust part of the test rig, as it sustains both the weight of different parts mounted on it and vibrational forces produced in operations as well due to the induction motor and braking arrangement. The rubber pads are also placed below the frame for better dampening of vibrations during braking operation. The induction motor is directly mounted on the frame while the brake shaft is mounted in the c-section pillars. The brake caliper assembly set, used in motorcycles, is also mounted on a separate pillar in such a way that it allows free rotation of the brake disc. The brake lever is fixed to a hand-held shaft with a load adjuster as shown in Fig. 8.4.

8.2.5 Brake disc test

For conducting the experiment, the properly cleaned and weighed brake disc is installed on the brake disc shaft by adjusting the brake calipers in such a way that it will not affect the free rotation of the disc. A three-phase induction motor is fixed on the frame using vibration dampener pads between the motor and the frame. The chain drive mechanism is checked for free and stable rotation between the driver and driven shafts. The developed disc brake test rig setup is shown in Fig. 8.4. The temperature sensing gun and the tachometer are

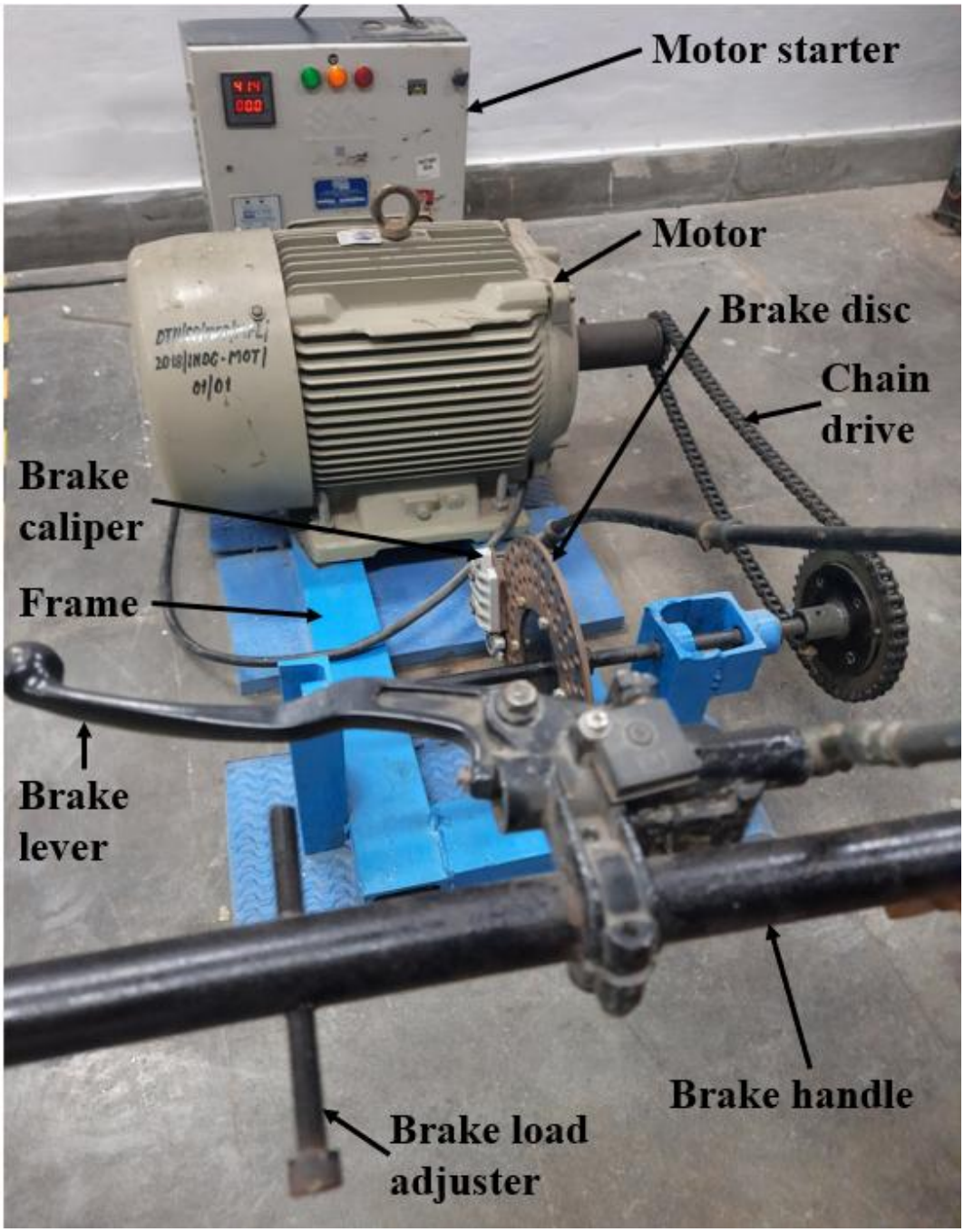

Fig. 8.4 Brake disc test rig setup

checked before the start of the test. The motor is started and the brake disc is allowed to rotate freely for a few minutes. Then the estimated brake force is applied to the brake lever by hanging the load in the load hanger and adjusting the load adjuster. The temperature and rpm of the brake disc shaft are continuously observed for 45 seconds with intermittent braking for 3 seconds and releasing the brake for a moment. After

completing the test the brake disc is removed from the brake shaft, weighed again and check for any brake pad/wear impressions over the surface.

The experiment is repeated for the estimated brake load till the brake load stops the rotation of the brake disc. The rise in disc temperature is noted for each experiment.

8.2.6 Temperature evolution in brake disc

Temperature evolution due to the rubbing of the brake pad against the brake disc is studied. Specific heat(C), thermal conductivity(k) and density(ρ) of the material play an important role in heat generation by rubbing of brake pad against the brake disc which results in temperature evolution in disc pad assembly. The evolution of temperature requires information about the transfer of heat generated during the rubbing action which includes the conductive, and convective heat transfer rate of the disc material. The convective heat transfer rate fluctuates with the variation in vehicle speed, brake component's design and position. Rudolf Limpert (2011) observed that any formula expressing the heat transfer coefficient yields only approximate results. The temperature evolved during intermittent braking is calculated using a simple analytical solution by considering the braking efforts, braking pauses remains unchanged and the brake disc-pad arrangement may be considered as a lumped system in which temperature evolution is uniform throughout and a function of time only. If the braking time is substantially less than the cooling time of the lumped system, then the cooling of the lumped system during braking may be neglected and temperature evolution $'\Delta T'$ will continuously increase and is calculated using Eq. 8.1 (Rudolf Limpert, 2011).

$$\Delta T = \frac{q_0 t_s}{\rho_R C_R V_R} \text{ K} \qquad \text{Eq. (8.1)}$$

where q_0 is the braking power absorbed by the brake disc, t_s is the braking time to stop, ρ_R is the brake disc density, C_R is the specific heat of the brake disc and V_R is the brake

disc volume. The evolution in temperature during intermittent braking is calculated using Eq. 8.2 for the lumped system (Rudolf Limpert, 2011).

$$[T(t) - T_{¥}]_a = \frac{\left[1-e^{\left((-n_a h_R A_R t_c)/(\rho_R C_R V_R)\right)}\right]\times[\Delta T]}{1-e^{\left((-h_R A_R t_c)/(\rho_R C_R V_R)\right)}} \quad ℃ \qquad \text{Eq. (8.2)}$$

where, h_R is the heat transfer coefficient, A_R is the brake disc surface area, t_c is the approximate cooling cycle time and n_a is the number of brake applications.

The heat transfer coefficient h_R is calculated using Eq. 8.3 based on the Reynolds number.

$$h_R = 0.04\left(\frac{k_a}{D_o}\right) R_e^{0.8} \qquad \text{Eq. (8.3)}$$

where,

K_a = thermal conductivity of air, = 0.026 W/m-K

D_o = outer diameter of the disc, = 0.24 m

R_e = Reynolds number $= \frac{\rho_a V D_o}{\mu_a}$ Eq. (8.4)

$= 2.71\times10^5$ which is more than 2.4×10^5 hence turbulent flow is considered

ρ_a - density of air = 1.2 kg/m^3

V - vehicle speed and

μ_a - kinematic viscosity of air= 1.77×10^{-5} Kg/m-s

8.2.7 Numerical simulation of brake disc

To carry out the simulations of the temperature evolution in brake disc by rubbing action of brake pad on application of brake force, a full-sized 3D deformable brake disc specimen alongwith brake pads, is modeled as per the dimensions of the actual specimen shown in Fig. 8.5. For reducing the simulation time, symmetric properties of the model are used and only the half of the thickness of the disc alongwith one brake pad is modeled

by considering the z-axis symmetry. The material properties obtained from the experiments and the literature are assigned to the brake disc specimen given in Table 8.1.

Table 8.1 Properties of brake disc and brake pad

Material	Young's modulus (E) GPa	Thermal conductivity (K) W/m-℃	Specific heat capacity (C) J/Kg-℃	Poisson's ratio (μ)	(ρ) kg/m^3	Coefficient of thermal expansion (α) 10^{-5}/℃
SiMoCr DCI*	160	33	506	0.26	7530	1.1
Brake pad	70	3	1300	0.24	2100	1.2

* www.ductile.org/ china-ductile-iron-castings.html

The material properties of the brake pad are also assigned as given in Table 8.1. The assembly of the brake disc and brake pad is done in the assembly module. The brake pad must be pressed against the rotating brake disc on the application of brake force and must retract to its original position after the removal of brake force. Such conditions are defined in the step module by assigning a total of 30 steps as dynamic temperature-displacement explicit steps. Even steps are of 3-second duration while the odd steps are of 0.5 seconds. Also, the history output and field output parameters are selected in the step module mainly for temperature and heat flux.

The surface-to-surface contact interaction properties with tangential, normal behaviour and heat generation properties are assigned to the brake disc and brake pad in the interaction module. The coupling constraint is assigned to the brake disc with its center so that angular velocity may be given to it as a boundary condition of the disc. The brake force is applied on the pad surface in the form of pressure in alternate steps in the load module. The brake force is applied on even steps and zero magnitude brake force is applied in odd steps. The amplitude of pressure is also defined for each step.

In the boundary condition module, the brake disc rotation is restricted only to the z-axis. The brake disc specimen is positioned in such a way that it freely rotates within the brake

pads. The displacement of the two brake pads is restricted only to move against the brake disc on the application of load on the pad surface by applying a boundary condition to restrict its x and y displacements during braking simulations. The symmetry of assembly along the z-axis is assigned. Angular velocity is assigned to the brake disc center. The initial room temperature is assigned to both the brake disc and brake pad in a predefined field module.

The boundaries of drilled holes are sensitive for simulation purposes. Therefore, local seeds are assigned to each drilled hole of the brake disc under the mesh module. Global seeds are assigned to the whole brake disc and brake pad. After applying mesh control and assigning element type, an 8-node C3D8T element, temperature-displacement coupled brick trilinear mesh is assigned to the assembly. Simulation is carried out and the temperature rise in brake disc assembly is observed for each brake force application. Mesh sensitivity analysis is done for different mesh sizes. Table 8.2 shows the details of the mesh assigned to the brake disc assembly for mesh sensitivity tests. The global mesh size ranges from 1 to 5 in the steps of 1. Global mesh size '1' results in time-consuming simulation while mesh size '5' is observed with lesser time but results are closer to the optimum mesh size of 3. The mesh sensitivity plot shown in Fig. 8.5 implies that there are no large variations observed in temperature values at different global mesh sizes.

Table 8.2 Mesh details of brake disc

Particulars	Global mesh size for linear hexagonal shaped C3D8T elements				
	1	2	3	4	5
No. of Elements	27668	10629	9285	8713	8322
No. of Nodes	43521	22560	19706	18486	17696

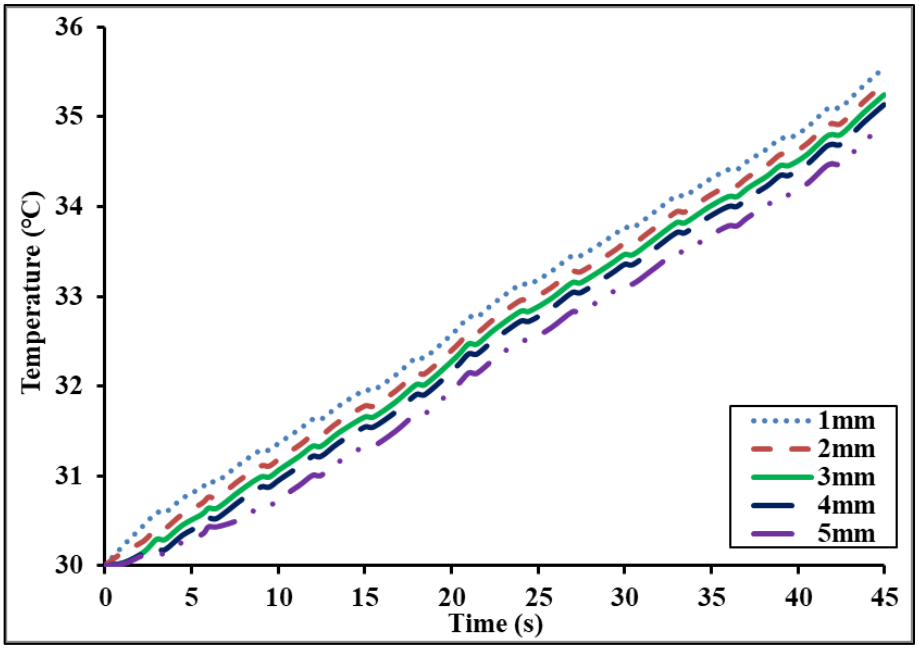

Fig. 8.5 Mesh sensitivity plot

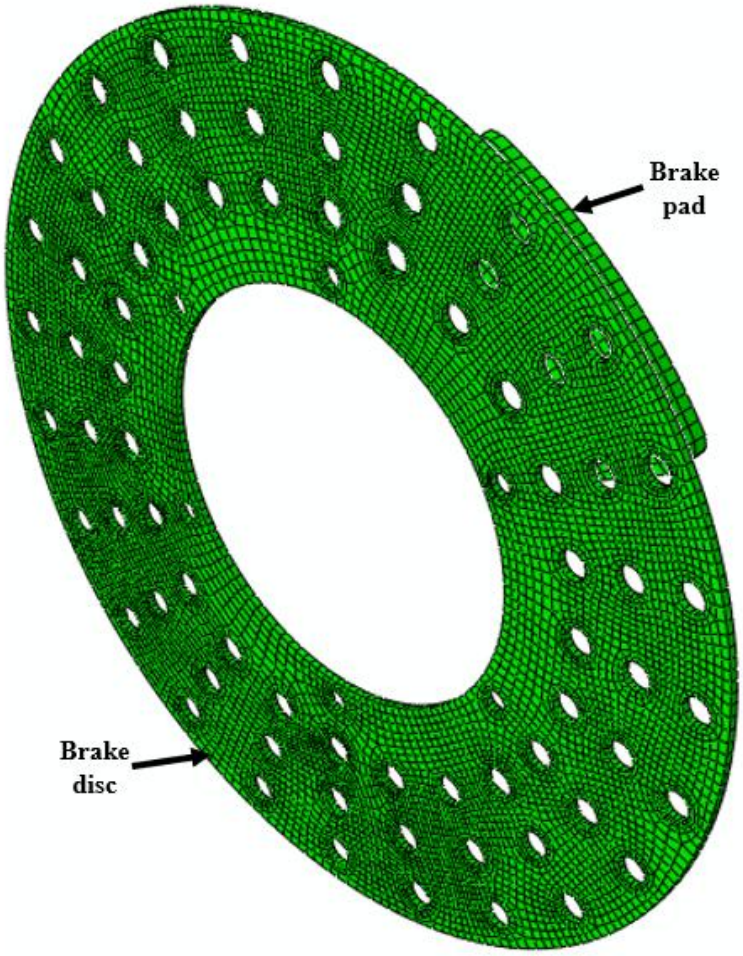

Fig. 8.6 A meshed model of brake disc in ABAQUS

8.3 Result and discussion

8.3.1 Wear in brake disc

The weight measurement of the brake disc before and after each test shows that no surface wear of the disc surface happened at all. This confirms the visual inspection of the disc surface that there are no traces of surface wear observed over the brake disc surface in contact with the brake pads. The reason for this may be either the short duration of the test or the wear loss is so small which may be neglected.

8.3.2 Temperature evolution in brake disc

Table 8.3 compiles the results obtained by both experimental and simulation. Whereas Fig. 8.7 shows only the experimental temperature increase at different applied forces. An overview of Table 8.3 and Fig. 8.7 shows that the temperature of the brake disc has increased at all applied brake forces. The temperature rise data obtained by the simulation is equivalent to the experimental data.

Table 8.3 Comparison of temperature evolved experimentally and by simulation

Time step	Temperature (°C)									
	Experimental					Simulation				
	10 N	20 N	30 N	40 N	50 N	10 N	20 N	30 N	40 N	50 N
3	30.1	30.6	33.1	36.7	43.2	30.3	31.1	33.4	36.5	48.2
6	30.2	31.3	35.3	44.1	57.6	30.6	31.9	36.7	44.2	61.4
9	30.4	32.1	38.9	51.4	72.7	30.9	32.9	41.1	52.8	74.7
12	30.6	32.8	41.9	59.6	84.6	31.3	33.8	45.5	62.3	90.8
15	30.9	33.9	45.6	67.2	99.8	31.6	34.7	48.8	70.2	105.1
18	31.2	34.8	48.8	74.1	113.3	32.1	35.4	51.6	78.9	117.2
21	31.5	35.7	52.1	84.4	124.8	32.4	36.3	56.1	87.1	130.4
24	31.9	36.6	55.8	92.6	139.1	32.8	37.1	60.2	95.2	144.6
27	32.2	37.2	59.5	100.2	156.9	33.2	37.8	63.3	103.2	155.7
30	32.6	37.8	62.9	109.7	168.8	33.4	38.6	66.8	110.6	168.1
33	32.9	38.3	66.6	116.4	177.8	33.8	39.2	69.8	118.7	180.2
36	33.2	38.7	69.7	123.3	185.5	34.1	39.7	73.5	126.1	190.4
39	33.4	39	71.6	127.5	192.3	34.4	40.5	76.3	134.3	202.7
42	33.5	39.2	72.8	130.3	196.1	34.8	41.1	78.8	142.6	212.8
45	33.6	39.4	73.6	132.4	198.7	35.2	41.8	81.8	146.9	221.7

It is seen that the rise in temperature evolution follows the applied brake force value. At lower brake force the temperature evolved, due to friction between the brake pad and disc, during braking is seen to be lower and rises upto 198.7°C at the higher brake force of 50N which equalizes the brake shaft torque and is sufficient to stop the brake disc rotation. The maximum temperature reaches approximately 190°C in an automotive disc brake with intermittent brake loads (Talati & Jalalifar, 2009).

The numerical analysis is done using Eq. 8.1 and 8.2. The rise in temperature in one brake

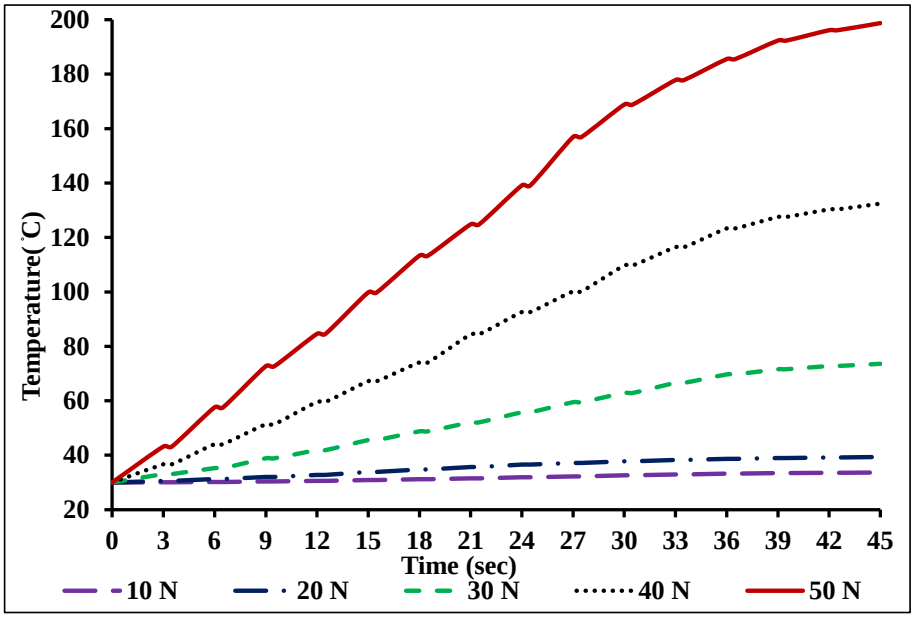

Fig. 8.7 Experimental result of brake disc test rig

stop is calculated as 71.94°C. And the total rise in temperature after intermittent braking of 15 times is 197.15°C and the brake disc temperature rises to 227.15°C (197.15 +30 (initial room temperature)).

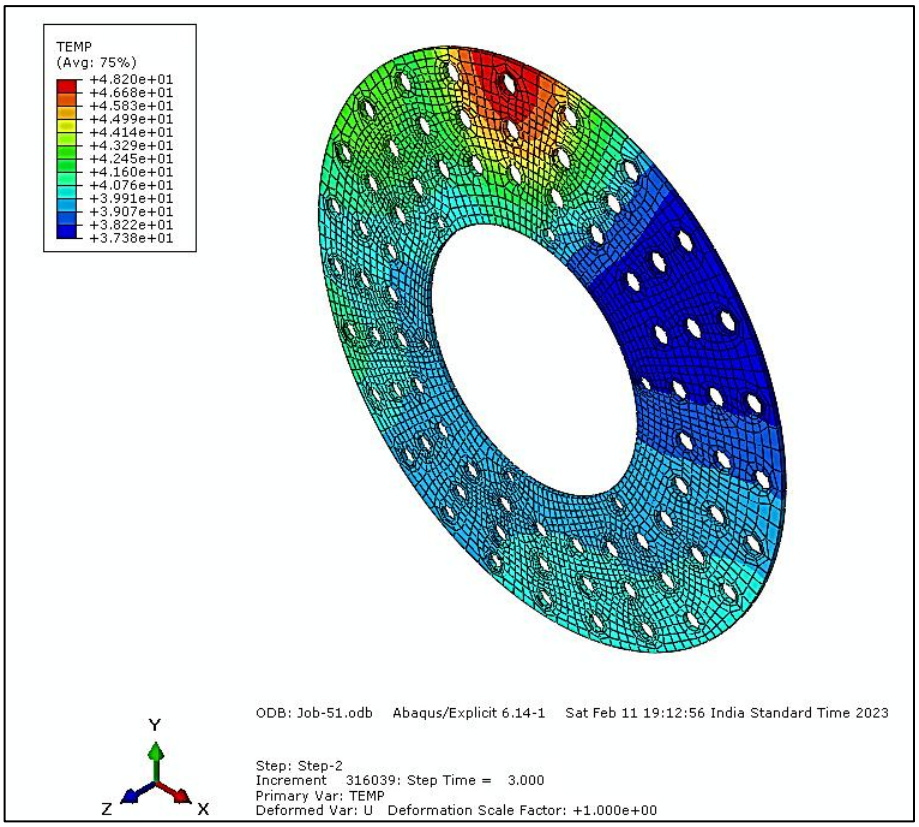

(i) After 3 seconds

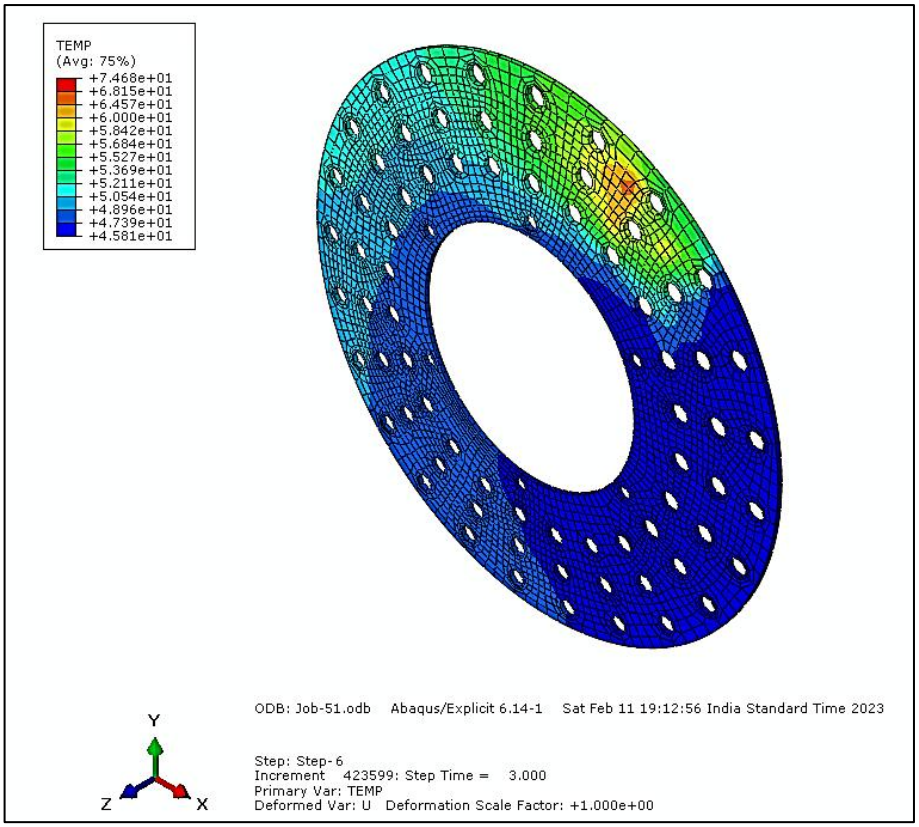

(ii) After 9 seconds

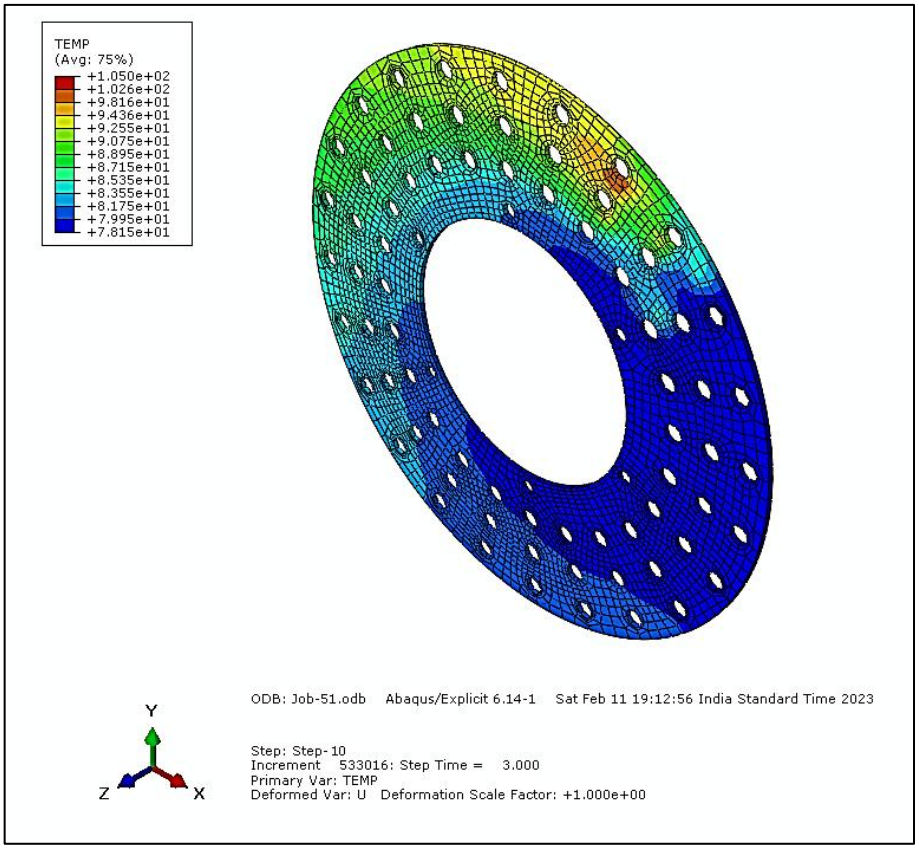

(iii) After 15 seconds

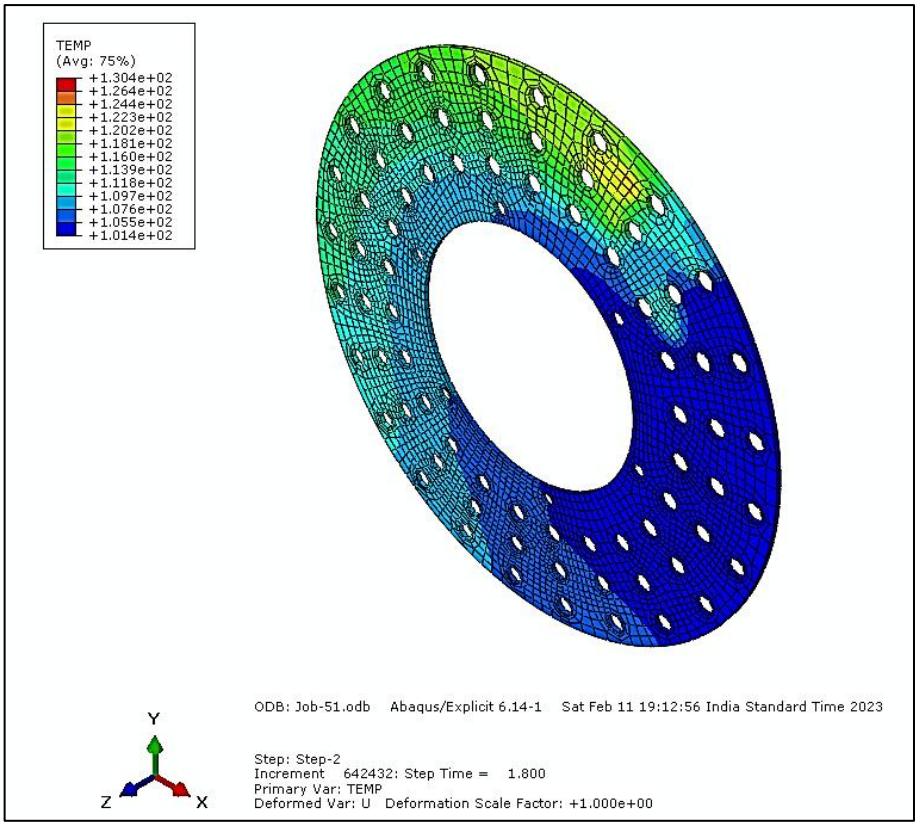

(iv) After 21 seconds

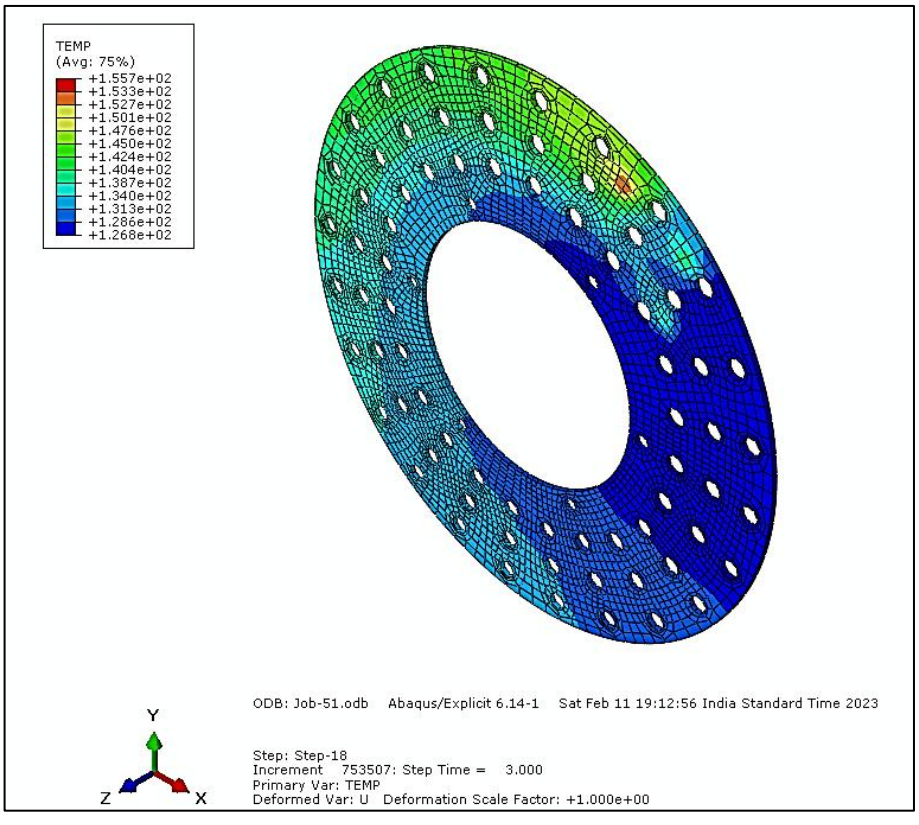

(v) After 27 seconds

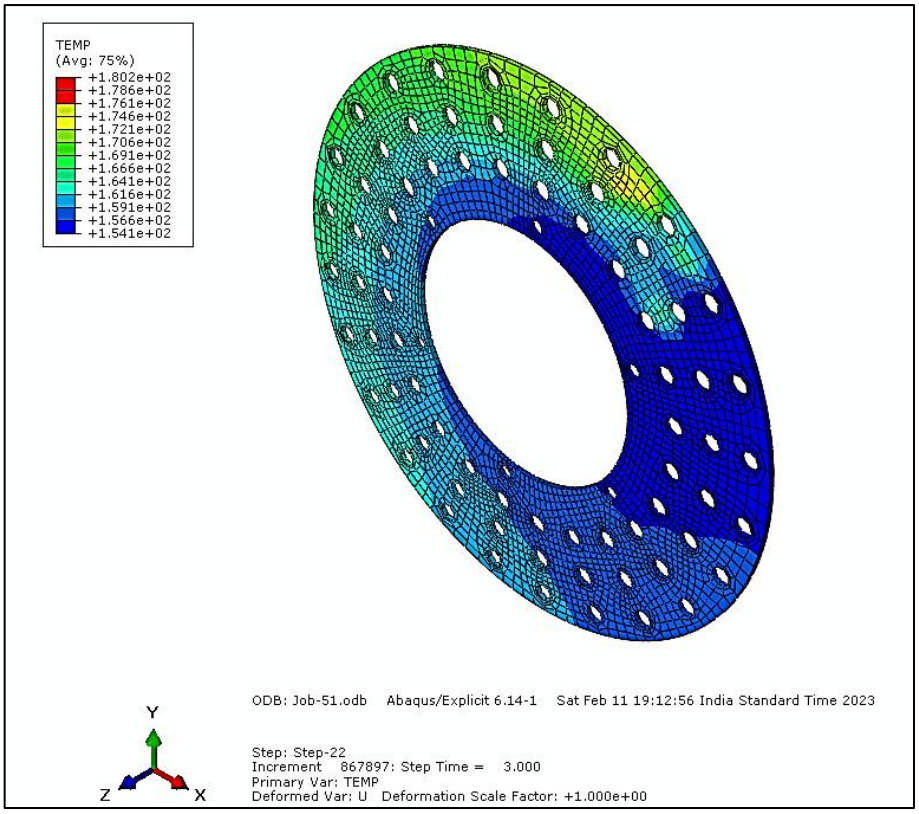

(vi) After 33 seconds

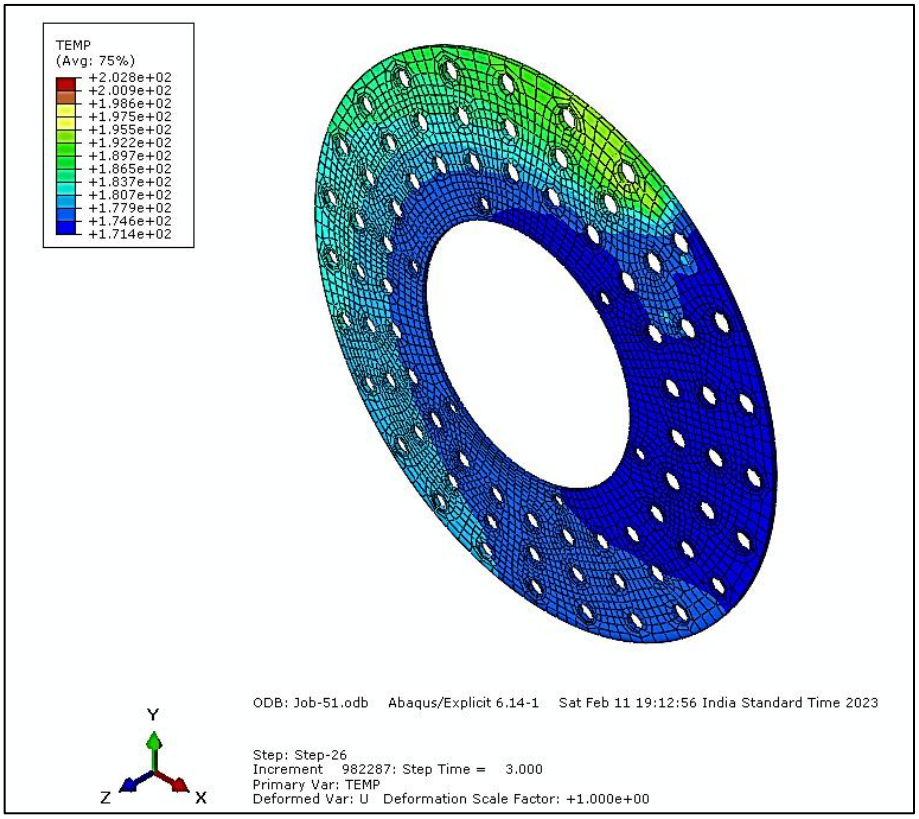

(vii) After 39 seconds

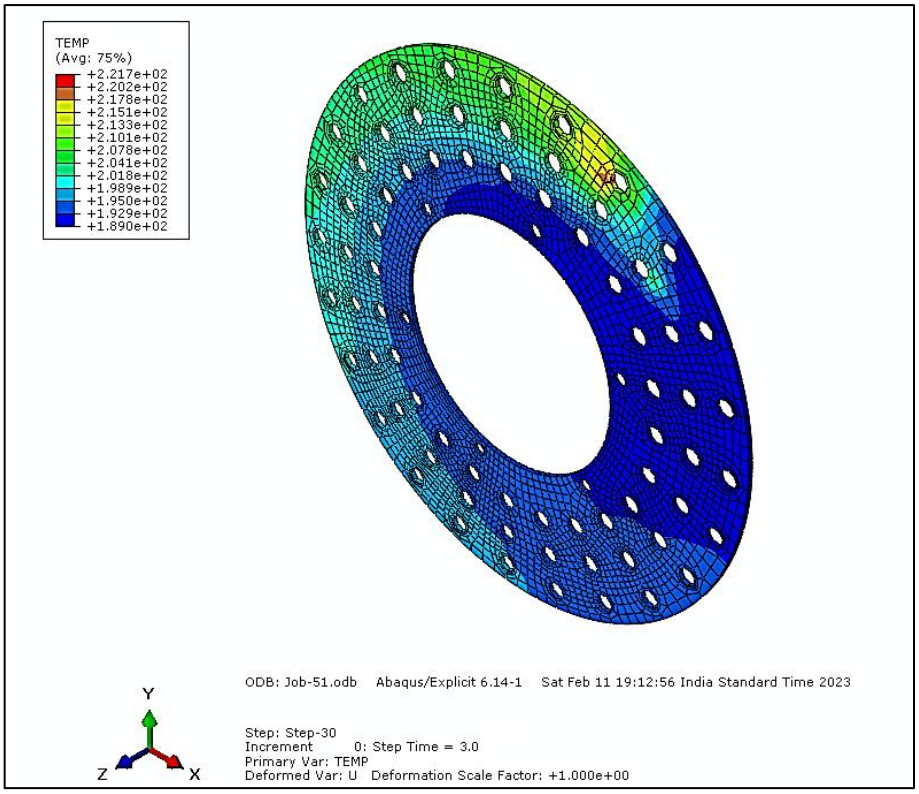

(viii) After 45 seconds

Fig. 8.8 Temperature effect observed at intermittent braking time span

Fig. 8.8 shows the behaviour of the brake disc during intermittent braking under the application of 50N brake force at the brake lever. The colour variation shows the temperature gradient throughout the brake disc surface. The maximum temperature is observed on the disc surface just passing the brake pad and the minimum temperature is observed on the disc surface as it just enters the brake pad squeezing area. The drilled holes play a crucial role in heat dissipation during disc rotation by providing more surface area and also allowing atmospheric air to pass through the drilled holes. The drilled holes also help in reducing the mass of the brake disc.

Fig. 8.9 shows the comparative rise in temperature at different applied brake force values during experiments and simulation.

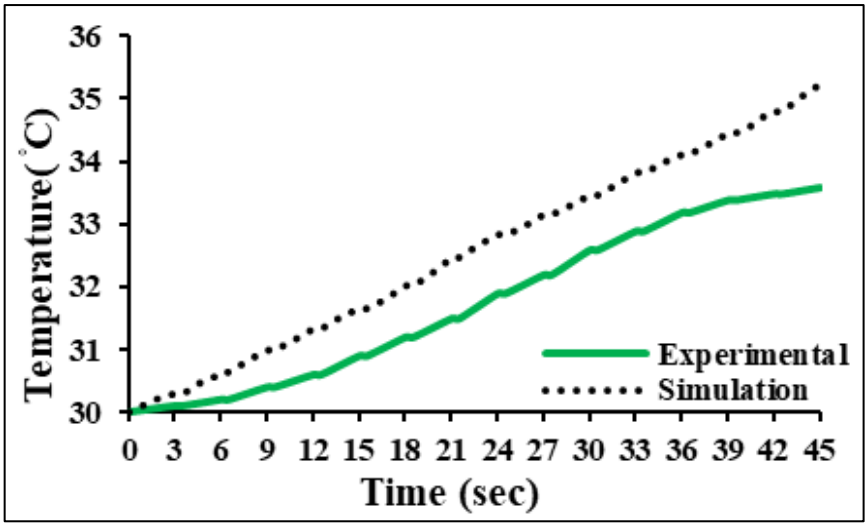
Temperature(°C)
36
35
34
33
32
31
30
0 3 6 9 12 15 18 21 24 27 30 33 36 39 42 45
Time (sec)
Experimental
Simulation

(i) 10 N

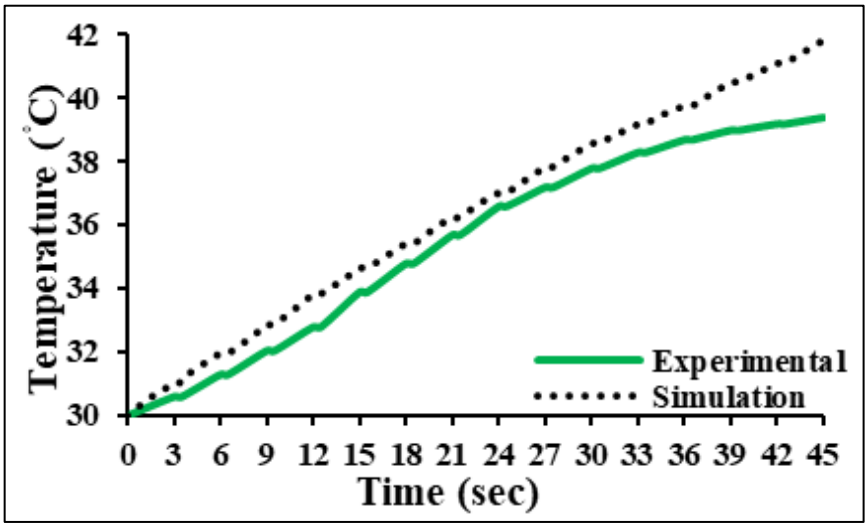
Temperature (°C)
42
40
38
36
34
32
30
0 3 6 9 12 15 18 21 24 27 30 33 36 39 42 45
Time (sec)
Experimental
Simulation

(ii) 20 N

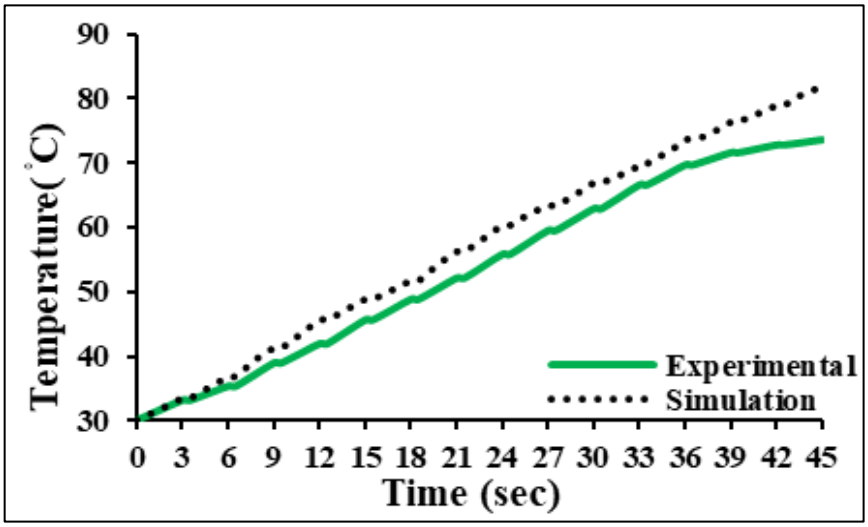
Temperature(°C)
90
80
70
60
50
40
30
0 3 6 9 12 15 18 21 24 27 30 33 36 39 42 45
Time (sec)
Experimental
Simulation

(iii) 30 N

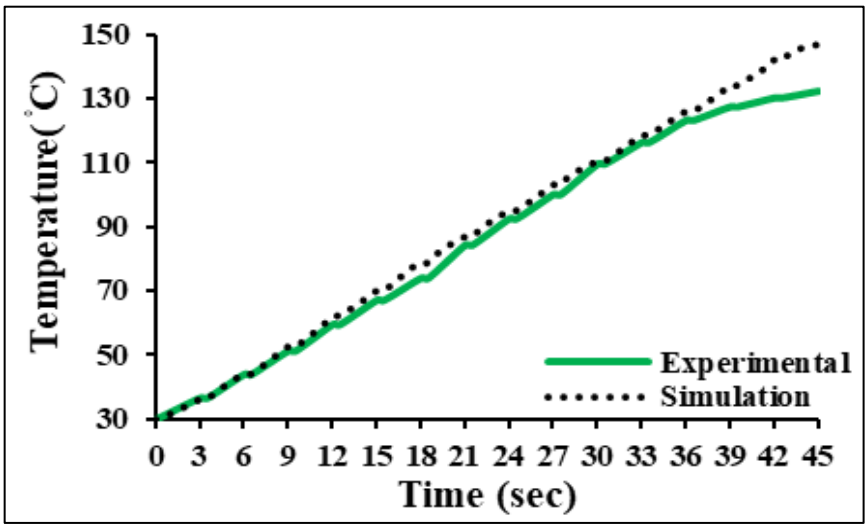

(iv) 40 N

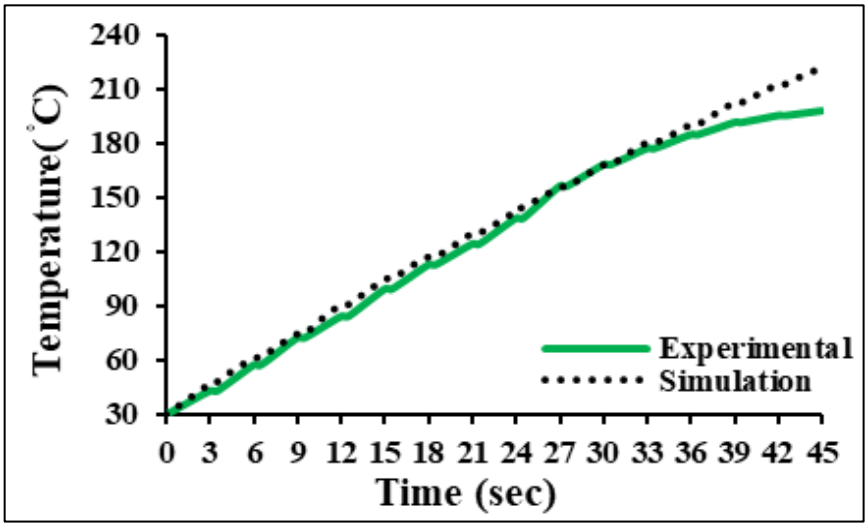

(v) 50 N

Fig. 8.9 Comparison of experimental and simulation result at different brake lever force

From Fig. 8.9. it is observed that the simulation curve rises similarly to the experimental curve under the application of all values of brake force till the midway and then rises above the experimental curve steeply which tries to become stagnant due to the more heat dissipation through radiative heat transfer in addition to conductive and convective heat transfer from the lumped assembly of brake disc due to the presence of silicon, molybdenum, chromium and copper in the ferritic-pearlitic matrix of the brake disc. The

presence of these alloyants in the disc material improves the thermal conductivity rate of the material. On observing Fig.8.9(i), a larger gap is observed between the experimental and simulation curve which reduces continuously on the application of higher application of brake lever force. Fig. 8.9(v) shows that both experimental and simulation curves closely followed each other for more than halfway through the total time. Fig. 8.8 and Fig. 8.9 show that the simulation results also agreed with the experimental results. The experimental value of temperature recorded at disc locking brake lever force of 50N is 198.7°C while the simulation results find the temperature value as 227.15°C and the mathematical calculations (Eq. 8.2) show the maximum temperature attained by the brake disc is 221.7°C.

The above study shows that the experimental results are in concordance with the simulation and mathematical calculations.

CHAPTER 9

CONCLUSIONS AND FUTURE SCOPE

9.1 SUMMARY

On observing the grades of the ductile cast iron given in Table 2.1, it is concluded that the tensile strength and percentage elongation are two properties on the basis of which different grades of DCI are designated. tensile strength of the grade increases on the cost of elongation or vice versa. There are numerous applications where both tensile strength and elongation are the prerequisite of the material to be chosen such as engine blocks, cylinder head, crankshaft, camshafts, brake discs, brake drums, suspension components, steering knuckles, exhaust manifold, nuclear cask etc. It is also observed from the available literature that the presently available ductile cast irons have shown good mechanical properties at room temperature and upto 500℃. Beyond this temperature the behaviour of ductile cast iron changes drastically. In actual working conditions, a lot of components are there which have undergone the high temperature working conditions. For efficient working, these components should possess both good strength and ductility at high temperatures too.

During its operational life, a component is subjected to wear due to the rubbing action of relative components and due to which the component may wear out or fail to perform the desired operation. It is desired that the material of components should possess good wear properties, strength and crack arresting properties for avoiding the failure due to fracture propagated from micro cracks on the surface or within the components.

Therefore, it is required to develop a material (SiMoCr ductile cast iron) which should retain its tensile strength, elongation, toughness and wear resistance properties even at

elevated temperature. The SiMoCr ductile cast iron developed and characterized in this research work shows good tensile strength, elongation, toughness alongwith good wear properties to meet the demand of the material having and retained such properties at elevated temperatures also.

9.2 CONCLUSIONS

In the present study, three different melts with the difference in alloying elements, Melt-1, Melt-2 and Melt-3, of SiMoCr ductile cast iron are prepared on charge calculation basis. Mechanical properties, tribological behaviour and microstructural features of the samples are studied. A brake disc of standard size is also prepared by casting and machining and tested in a real-world situation on a brake test-rig setup for the analysis of wear and temperature distribution during braking application. Based on the above experimental and numerical studies following conclusions are drawn:

1. The spherical nodule plays a significant role in arresting the crack and reorienting the crack path around the nodule as evidenced from the results of scanning electron microscopy. An increase in the nodule count decreases the nodule size which further results in higher tensile strength. Increasing the nodule count decreases the pearlite-ferrite ratio which results in a decrease in tensile strength but an increase in percentage elongation. The highest number of nodules are observed in the specimens of Melt-2 followed by Melt-1 which may be attributed to the respective carbon equivalent and negligible graphite floatation during solidification. The lowest nodule count in the specimens of Melt-3 may be attributed to the higher floatation during solidification when compared to Melt-1 and Melt-2.

2. The higher microshrinkage porosity in the microstructural samples of Melt-3 may be attributed to the formation of complex carbides due to the presence of Mo in conjunction with Cr. The alloying elements may increase the likelihood of micro-porosity in the castings.
3. The samples of Melt-2 show a higher tensile strength and elongation when compared with the properties obtained in Melt-1 and Melt-3. The highest values of the ultimate tensile strength (606MPa) and percentage elongation (13.98%) are observed in Melt-2.
4. The average hardness value of the specimens of Melt-3 is the highest followed by hardness values of specimens taken from Melt-2 and Melt-1, respectively. The average hardness value of the specimens of Melt-3 is the highest i.e., 298 ± 10.67 HV0.5 followed by hardness in samples of Melt-2 and Melt-1. This higher hardness may be attributed to an increased pearlitic region due to the presence of a higher amount of Si, Mo and Cr.
5. Johnson-Cook material model parameters are calculated using a well-established standard equation after performing the uniaxial tensile test at various strain rates (10^{-4} s^{-1}, 10^{-3} s^{-1}, 10^{-2} s^{-1} and 10^{-1} s^{-1}) and temperatures (room temperature, 423 K, 523 K and 623 K. It is observed that the material reveals a positive strain rate dependency. The tensile strength is directly dependent on the strain rate during testing which could be attributed to the lower time given to the specimens to undergo recovery during plastic deformation. It is also observed that ductility is inversely proportional to the rate of deformation. The reason for the lower ductility can be attributed to the sessile dislocations getting locked due to higher strain rates. The phenomenon of recovery gets sufficient time for the

glide of dislocations during deformation at higher temperatures and results in lower strength and ductility.

6. The average value of static fracture toughness obtained from the experiments for the specimen of Melt-2 is 54.49 MPa√m, followed by fracture toughness in the samples of Melt-1 and Melt-3. The higher value of static fracture toughness of Melt-2 may be attributed to the homogeneous distribution of the nodules in the matrix of ferrite and pearlite with lower microshrinkage porosity. According to the results obtained from FE simulations with a fatigue pre-crack using the experimental data, the simulated results for fracture toughness agree with the results obtained from the experiments.
7. The dry sliding wear behaviour is studied for Melt-3 being the hardest among the three melts. The sliding velocity significantly influences the specific wear rate, whereas the applied load is the key influencing parameter for a higher friction coefficient value. The temperature has been found as an optimum influencer on both sliding wear rate and coefficient of friction. Unambiguously, the minimum value of *'k'* and the higher value of *'μ'* are obtained at the lower level of the preselected wear parameters. From confirmation tests, it is found that the experimental results are in good agreement with the predicted results. The experimental values of *'k'* and *'μ'* at the rest of the preselected wear parameters are very close to the predicted data values using first-order regression analysis. Contour plots reveal that the minimum *'k'* value and maximum *'μ'* value may be obtained by selecting any combination of the wear parameters within the triangular region highlighted lighter in colour for *'k'* values and darker for the *'μ'* value of disc material. SEM and EdX analysis of

disc wear surfaces show that the more wear debris embedded in the disc surface is at higher levels of the wear parameters.

8. The behaviour of the brake disc against the brake pad was studied using a brake test rig setup and observed that negligible wear is captured during the trial runs at different brake forces. The experimental value of the increase in disk temperature at the locking brake load has been recorded as 198.7 °C, which agrees with the results obtained from numerical analysis and simulation.

9.3 SCOPE FOR FUTURE WORK

The growing trend of light weighting in the automotive industry is driving the demand for SiMoCr ductile cast iron, as it offers the strength of that of steel at a much lower weight. In addition, advancements in casting technology, such as computer-aided design and simulation, are leading to improved production efficiency and quality of SiMoCr ductile cast iron.

1. To study the microstructural features, tensile and hardness properties of samples of SiMoCr DCI at elevated temperatures will make it more suitable in high-temperature applications.
2. To study the tensile properties with higher strain rates at elevated temperatures will be used to estimate the Johnson-Cook damage material model parameters.
3. To study the fracture toughness properties of SiMoCr DCI specimens at higher temperatures.
4. To study the erosive behaviour of SiMoCr DCI samples to make the material suitable for the components used in fluid handling structures.
5. Cryogenic temperature applications look promising, particularly in the field of liquified natural gas (LNG) storage and transportation. LNG requires very low-

temperature storage, and the study of SiMoCr ductile cast iron properties, offers excellent resistance to brittle fracture and corrosion, at cryogenic temperature, which will make it a suitable material for LNG storage tanks and piping.

6. The elevated temperature applications look promising, particularly in the power generation industry, where SiMoCr ductile cast iron will be used in components such as steam turbine rotors and casings, etc.

In conclusion, the future of SiMoCr ductile cast iron is bright, and its use is likely to continue to grow in various industries as demand for high-strength and durable materials increases.

REFERENCES

1. Aal, A. A., Ibrahim, K. M., & Hamid, Z. A. (2006). Enhancement of wear resistance of ductile cast iron by Ni-SiC composite coating. *Wear*, *260*(9–10), 1070–1075. https://doi.org/10.1016/j.wear.2005.07.022
2. Abedi, H. R., Fareghi, A., Saghafian, H., & Kheirandish, S. H. (2010). Sliding wear behavior of a ferritic-pearlitic ductile cast iron with different nodule count. *Wear*, *268*(3–4), 622–628. https://doi.org/10.1016/j.wear.2009.10.010
3. Agnihotri, S. K. (2020). Evaluation of dynamic SIF during crack propagation in layered plates having property variation along the crack front. *Sadhana - Academy Proceedings in Engineering Sciences*, *45*(1), 1–10. https://doi.org/10.1007/s12046-020-01345-x
4. Agunsoye, J. O., Isaac, T. S., Awe, O. I., & Onwuegbuzie, A. T. (2013). Effect of Silicon Additions on the Wear Properties of Grey Cast Iron. *Journal of Minerals and Materials Characterization and Engineering*, *01*(02), 61–67. https://doi.org/10.4236/jmmce.2013.12012
5. Alhussein, A., Risbet, M., Bastien, A., Chobaut, J. P., Balloy, D., & Favergeon, J. (2014). Influence of silicon and addition elements on the mechanical behavior of ferritic ductile cast iron. *Materials Science and Engineering A*, *605*, 222–228. https://doi.org/10.1016/j.msea.2014.03.057
6. Aranzabal, J., Serramoglia, G., Goria, C. A., & Rousière, D. (2003). Development of a new mixed (ferritic-ausferritic) ductile iron for automotive suspension parts. *International Journal of Cast Metals Research*, *16*(1–3), 185–190. https://doi.org/10.1080/13640461.2003.11819580
7. Ast, J., Ghidelli, M., Durst, K., Göken, M., Sebastiani, M., & Korsunsky, A. M. (2019). A review of experimental approaches to fracture toughness evaluation at the micro-scale. *Materials and Design*, *173*, 107762. https://doi.org/10.1016/j.matdes.2019.107762
8. Banerjee, A., Dhar, S., Acharyya, S., Datta, D., & Nayak, N. (2015). Determination of Johnson cook material and failure model constants and numerical modelling of Charpy impact test of armour steel. *Materials Science and Engineering A*, *640*, 200–209. https://doi.org/10.1016/j.msea.2015.05.073

9. Basurto-Hurtado, J. A., Morales-Hernández, L. A., Osornio-Rios, R. A., & Dominguez-Gonzalez, A. (2016). An approach based on the exploratory data analysis to relate the wear behavior with the microstructure of ductile cast irons. *Advances in Materials Science and Engineering*, *2016*. https://doi.org/10.1155/2016/2605602
10. Bayrakceken, H., Ucun, I., & Tasgetiren, S. (2006). Fracture analysis of a camshaft made from nodular cast iron. *Engineering Failure Analysis*, *13*(8), 1240–1245. https://doi.org/10.1016/j.engfailanal.2005.11.001
11. Belhocine, A., Abu Bakar, A. R., & Bouchetara, M. (2016). Thermal and structural analysis of disc brake assembly during single stop braking event. *Australian Journal of Mechanical Engineering*, *14*(1), 26–38. https://doi.org/10.1080/14484846.2015.1093213
12. Benedetti, M., Fontanari, V., & Lusuardi, D. (2019). Effect of graphite morphology on the fatigue and fracture resistance of ferritic ductile cast iron. *Engineering Fracture Mechanics*, *206*(October), 427–441. https://doi.org/10.1016/j.engfracmech.2018.12.019
13. Berdin, C., Dong, M. J., & Prioul, C. (2001). Local approach of damage and fracture toughness for nodular cast iron. *Engineering Fracture Mechanics*, *68*(9), 1107–1117. https://doi.org/10.1016/S0013-7944(01)00010-8
14. Borsato, T., Berto, F., Ferro, P., & Carollo, C. (2016). Effect of in-mould inoculant composition on microstructure and fatigue behaviour of heavy section ductile iron castings. *Procedia Structural Integrity*, *2*, 3150–3157. https://doi.org/10.1016/j.prostr.2016.06.393
15. Borsato, T., Ferro, P., Berto, F., & Carollo, C. (2019). Effect of solidification time on microstructural, mechanical and fatigue properties of solution strengthened ferritic ductile iron. *Metals*, *9*(1). https://doi.org/10.3390/met9010024
16. Bougoffa, M. S. E., Bachir bey, M. N., Benouali, C., Sayah, T., Fellah, M., & Abdul Samad, M. (2021). Dry Sliding Friction and Wear Behavior of CuZn39Pb2 and AA7075 Under Industrial and Laboratory Conditions. *Journal of Bio- and Tribo-Corrosion*, *7*(2), 1–17. https://doi.org/10.1007/s40735-021-00475-x
17. Brauer, S. A., Whittington, W. R., Johnson, K. L., Li, B., Rhee, H., Allison, P. G., Crane, C. K., & Horstemeyer, M. F. (2017). Strain Rate and Stress-

State Dependence of Gray Cast Iron. *Journal of Engineering Materials and Technology, Transactions of the ASME*, *139*(2), 1–11. https://doi.org/10.1115/1.4035616

18. Cabanne Pierre-Marie. (2011). Fluctuations in Magnesium Treatment of Ductile Iron Some Reasons • Some Solutions. *S. G. Iron Conclave*, 33–36.
19. Callister Jr, W. D., & Rethwisch, D. G. (2020). Callister's Materials Science and Engineering. In *John Willey & Sons*. John Willey & Sons.
20. Čanžar, P., Tonković, Z., & Kodvanj, J. (2012). Microstructure influence on fatigue behaviour of nodular cast iron. *Materials Science and Engineering A*, *556*, 88–99. https://doi.org/10.1016/j.msea.2012.06.062
21. Cardoso, P. H. S., Israel, C. L., & Strohaecker, T. R. (2014). Abrasive wear in Austempered Ductile Irons: A comparison with white cast irons. *Wear*, *313*(1–2), 29–33. https://doi.org/10.1016/j.wear.2014.02.009
22. Çelik, M. B., Özdalyan, B., & Alkan, F. (2011). The use of pure methanol as fuel at high compression ratio in a single cylinder gasoline engine. *Fuel*, *90*(4), 1591–1598. https://doi.org/10.1016/j.fuel.2010.10.035
23. Chaengkham, P., & Srichandr, P. (2011). Continuously cast ductile iron: Processing, structures, and properties. *Journal of Materials Processing Technology*, *211*(8), 1372–1378. https://doi.org/10.1016/j.jmatprotec.2011.03.008
24. Collini, L., & Pirondi, A. (2019). Microstructure-based RVE modeling of the failure behavior and LCF resistance of ductile cast iron. *Procedia Structural Integrity*, *24*(2019), 324–336. https://doi.org/10.1016/j.prostr.2020.02.030
25. Davis, J. R., Associates, D., Henry, S. D., & Scott, W. W. (1996). *ASM Specialty Handbook- Cast Irons*.
26. Delprete, C., & Sesana, R. (2014). Experimental characterization of a Si – Mo – Cr ductile cast iron. *JOURNAL OF MATERIALS & DESIGN*, *57*, 528–537. https://doi.org/10.1016/j.matdes.2014.01.002
27. Dinda, S., & Kujawski, D. (2004). Correlation and prediction of fatigue crack growth for different R-ratios using Kmax and ΔK+ parameters. *Engineering Fracture Mechanics*, *71*(12), 1779–1790. https://doi.org/10.1016/j.engfracmech.2003.06.001
28. Ferrer, I., Sertucha, J., Sua, R., Asenjo, I., Larran, P., & Lacaze, J. (2008). Effect of mould inoculation on formation of chunky graphite in heavy section

spheroidal graphite cast iron parts. *International Journal of Cast Metal Research*, *20*(6), 319–325. https://doi.org/10.1179/136404608X286138

29. Ferro, P., Borsato, T., Berto, F., & Carollo, C. (2021). Fatigue strength assessment of heavy section ductile irons through the average strain density energy criterion. *Material Design and Processing Communications*, *3*(4), 1–7. https://doi.org/10.1002/mdp2.197
30. Ferro, P., Lazzarin, P., & Berto, F. (2012). Fatigue properties of ductile cast iron containing chunky graphite. *Materials Science and Engineering A*, *554*, 122–128. https://doi.org/10.1016/j.msea.2012.06.024
31. Fish, J., & Belytschko, T. (2007). *A first course in finite elements* (Vol. 1). John Wiley & Sons.
32. Gambirasio, L., & Rizzi, E. (2014). On the calibration strategies of the Johnson–Cook strength model: Discussion and applications to experimental data. *Materials Science and Engineering: A*, *610*, 370–413. https://doi.org/10.1016/j.msea.2014.05.006
33. Gambirasio, L., & Rizzi, E. (2016). An enhanced Johnson-Cook strength model for splitting strain rate and temperature effects on lower yield stress and plastic flow. *Computational Materials Science*, *113*, 231–265. https://doi.org/10.1016/j.commatsci.2015.11.034
34. Glavas, Z., Strkalj, A., & Stojakovic, A. (2016). THE PROPERTIES OF SILICON ALLOYED. *Metalurgija*, *55*(3), 293–296.
35. González-Martínez, R., de la Torre, U., Ebel, A., Lacaze, J., & Sertucha, J. (2018). Effects of high silicon contents on graphite morphology and room temperature mechanical properties of as-cast ferritic ductile cast irons. Part II – Mechanical properties. *Materials Science and Engineering A*, *712*(November 2017), 803–811. https://doi.org/10.1016/j.msea.2017.11.051
36. González-Martínez, R., de la Torre, U., Lacaze, J., & Sertucha, J. (2018). Effects of high silicon contents on graphite morphology and room temperature mechanical properties of as-cast ferritic ductile cast irons. Part I – Microstructure. *Materials Science and Engineering A*, *712*(October 2017), 794–802. https://doi.org/10.1016/j.msea.2017.11.050
37. Griffith, A. A. (1921). The phenomena of rupture and flow in solids. *Philosophical Transactions of the Royal Society of London. Series A*, *VI*(1), 9–14. https://doi.org/10.1098/rsta.1921.0006

38. Grzesik, W., Kiszka, P., Kowalczyk, D., Rech, J., & Claudin, C. (2012). Machining of nodular cast iron (PF-NCI) using CBN tools. *Procedia CIRP*, *1*(1), 483–487. https://doi.org/10.1016/j.procir.2012.04.086
39. Gupta, M. K., Sood, P. K., & Sharma, V. S. (2016). Machining Parameters Optimization of Titanium Alloy using Response Surface Methodology and Particle Swarm Optimization under Minimum-Quantity Lubrication Environment. *Materials and Manufacturing Processes*, *31*(13), 1671–1682. https://doi.org/10.1080/10426914.2015.1117632
40. He, J., Chen, F., Wang, B., & Zhu, L. B. (2018). A modified Johnson-Cook model for 10%Cr steel at elevated temperatures and a wide range of strain rates. *Materials Science and Engineering A*, *715*(November 2016), 1–9. https://doi.org/10.1016/j.msea.2017.10.037
41. Henrique, P., Cardoso, S., Biehl, L. V., Engenharia, E. De, Rua, F., Huch, A., Grande, R., Cep, B., & Israel, C. L. (2011). Evaluation of Abrasive Wear in Different Types of Cast. *Proceedings of COBEM 2011*.
42. Hervas, I., Thuault, A., & Hug, E. (2015). Damage Analysis of a Ferritic SiMo Ductile Cast Iron Submitted to Tension and Compression Loadings in Temperature. *Metals*, *5*, 2351–2369. https://doi.org/10.3390/met5042351
43. Hosdez, J., Limodin, N., Najjar, D., Witz, J. F., Charkaluk, E., Osmond, P., Forré, A., & Szmytka, F. (2020). Fatigue crack growth in compacted and spheroidal graphite cast irons. *International Journal of Fatigue*, *131*, 105319. https://doi.org/10.1016/j.ijfatigue.2019.105319
44. Iacoviello, F., di Cocco, V., & Bellini, C. (2019). Fatigue crack propagation and damaging micromechanisms in Ductile Cast Irons. *International Journal of Fatigue*, *124*(January), 48–54. https://doi.org/10.1016/j.ijfatigue.2019.02.030
45. Ibrahim, M. M., Nofal, A., & Mourad, M. M. (2016). Microstructure and Hot Oxidation Resistance of SiMo Ductile Cast Irons Containing Si-Mo-Al. *Metallurgical and Materials Transactions B*, 1–9. https://doi.org/10.1007/s11663-016-0871-y
46. Jhaveri, K., Lewis, G. M., Sullivan, J. L., & Keoleian, G. A. (2018). Life cycle assessment of thin-wall ductile cast iron for automotive lightweighting applications. *Sustainable Materials and Technologies*, *15*(January), 1–8. https://doi.org/10.1016/j.susmat.2018.01.002

47. Johnson, G. R., & Cook, W. H. (1983). A Computational Constitutive Model and Data for Metals Subjected to Large Strain, High Strain Rates and High Pressures. *The Seventh International Symposium on Ballistics*, 541–547.
48. Jozić, S., Bajić, D., & Celent, L. (2015). Application of compressed cold air cooling: Achieving multiple performance characteristics in end milling process. *Journal of Cleaner Production*, *100*, 325–332. https://doi.org/10.1016/j.jclepro.2015.03.095
49. Keough, J. R., & Hayrynen, K. L. (2000). Automotive applications of austempered ductile iron (ADI): A critical review. *SAE Technical Papers*, 344–354. https://doi.org/10.4271/2000-01-0764
50. Khan, W. N., & Chhibber, R. (2020). Effect of Intermetallic and Secondary Phases on Dry and Wet Sliding Wear Behavior of Super Duplex Stainless Steel. *Tribology Transactions*, *63*(3), 403–414. https://doi.org/10.1080/10402004.2019.1694731
51. Khare, S., Kumar, K., Choudhary, S., Singh, P. K., Verma, R. K., & Mahajan, P. (2021). Determination of Johnson–Cook Material Parameters for Armour Plate Using DIC and FEM. *Metals and Materials International*, *27*(12), 4984–4995. https://doi.org/10.1007/s12540-020-00895-3
52. Kujawski, D. (2001). A fatigue crack driving force parameter with load ratio effects. *International Journal of Fatigue*, *23*, S239–S246. https://doi.org/https://doi.org/10.1016/S0142-1123(01)00158-X
53. Kumar, P. (2009). *Elements of fracture mechanics*. Tata McGraw-Hill Education.
54. Lekakh, S. N., Buchely, M., O'Malley, R., Godlewski, L., & Li, M. (2021). Thermo-cycling fatigue of SiMo ductile iron using a modified thermo-mechanical test. *International Journal of Fatigue*, *148*(January), 106218. https://doi.org/10.1016/j.ijfatigue.2021.106218
55. Li, W., Yang, X., Wang, S., Xiao, J., & Hou, Q. (2020). Comprehensive analysis on the performance and material of automobile brake discs. *Metals*, *10*(3). https://doi.org/10.3390/met10030377
56. Lyu, Y. (2019). Abrasive Wear of Compacted Graphite Cast Iron with Added Tin. *Metallography, Microstructure, and Analysis*, *8*(1), 67–71. https://doi.org/10.1007/s13632-018-0504-8

57. Mamatha Gandhi, M., Bain, A., Prasanna, G. L., Vamshi, M., Saranya, J., Dhruthi, N., Sateesh, N., & Subbiah, R. (2021). Examination on dry sliding wear behavior of AISI 304 stainless steel treated with salt bath nitriding process. *Materials Today: Proceedings*, *44*, 1412–1417. https://doi.org/10.1016/j.matpr.2020.11.625
58. Mardaras, E., González-Martínez, R., Bayon, R., Nastac, L., & Méndez, S. (2020). Surface modification of ductile iron produced by an innovative in-situ casting technique. *International Journal of Cast Metals Research*, *33*(2–3), 103–111. https://doi.org/10.1080/13640461.2020.1766278
59. Matteis, P., Scavino, G., Castello, A., & Firrao, D. (2014). High Temperature Fatigue Properties of a Si-Mo Ductile Cast Iron. *Procedia Materials Science*, *3*, 2154–2159. https://doi.org/10.1016/j.mspro.2014.06.349
60. Montgomery, D. C. (2017). *Design and analysis of experiments*. John wiley & sons.
61. Murugesan, M., & Jung, D. (2019). Johnson Cook Material and Failure Model Parameters Estimation of AISI-1045 Medium Carbon Steel for Metal Forming Applications. *Materials*, *12*(4), 609. https://doi.org/10.3390/ma12040609
62. Nili Ahmadabadi, M., Zamani, C., Hoshmand, M. R., & Bahrevar, C. (2003). Effect of temperature on the hot formability of ductile iron in the semisolid state. *International Journal of Cast Metals Research*, *16*(1–3), 383–386. https://doi.org/10.1080/13640461.2003.11819613
63. Nilsson, K. F., & Vokál, V. (2009). Analysis of ductile cast iron tensile tests to relate ductility variation to casting defects and material microstructure. *Materials Science and Engineering A*, *502*(1–2), 54–63. https://doi.org/10.1016/j.msea.2008.09.082
64. Okunnu, R. (2015). *High Strength Solution-Strengthened Ferritic Ductile Cast Iron*. Aalto university.
65. Papis, K., Tunzini, S., Menk, W., Fischer, G., & Ag, A. (2014). Cast iron alloys for exhaust applications. *10th International Symposium on the Science and Processing of Cast Iron-SPCI10*, 1–8.
66. Pedersen, K. M., & Tiedje, N. S. (2008). Graphite nodule count and size distribution in thin- walled ductile cast iron. *Material Characterization*, *59*(8), 1111–1121.

67. Peng Chang, B., Md Akil, H., Bt Nasir, R., & Khan, A. (2015). Optimization on wear performance of UHMWPE composites using response surface methodology. *Tribology International*, *88*, 252–262. https://doi.org/10.1016/j.triboint.2015.03.028
68. Polajnar, M., Kalin, M., Thorbjornsson, I., Thorgrimsson, J. T., Valle, N., & Botor-Probierz, A. (2017). Friction and wear performance of functionally graded ductile iron for brake pads. *Wear*, *382–383*, 85–94. https://doi.org/10.1016/j.wear.2017.04.015
69. Prasad, B. K. (2006). Sliding wear response of a cast iron under varying test environments and traversal speed and pressure conditions. *Wear*, *260*(11–12), 1333–1341. https://doi.org/10.1016/j.wear.2005.09.017
70. Prasad, B. K. (2011). Sliding wear response of a grey cast iron: Effects of some experimental parameters. *Tribology International*, *44*(5), 660–667. https://doi.org/10.1016/j.triboint.2011.01.006
71. Pusch, G., Henkel, S., Biermann, H., H, P., Ludwig, A., & Trubitz, P. (2016). Recent Trends in Fracture and Damage Mechanics. In *Recent Trends in Fracture and Damage Mechanics*. https://doi.org/10.1007/978-3-319-21467-2
72. Ramya Sree, K., Reddy, G. K., Prasanna, G. L., Saranya, J., Anitha Lakshmi, A., Swetha, M., Vineeth Raj, T., & Subbiah, R. (2021). Dry sliding wear behavior of treated AISI 304 stainless steel by gas nitriding processes. *Materials Today: Proceedings*, *44*, 1406–1411. https://doi.org/10.1016/j.matpr.2020.11.624
73. Rebasa, N., Dommarco, R., & Sikora, J. (2002). Wear resistance of high nodule count ductile iron. *Wear*, *253*(7–8), 855–861. https://doi.org/10.1016/S0043-1648(02)00171-0
74. Reif, K. (2014). *Brakes, Brake Control and Driver Assistance Systems* (K. Reif, Ed.). Bosch Professional Automotive Information. https://doi.org/10.1007/978-3-658-03978-3
75. Rice, J. R. (1968). A path independent integral and the approximate analysis of strain concentration by notches and cracks. *Journal of Applied Mechanics, Transactions ASME*, *35*(2), 379–388. https://doi.org/https://doi.org/10.1115/1.3601206

76. Rodrigues, A. C. P., Yonamine, T., Sinatora, A., & Azevedo, C. R. F. (2016). Pin-on-disc tribotests with the addition of Cu particles as an interfacial media: Characterization of disc tribosurfaces using SEM-FIB techniques. *Tribology International*, *100*, 351–359. https://doi.org/10.1016/j.triboint.2016.03.034
77. Rudolf Limpert. (2011). *Brake Design and Safety* (Third edition). SAE International.
78. Sahin, Y., & Durak, O. (2007). Abrasive wear behaviour of austempered ductile iron. *Materials and Design*, *28*(6), 1844–1850. https://doi.org/10.1016/j.matdes.2006.04.015
79. Salehnejad, M. A., Mohammadi, A., Rezaei, M., & Ahangari, H. (2019). Cracking failure analysis of an engine exhaust manifold at high temperatures based on critical fracture toughness and FE simulation approach. *Engineering Fracture Mechanics*, *211*(August 2018), 125–136. https://doi.org/10.1016/j.engfracmech.2019.02.005
80. Salguero, J., Vazquez-Martinez, J. M., del Sol, I., & Batista, M. (2018). Application of Pin-On-Disc techniques for the study of tribological interferences in the dry machining of A92024-T3 (Al-Cu) alloys. *Materials*, *11*(7), 1–11. https://doi.org/10.3390/ma11071236
81. Satyendra. (2014, May 21). *Ductile Cast Iron*. IspatGuru. https://www.ispatguru.com/ductile-cast-iron/
82. Sertucha, J., Larranaga, P., Lacaze, J., & Insausti, M. (2010). Experimental investigation on the effect of copper upon eutectoid transformation of as-cast and austenitized spheroidal graphite cast iron. *International Journal of Metalcasting*, *4*(1), 51–58. https://doi.org/10.1007/BF03355486
83. Shafiee, A., Nili-Ahmadabadi, M., Ghasemi, H. M., & Hossein-Mirzaei, E. (2009). Wear behaviour of a Cr-Mo steel with different microstructures, in comparison with austempered ductile iron (ADI). *International Journal of Material Forming*, *2*(SUPPL. 1), 237–241. https://doi.org/10.1007/s12289-009-0636-0
84. Shirani, M., & Härkegård, G. (2011). Fatigue life distribution and size effect in ductile cast iron for wind turbine components. *Engineering Failure Analysis*, *18*(1), 12–24. https://doi.org/10.1016/j.engfailanal.2010.07.001

85. Shirani, M., Härkegard, G., & Morin, N. (2010). Fatigue life prediction of components made of spheroidal graphite cast iron. *Procedia Engineering*, *2*(1), 1125–1130. https://doi.org/10.1016/j.proeng.2010.03.121
86. Shrot, A., & Bäker, M. (2012). Determination of Johnson-Cook parameters from machining simulations. *Computational Materials Science*, *52*(1), 298–304. https://doi.org/10.1016/j.commatsci.2011.07.035
87. Singh Rooprai, R., Singh, T., Rana, M., & Kumar Sharma, V. (2022). Optimization of wear parameters for AISI 4140 using Taguchi grey relational analysis. *Materials Today: Proceedings*, *50*(3), 293–296. https://doi.org/10.1016/j.matpr.2021.06.336
88. Skaland, T. (2001). A New Approach to Ductile Iron Inoculation. *American Foundry Society*, 1–12.
89. Srinivasarao, P., Kumar Birru, A., & Scholar, R. (2017). Effect of Mechanical Properties with Addition of Molasses and FlyAsh in Green SandMoulding. In *Materials Today: Proceedings* (Vol. 4). www.sciencedirect.comwww.materialstoday.com/proceedings2214-7853
90. Stachowiak, G. W., & Batchelor, A. W. (2013). *E n g i n e e r i n g T r i b o l o g y*. Butterworth Heinemann.
91. Stawarz, M. (2017). SiMo Ductile Iron Crystallization Process. *Archives of Foundry Engineering*, *17*(1), 147–152. https://doi.org/10.1515/afe-2017-0027
92. Stefanescu, D. M. (2005). Solidification and modeling of cast iron - A short history of the defining moments. *Materials Science and Engineering A*, *413–414*(July), 322–333. https://doi.org/10.1016/j.msea.2005.08.180
93. Stefanescu, D. M. (2018). Thermodynamics Principles as Applied to Cast Iron. *Cast Iron Science and Technology*, *October*, 31–45. https://doi.org/10.31399/asm.hb.v01a.a0006295
94. Szmytka, F., Charkaluk, E., Constantinescu, A., & Osmond, P. (2020). Probabilistic Low Cycle Fatigue criterion for nodular cast-irons. *International Journal of Fatigue*, *139*(January), 105701. https://doi.org/10.1016/j.ijfatigue.2020.105701
95. Taguchi, G. (1987). *System of Experimental Design: Engineering Methods to Optimize Quality and Minimize Costs*. UNIPUB/Kraus International Publications, White Plains, NY, USA.

96. Talati, F., & Jalalifar, S. (2009). Analysis of heat conduction in a disk brake system. *Heat and Mass Transfer/Waerme- Und Stoffuebertragung*, *45*(8), 1047–1059. https://doi.org/10.1007/s00231-009-0476-y

97. Tokunaga, T., Kim, Y. J., & Era, H. (2019). Effect of Nickel Content on Microstructural Evolution in Austempered Solution-Strengthened Ferritic Ductile Cast Iron. *Journal of Materials Engineering and Performance*, *28*(7), 4034–4040. https://doi.org/10.1007/s11665-019-04184-y

98. Vaško, A. (2019). Structure and Fatigue Properties of SiMo and SiCu Types of Nodular Cast Iron. *Adria Symposium on Advances in Experimental Mechanics*, *36*, 67–68.

99. Vdovin, A., & Le Gigan, G. (2020). Aerodynamic and thermal modelling of disc brakes - Challenges and limitations. In *Energies* (Vol. 13, Issue 1). MDPI AG. https://doi.org/10.3390/en13010203

100. Viswanadham, P., & Singh, P. (1998). Failure Modes and Mechanisms in Electronic Packages. In *Failure Modes and Mechanisms in Electronic Packages* (1st ed.). Springer US. https://doi.org/10.1007/978-1-4615-6029-6

101. Weiß, P., Tekavčič, A., & Bührig-Polaczek, A. (2018). Mechanistic approach to new design concepts for high silicon ductile iron. *Materials Science and Engineering A*, *713*(August 2017), 67–74. https://doi.org/10.1016/j.msea.2017.12.012

102. Xiao, X., Yin, Y., Bao, J., Lu, L., & Feng, X. (2016). Review on the friction and wear of brake materials. *Advances in Mechanical Engineering*, *8*(5), 1–10. https://doi.org/10.1177/1687814016647300

103. Zeytin, H. K., Kubilay, C., Aydin, H., Ebrinc, A. A., & Aydemir, B. (2009). Effect of Microstructure on Exhaust Manifold Cracks Produced From SiMo Ductile Iron. *Journal of Iron and Steel Research International*, *16*(3), 32–36. https://doi.org/10.1016/S1006-706X(09)60040-6

104. Zou, J. peng, Shimizu, K., & Cai, Q. zhou. (2015). Effects of Cr Content and Annealing Temperature on Microstructure and Wear Characteristics of Cast Ausferrite Nodular Iron. *Journal of Iron and Steel Research International*, *22*(11), 1049–1054. https://doi.org/10.1016/S1006-706X(15)30111-4

PUBLICATIONS BASED ON THE PRESENT WORK

The followings are the publications in journals and conferences based on the present work.

International Journals: -

1. Ram Nanak, Gautam Vijay (2022). Characterization of Fracture Toughness of As-Cast Si-Mo-Cr Ductile Cast Iron. Journal of Polymer & Composites, Volume 10, Special Issue 1, 2022. doi (Journal): 10.37591/JoPC.
2. Ram Nanak, Gautam Vijay (2023). Characterization of dry sliding behaviour of a Si-Mo-Cr ductile cast iron, FME Transactions, Volume 51, 2023, Pages 48-58. doi: 10.5937/fme2301048R.

International Conferences: -

1. Ram Nanak, Gautam Vijay (2022). Evaluation of Johnson-Cook material model parameters for Si-Mo-Cr ductile cast iron, International Conference on Thermo-Fluid and System Design **(ICTFSD-2022)** held at BITS Mesra, Ranchi Jharkhand, India during March 22-23, 2022. Materials Today: Proceedings, Volume 61, Part 1, 2022, Pages 16-20. https://doi.org/10.1016/j.matpr.2022.03.298.
2. Ram Nanak, Gautam Vijay (2022). Prediction of effect of alloying elements on properties of ferritic grade Si-Mo ductile cast iron using regression analysis, 13th International conference on Material Processing Characterization **(ICMPC-2022)** held at GRIET Hyderabad, Telangana, India on April 22-24, 2022. Materials Today: Proceedings, Volume 62, part 6, Pages 3855–3859. https://doi.org/10.1016/j.matpr.2022.04.524.
3. Ram Nanak, Gautam Vijay (2022). Prediction of effect of alloying elements on properties of ferritic grade Si-Mo. 7th International Conference on Advanced

Production and Industrial Engineering **(ICAPIE) – 2022** held jointly at Delhi Technological University, Delhi and National Institute of Technology Delhi, India during **June 11-12th, 2022.** Advances in Transdisciplinary Engineering. doi*:10.3233/ATDE220809.*

BIO DATA

Mr. Nanak Ram was born in Sonipat, Haryana on 20th June 1980. He did his diploma in Mechanical Engineering from Govt Polytechnic Sirsa Haryana. He graduated from JIET Jind, Kurukshetra University Haryana in 2003 and did his post-graduation in Manufacturing Engineering from the National Institute of Technical Teachers Training and Research (NITTTR), Chandigarh in 2014. Currently, he is pursuing Ph.D. as a part-time scholar under the guidance of Prof. Vijay Gautam, in the Department of Mechanical Engineering, DTU Delhi.

He has twenty years of teaching experience in the field of Manufacturing Processes, Applied Mechanics, Machine Drawing-I & II, Engineering Drawing, Engineering Materials and Metal Forming. He has been teaching these subjects at both Diploma and Undergraduate levels. He worked as officiating Principal/ Principal in different polytechnics in Haryana. His research area is focused on the field of materials Characterization. He has guided many diploma and undergraduate students on various projects. He has published his work in international journals and conferences. He is a member of IEI (Institutions of Engineers India).